

See discussions, stats, and author profiles for this publication at: <https://www.researchgate.net/publication/283348025>

# GVIP–Volume10–Issue4–P1151544413

Data · November 2015

DOI: 10.13140/RG.2.1.4196.0403

---

CITATIONS  
0

READS  
374

---

23 authors, including:



Ashraf Aboshosha

ICGST LLC

213 PUBLICATIONS 178 CITATIONS

[SEE PROFILE](#)



Imed Riadh Farah

Université de la Manouba

209 PUBLICATIONS 798 CITATIONS

[SEE PROFILE](#)



Nagachetan Bangalore Manjunathamurthy

Visio Ingenii Limited

26 PUBLICATIONS 68 CITATIONS

[SEE PROFILE](#)



Rupert C D Young

University of Sussex

297 PUBLICATIONS 2,630 CITATIONS

[SEE PROFILE](#)

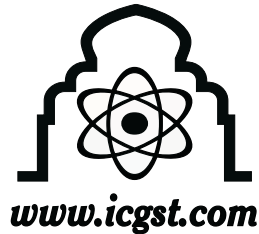
Some of the authors of this publication are also working on these related projects:



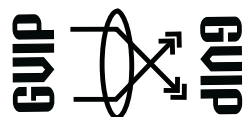
PhD at Sussex University [View project](#)



Sentiment analysis [View project](#)



## **The International Congress for global Science and Technology**



**ICGST International Journal on Graphics, Vision  
and Image Processing  
(GVIP)**

**Volume (10), Issue (IV)  
October, 2010**

[www.icgst.com](http://www.icgst.com)  
[www.icgst-amc.com](http://www.icgst-amc.com)  
[www.icgst-ees.com](http://www.icgst-ees.com)

**© ICGST LLC, Delaware, USA, 2010**

GVIP Journal  
ISSN Print 1687-398X  
ISSN Online 1687-3998  
ISSN CD-ROM 1687-4005  
© ICGST LLC, Delaware, USA, 2010

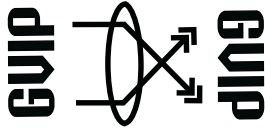
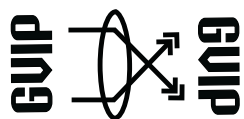


## Table of Contents

Papers	Pages
P1151031180, Nagachetan Bangalore and Rupert Young and Philip Birch and Chris Chatwin, "Tracking Moving Objects Using Bandpass Filter Enhanced Localisation and Automated Initialisation of Active Contour Snakes"	1--8
P1151011027, Aba M. Patil and Satish R. Kolhe and Pradeep M. Patil and Milind E Rane, "Modified Fisher Face Approach for Robust Biometric Recognition System"	9--15
P1151032181, M. Usman Akram and Aasia Khanum and Khalid Iqbal, "An automated System for Liver CT Enhancement and Segmentation"	17-22
P1151035261, K.P. Ajitha Gladis and K. Ramar and Jestin Rajamony, "Content-Based Image Retrieval Using Templates of Medical Images"	23--34
P1151026162, L. H. You and B. P. Tang and X. Y. You and J. J. Zhang, "Creating and Manipulating Surfaces through Physics-based Curve Deformations"	35--46
P1151024133, R.K.Kulkarni and S.Meher and J.M.Nair, "An Adaptive Switching Filter for Removing Impulse Noise from Highly corrupted Images"	47--53
P1151025147, Z. B. Rabah and I. R. Farah and B. Solaiman and H. B. Ghzala, "Reducing Change of Illumination Effect for Hyperspectral Image Unmixing"	55--64



**ICGST International Journal on Graphics, Vision and Image Processing  
(GVIP)**

**A publication of the International Congress for global Science and Technology -  
(ICGST)**

**ICGST Editor in Chief: Ashraf Aboshosha**

**[www.icgst.com](http://www.icgst.com), [www.icgst-amc.com](http://www.icgst-amc.com), [www.icgst-ees.com](http://www.icgst-ees.com)**

**[editor@icgst.com](mailto:editor@icgst.com)**



# Tracking Moving Objects Using Bandpass Filter Enhanced Localisation and Automated Initialisation of Active Contour Snakes

Nagachetan Bangalore, Rupert Young, Philip Birch, Chris Chatwin

*Industrial Informatics Research group,*

*Department of Engineering and Design, University Of Sussex, Brighton, BN1 9QT, UK*

E-mail: nb56@sussex.ac.uk, R.C.D.Young@sussex.ac.uk

## Abstract

This paper describes a robust and accurate method of Active Contours, also known as Snakes. Active Contours (AC) are a completely different approach to feature extraction. The feature being extracted is the contour of an object in an image or a video frame. Active Contours can also be used to allow tracking of any object in a video sequence using the knowledge of the contour of the object being tracked. In this paper a new method of minimization of boundary co-ordinates of the object is used for the Snake initialization. The boundary co-ordinates of the object under study are extracted using threshold, filtering and morphological operations. A fine tuned Difference of Gaussian (DoG) filter is used to extract the edge image of the object in a scene. The DoG filtered image is also used to add a new energy functional term in the AC Snake energy equation. A new method of adding and removing snake points based on the distance between the points is introduced. Thus, in this paper, a modified energy functional for energy minimization and a new method of AC Snake initialization is proposed. The new snake model designed is dynamic and can be applied both on static and dynamic video frames. In order to show the performance of the proposed snake model several experimental results are presented for frame data from video sequences.

**Keywords:** Active contours, Snake initialization, Snake algorithms, tracking, image segmentation, Edge based active contours

## 1. Introduction

Contour extraction is one of the basic tasks in image and video processing. Object tracking is an important task in any computer vision system. A Snake can be explained as an energy minimization curve that represents several salient features of shape of the object being considered. It is associated with an energy functional which is designed in a manner that achieves a minimum value near the object boundaries, hence reducing the problem of locating an object boundary. Various parameters of the object namely: area; height; centroid; shape; motion and orientation, can be deduced using the contour feature of the Active contour technique. The Active contour Snakes are elastic curves defined within an image to move under the influence of the internal forces extracted from the curve itself and the external forces computed from the image data [1-4].

Snakes are a more general technique of matching a deformable model to an image by means of energy minimization. The basic snake model is a controlled continuity curve under the association of image forces, external constraint forces and internal forces. The external image forces propel the snake towards the salient image features. The internal snake force serves to improve the smoothness constraint of the contour and the external constraint forces drive the snake to near the desired local minimum points, in this case exterior edges [1-3, 5] .

The position of the snake can be parametrically represented by:

$$v(s) = [x(s), y(s)], s \in [0,1] \quad (1)$$



The energy functional can be expressed in the continuous domain as:

$$E_{\text{snake}}^* = \int_0^1 [\alpha \cdot E_{\text{int}}(v(s)) + \beta \cdot E_{\text{ext}}(v(s))] ds \quad (2)$$

where  $E_{\text{int}}$  and  $E_{\text{ext}}$  are the internal and external energies. The internal energy signifies the energy due to bending and the external energy signifies the image energy and the constraint energies to contour the required point on an object. The parameters  $\alpha$  and  $\beta$  are the constants controlling the influence of different energies giving importance to the data to be contoured [5].

Unlike most other techniques for finding salient contours, the model is active and fast. The following sections discuss a new technique of incorporating a term derived from a thresholded difference of Gaussian filtered image in the equation to allow quick and accurate contouring of the edges of the object being tracked. A technique for initializing snake points at the first iteration using the thresholded difference of Gaussian filtered images to improve accuracy is introduced. Methods to decrease the number of snake points in the contour is discussed to improve the robustness in real-time tracking of an object in a sequence. The paper is divided into five major sections detailing the difference of Gaussian filter term, snake initialisation, snake deformation and progression. The final section is preceded by the conclusion, presenting the result, analysis and verification of the algorithm developed.

## 2. Design of Difference of Gaussian (DoG) Filter

A Difference of Gaussian filter is implemented in the spatial frequency domain of the image as a band-pass filter. It is calculated as a convenient good approximation to a scale normalized Laplacian of Gaussian (LoG) filter as it is accurately and readily implementable in the spatial frequency domain as a band-pass filter. In addition to this, the spatial domain numerical approximation of a Laplacian of a Gaussian filter has a high tendency to have a ringing effect. The ringing effect results in the appearance of spurious or ring like edges near the sharp transition at the edges of an object. Thus the frequency domain implementation of the DoG filtering operation is preferred in the current application.

The DoG band-pass thus filters an image to perform an edge enhancement operation on the objects present in the image [10].

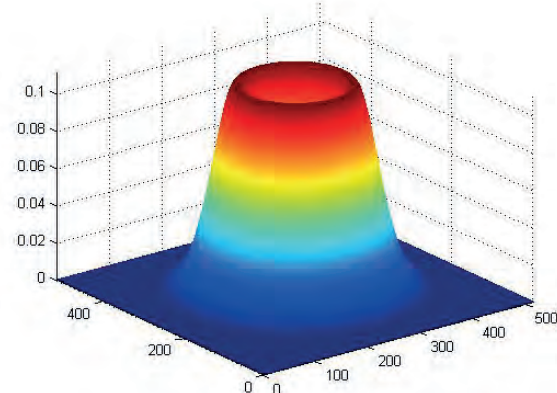


Figure 1 DoG filter shown as band-pass filter in the spatial frequency domain

Writing the Gaussian distribution in standard form,

$$D(x, y) = \frac{1}{2\pi\sigma^2} \cdot \exp\left(-\frac{x^2 + y^2}{2\pi\sigma^2}\right) \quad (3)$$

the DoG filter function can be described as the difference of two differently scaled Gaussians functions;

$$D(x, y) = \frac{1}{2\pi\sigma_2^2} \cdot e^{-\left[\frac{x^2+y^2}{2\pi\sigma_2^2}\right]} - \frac{1}{2\pi\sigma_1^2} \cdot e^{-\left[\frac{x^2+y^2}{2\pi\sigma_1^2}\right]} \quad (4)$$

Where, the  $\sigma_1$  and  $\sigma_2$  represent the different standard deviations of the Gaussian function. The ratio between the two sigma values is maintained at 1.6 for the DoG filter to have an optimum performance as a band-pass filter to allow accurate zero-crossing detection at the edge locations in images [6, 11, 17].

## 3. DoG filtered image term in the Snake expression

An example test frame is shown in figure (2) with a DoG filtered output of the frame shown in figure (3) (with an appropriate bias added so the bi-polar filtered image can be displayed as an intensity image).

From figure (3), it can be seen that the location of the edges of the object under consideration are detected using the filtering process. Due to the second differential operation performed by the DoG filter, the pixel values at the image edges have zero-crossings between positive and negative values. The negative pixel values at the location of the edges can be utilized for the addition of a new parameter in the Snake equation.





Figure 2 Test frame



Figure 3 DoG band-pass filtered image

Considering Equation (2), this can be expressed at any point  $v_i$  as:

$$E_{\text{snake}}^* = \alpha \cdot E_{\text{int}}(v_i) + \beta \cdot E_{\text{ext}}(v_i) \quad (5)$$

where,  $i = 1$  to  $n$ ,  $n$  being the number of points in the AC Snake.

The internal energy function is intended to enforce a shape on the deformable contour and to maintain a constant distance between the points in the contour. It consists of continuity energy ( $E_{\text{cont}}$ ) and curvature energy ( $E_{\text{curv}}$ ).

An average distance between contour points is computed and denoted as  $\text{avgd}$  [1,2]. The variable  $\alpha$  is initialized and the continuity term is calculated, being denoted as  $E_{\text{cont}}$ . This can be computed according to:

$$E_{\text{cont}}(i) = \text{abs}(\text{avgd} - \text{norm}(\text{curp} - \text{pix}(:, :))) \quad (6)$$

where,  $\text{curp}$  denotes the current contour position and  $\text{pix}(:, :)$  represents the initial contour point vector. The  $\text{abs}$  and  $\text{norm}$  terms, signify the absolute and norm functions, respectively.

The constraint energy can be of many kinds and here we consider the curvature energy. The

curvature energy is computed using the initial Contour point vector [5, 6, 8, 9]. The curvature energy, denoted as  $E_{\text{curv}}$ , controls the curve or bending of the contour and can be computed according to:

$$E_{\text{curv}}(i) = \text{norm}(\text{pix}(i-1) - 2 \cdot \text{curp} + \text{pix}(i+1))^2 \quad (7)$$

The external energy functional attracts the deformable contour to interesting features, such as object boundaries, in the image. The image energy is computed for each neighbourhood pixel. The image energy will be the sum of intensity energy and the gradient energy. The magnitude of the intensity of a corresponding image point in the neighbourhood gives the image intensity energy,  $E_{\text{in}}$ , and the gradient magnitude of the same point gives the image gradient energy,  $E_{\text{grad}}$  [1,2,5]. This can be expressed as follows:

$$E_{\text{image}} = \beta \cdot (E_{\text{in}} + E_{\text{grad}}) \quad (8)$$

The DoG filtered image pixel values can be added to the equation for each pixel external energy computation. If the value of each DoG filtered output pixel is considered as the energy of the DoG at that pixel then the energy term can be denoted by  $E_{\text{DoG}}$  and inserted into the overall expression as below:

$$E_{\text{ext}} = E_{\text{image}} + c \cdot E_{\text{DoG}} \quad (9)$$

The constant  $c$  gives a measure of the influence of the DoG filtered image energy at the pixels being considered. Thus, by adhering to the energy minimization rule of the Snake algorithm, an improved selection of the correct edge pixel for the contouring process is achieved leading to a greater accuracy in the choice to contour edges of the object.

#### 4. Automatic initial Contour extraction

In classical methods, an initial contour point is selected by the user, near to the contour of the target object. Various methods use circular or rectangular initial contour points around the object of interest. The minimum energy functional, its coordinates and the weighting parameters are then initialized. The energy functional is calculated, as explained in the previous section, by considering several feature parameters to calculate the energy.

The new method, designed to initialize the contour on the given object, is based on locating a moving object in the scene and employing the DoG filter image boundary extraction technique. For any given



frame (frame 1) DoG filtering is performed, followed by threshold and morphological operations. The morphological operation used is binary erosion and is employed in order to remove unconnected noisy edges. A subsequent frame (frame 2) is also processed in a similar manner to obtain two different edge images. This step is illustrated (after adding a bias to allow display of the images) in figures (4) to (7) below.



Figure 4: Frame 1



Figure 5: Frame 2



Figure 6: DoG filtered frame 1



Figure 7: DoG filtered frame 2

An absolute subtraction of the DoG filtered output of frames 1 and 2, shown in figures (6) and (7), is performed after a threshold operation. This gives only the moving object edges, comprising both edges in the position of the object in frame 1 and frame 2. Binary erosion is performed on the resultant image to get rid of the residual noisy edges resulting from the subtraction. The resultant image is as shown in figure (8). The resultant image is now further processed, the coordinates of the first non-zero pixel chain in the image being located by scanning the entire image (starting from the top left as the origin). From the first non-zero pixel of the pixel chain a boundary tracing operation is initiated to obtain a boundary traced image, as shown in figure (9).



Figure 8: DoG subtracted resultant image



Figure 9: Boundary traced image



The boundary thus extracted is placed in a coordinate vector array containing the coordinates of all pixels in the boundary. The number of boundary pixels is too large for fast and efficient calculation of the Snake contours. The coordinate vector is reduced so as to achieve a fixed pixel spacing between each element. For instance, in this case it is done by selecting every 5<sup>th</sup> coordinate point in the array to produce a reduced resolution contour vector with fixed pixel spacing of five pixels thus reducing the number of snake points, n, in the contour. This forms the initial contour vector of the snake and is shown below in figure (10).



Figure 10: Initial contour

## 5. Snake Deformation

The energy functional and the initial contour are computed as explained in the previous sections considering several feature parameters to calculate the energy (see equations 5, 8 and 9). Eight point neighbourhood pixels are traversed and the energy functional of each of these points is computed. The total energy of each point calculated is compared with the minimum energy and the new points are appended in the contour point vector, based on the minimum energy criterion. Thus, by iterating for all contour points in the initial contour, the AC fits around the moving object under consideration [15-18].

The active contour of the next frame is based on the active contour vector of the current frame. Thus the current frame contour vector becomes the initial contour vector of the next frame. After setting the initial contour, the snake deformation takes place in an iterative manner, as explained earlier, in order to fit on to the object being contoured. Contouring the same object under motion in subsequent frames, result in the snake acting as a dynamic, deforming contour. This then allows tracking of the moving object. In the frames in which the object becomes static, the Snake remains on the final boundary

locations of the object thus locking onto the object[16].

## 6. Snake Progression

Due to the dynamic change in shape of the object tracked, there can be an addition or removal of extra snake points into the contour vector. When the length of any segment between two coordinate points in the active contour array goes higher than the average distance  $avgd$  an addition of a coordinate point takes place to compensate for the changes in the object. Similarly, when the length of any segment between two coordinate points in the array goes lower than the average distance  $avgd$  a coordinate point is removed from the contour array to compensate for the shrinkage in size of the object being traced. This allows the snake to efficiently define the object shape even if there is a change in the scale or rotation of the object during a tracked sequence in the scene [5]. Figures 11 and 12 illustrate the snake deformation and progression in an example sequence.

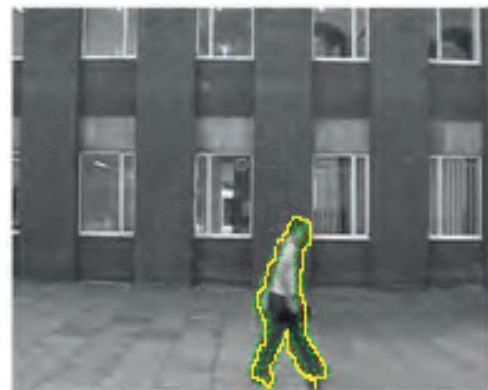


Figure 11: Frame 3

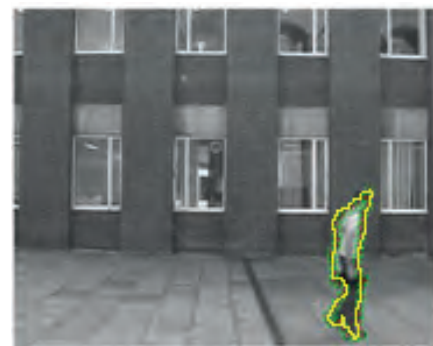


Figure 12: Frame 30

Thus, the modified Snake progresses to follow the object deformation and motion. It then stops and appends onto the same points when the object ceases to move. A few more examples are shown below in Figures 13 to 16 to show the Snake contouring operation [14].





Figure 13: Frame 1 (before deformation)[14]

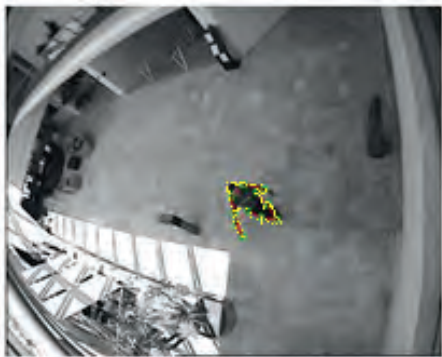


Figure 14: frame 3 (after deformation)



Figure 15: Frame 60 (after deformation)



Figure 16: frame 103 (continuously tracked)

In a further example, frames from an infrared traffic video are shown in Figures 17 and 18, illustrating the tracking of a motor vehicle.



Figure 17: Snake on IR video frame 10



Figure 18: Continuously tracked car frame 22

This algorithm can either be used in an image or on frame data in a continuous video. The algorithm is applied after converting the RGB images to gray-scale colour space. It can also be applied on infrared images converted to gray-scale colour space. The active contours are set as soon as the object in a video is in motion and the contour follows the object by deforming onto the object in each frame, thus providing robust tracking of the acquired object in the video. The introduction of the new energy functional term derived from the DoG filtered image reduces the snake energy to give emphasis to the object edges, thus making the snake deformation faster and more robust.

## 7. CONCLUSION

This paper introduces a modified model for active contours which is fast, robust and accurate as compared to other available methods for Active Contours or Snake models[2-5, 15-18]. The described method is based on DoG filtered images thus giving more emphasis to the edges of the object under study.



The method of automatic contour initialization makes it possible for the algorithm to work on video sequences without user interaction, unlike previously presented methods [1-9, 13]. The initial contour set, based on moving objects and the boundary data of the object, makes the snake fitting and deformation quicker than the other methods previously reported in the literature. Due to the initialization on the edges of the object, the snake requires fewer iterations for the first frame in which the object is being acquired, thus reducing the processing time. This not only reduces processing time but also makes it accurate, as the initial contour fits readily onto the object. The progression of the snake onto future frames is also made accurate and fast due to the presence of the DoG energy parameter in the minimization equation. The method also works when an object being tracked stops moving and becomes static in the scene. Addition or removal of contour coordinates into the AC allows the contour to fit onto the moving object precisely.

In future work there is a requirement to design and modify the model for multiple object localisation and to cases where there is requirement to differentiate between multiple objects interacting with each other. We anticipate that with the improvement in accuracy of the AC Snake method it will also be suitable for object selective segmentation and tracking which is applicable to many industrial and security applications.

## References

- [1] Michael Kass, Andrew Witkin, and Demetri Terzopoulos, "Snakes: Active Contour Models", International Journal of Computer Vision, Volume 1, 1988, pp. 321-331.
- [2] Chenyang Xu, Jerry L. Prince, "Snakes, Shapes, and Gradient Vector flow", IEEE Transactions on Image processing, Vol.7, No 3, March, (1998), pp. 359-369
- [3] F. Mohanna and F. Mokhtarian, "Improved curvature estimation for accurate localization of active contours," in Proc. International Conference on Image Processing (ICIP'01), vol. 2, pp. 781-784, Thessaloniki, Greece, October 2001.
- [4] Min hu, Xijian Ping, Yihong Ding, "Automated Cell Nucleus Segmentation using Improved Snake", International Conference on Image Processing, Volume 4, pp. 2737 - 2740 (ICIP), October (2004).
- [5] S. Lefevre, J.G.Gerard, A.Piron, N.Vincent,"An Extended Snake model for Real-time multiple Object tracking", RFAI publication: International workshop on Advanced concepts for Intelligent vision systems, Ghent, Belgium, pp. 268-275, September 2002.
- [6] D. Williams, M. Shah, "A Fast Algorithm for Active Contours and Curvature Estimation", Computer Vision Graphics and Image Processing: Image Understanding, Vol.55, pp. 14-26, (1992).
- [7] J. Hernandez, F. Prieto, T. Redarce, "Fast Active Contours for Sampling", CERMA'06 Conference, IEEE Computer Society, Volume 2, pp. 9-13, September (2006).
- [8] M. Writh, D. Nikitenko, J. Lyon, "Segmentation of the Breast region in Mammograms using a rule based fuzzy reasoning algorithm", ICGST International Journal of graphics, vision and image processing, Volume 5, Issue 2, Jan 2005.
- [9] W.E.S. David, M. Honea and G. Bilbro, "Active Contours using a potential filed", ICPR02: International Conference on Pattern Recognition, Volume 2, pp.20757, August (2002).
- [10] H. Yang, Y. Tan, J. Tian, J. Liu, "Accurate Dynamic Scene Model for Moving Object Detection", ICIP 2007, IEEE, Volume 6, pp. 157-160, September (2007)
- [11] C. P. Lee, W. Snyder, C. Wang, " Supervised Multispectral Image Segmentation using Active Contours", Proceedings of the 2005 IEEE International Conference on Robotics and Automation, Barcelona, Spain, pp. 4242-4247, April, (2005).
- [12] Farag Cao, Y. Rose, D.M. Delp, E. J, "On empirical estimation of the parameters of edge enhancement filters", International Conference on System, Man and Cybernetics, Volume 1, pp. 346-350, October 1992.
- [13] Rajeev Ratan, Sanjeev Sharma, S.K. Sharma, "Brain tumor detection based on multi-parameter MRI image analysis", ICGST International Journal of Graphics, vision and Image processing, Volume 9, issue 3, June 2009.
- [14] 'CAVIAR' test case scenarios, July 2003 & Jan 2004.  
<http://homepages.inf.ed.ac.uk/rbf/CAVIARDATA>  
 1/
- [15] Y. Rathi, N. Vaswani, A. Tannenbaum, and A. Yezzi, "Particle Filtering for Geometric Active Contours and Application to Tracking Deforming Objects," IEEE Int'l Conf. Computer



- Vision and Pattern Recognition, vol. 2, pp. 2-9, 2005.
- [16] G. Papandreou, and P. Maragos, "Multigrid geometric active contour models", IEEE transaction on image processing, vol. 16, no. 1, January 2007.
- [17] T.F. Chan and L.A. Vese, "Active Contour without Edges", IEEE transactions on Image processing, vol 10, no 2, February 2001.
- [18] John Melonakos , Eric Pichon , Sigurd Angenent , Allen Tannenbaum, Finsler Active Contours, IEEE Transactions on Pattern Analysis and Machine Intelligence, v.30 n.3, p.412-423, March 2008.

## Biographies



**Mr Nagachetan Bangalore** is currently a researcher at the University of Sussex pursuing a Doctor of Philosophy degree in intelligent image processing using Active Contours. He also gained his MSc degree in Satellite Communication and Space systems from the

University of Sussex in 2006. He graduated with a Bachelor of Engineering degree in Electronics and Communications at Vishveshwaraiah Technological University, India. He has a keen interest in the field of digital signal and image processing, object tracking, pattern recognition and quantum physics. He is a member of the British Machine Vision Association (BMVA) and the Institution of Engineering and Technology.



**Dr Rupert Young** is currently a Reader at the University of Sussex; he graduated from Glasgow University, from where he also gained his PhD in coherent optical signal processing. Since 1995 he has been with the School of

Engineering and Design, University of Sussex. He has published over 200 refereed journal and conference papers on various aspects of digital signal and image processing, pattern recognition and electro-optics. He is a member of the Society of Photo-Optical and Instrumentation Engineers and the Optical Society of America.



**Dr Philip Birch** has published widely in image processing and recognition journals. Dr Birch is a lecturer at the University of Sussex. He has made major contributions to the research group in optoelectronics and image processing, he spent 3 years working as a project manager in a start-up company called Spiral Scratch Ltd, where *inter alia*, he acted as the research coordinator with Liverpool and Sheffield Hallam Universities. His leadership in 3D optical depth measurement and image processing for tracking has resulted in two products that are currently being taken to market and is also patented. He continues to support this start-up company via a new project with Sussex University. He is a member of OSA, IEEE and BMVA.



**Professor C. R. Chatwin** holds the Chair of Engineering, University of Sussex, UK; where, *inter alia*, he is the Research Director of the "IIMS Research Centre" and the Laser and Photonics Systems Engineering Group. At Sussex he is a member of the University: Senate, Council and Court. He has published widely in image processing journals and filed several patents. Much of his research has been for commercial companies solving difficult real world machine vision problems. He is also a member of the Institution of Electrical and Electronic Engineers, the British Computer Society, the Association of Industrial Laser Users. He is a Chartered Engineer, Euro-Engineer, International Professional Engineer, Chartered Physicist, Chartered Scientist and a Fellow of the Institution of Electrical Engineers, the Institution of Mechanical Engineers, the Institute of Physics and the Royal Society for Arts, Manufacture and Commerce.





## Modified Fisher Face Approach for Robust Biometric Recognition System

Aba M. Patil<sup>1</sup>, Satish R. Kolhe<sup>1</sup>, Pradeep M. Patil<sup>2</sup> and Milind E Rane<sup>2</sup>

<sup>1</sup>*North Maharashtra University, Jalgaon, India*

<sup>2</sup>*Vishwakarma Institute of Technology, Pune, India*

### Abstract

In this paper, a person is identified with face as a biometric feature using modified fisher face and fuzzy fisher face. The premise of this paper is to introduce modified fisher face, fuzzy fisher face and include gradual level of assignment to class being regarded as a membership grade which helps to improve recognition results. Performance of the said system is compared with traditional fisher face methods using Fisher's linear discriminant analysis. For all these methods of face recognition an assumption was made about the same level of relevance of each face to the corresponding category. The comprehensive experiments completed on ORL and Yale face databases show improved recognition rates and reduced sensitivity to variations between face images caused by changes in illumination and viewing directions.

**Keywords:** *Linear discriminant analysis, fisher face, fuzzy fisher face, face recognition*

### 1. Introduction

Humans can easily recognize faces, spoken words, handwritten or printed digits, images and many other things in everyday life. If there are a limited number of categories or classes then recognition performance may be improved; however, the same might not be very efficient if several categories are present. Face recognition is largely motivated by the need for surveillance and security, telecommunication and digital libraries, human-computer intelligent interaction, and smart environments [1 - 4]. In practice, face recognition is a very difficult problem due to a substantial variation in light direction, different face poses, and diversified facial expressions. A good face recognition methodology should consider representation as well as classification issues, and a good representation method should require

minimum manual annotations. Face recognition depends heavily on the particular choice of features used by the classifier [5]. One usually starts with a given set of features and then attempts to derive an optimal subset of features leading to high recognition performance with the expectation that similar performance can also be displayed on future trials using unseen test data. The most well known classification techniques used for face recognition are those of eigenface [6] and fisher face [7]. The eigenface method relies on a transformation of feature vectors by utilizing principal components and is referred to as principal component analysis (PCA) used to derive a starting set of features; the other naming used there is the Karhunen–Loeve (KL) expansion. In essence, the PCA dwells on a linear projection of a high-dimensional face image space into a new low-dimensional feature space. The major problem coming with the use of the eigenface technique is that it can be affected by variations in illumination conditions and different facial expressions. It is also worth stressing that the PCA is oriented toward the representation in low-dimensional spaces but not necessarily optimal in terms of face classification. Applying PCA technique to face recognition, Turk and Pentland developed a well-known Eigenface method. The Eigenface method, however, does not consider the classification aspect, as it is based on the optimal representation criterion in the sense of mean-square error. To improve the PCA standalone classification performance, one needs to combine further this optimal representation criterion with some discrimination criterion. One widely used discrimination criterion in the face recognition community is the Fisher linear discriminant (FLD), or linear discriminant analysis (LDA) [9], a well-known technique for dimensionality reduction. The second



well-known approach coming under the name of fisher face is insensitive to large variation in the conditions already enumerated above. It uses both PCA and FLD. It is worth stressing that by maximizing the ratio of between-scatter matrix and within-scatter matrix, FLD produces well separated classes in a low-dimensional subspace, even under severe variation in lighting and facial expressions. There are various enhancements made to FLD direct LDA, uncorrelated discriminant transformation [8], most discriminating feature [9]. In LDA, the dimensional embeddings are reduced in such a way that the orientation of the projected data of classes on an arbitrary line or space is well-separated from each other. There are some limitations in applying LDA directly viz. within class scatter matrix can become singular due to high dimensionality of original feature vectors in comparison with low number of training vectors available. To overcome this limitation, a number of authors have proposed the use of class-independent PCA prior to LDA in the feature extraction stage. Swets et al. [11] showed two stage PCA plus LDA method where PCA is first used for dimension reduction so as to make within class scatter matrix non-singular before the application of LDA especially when training samples are scarce. Belhumeur et al. [12] proposed a projection method which is based on LDA and PCA techniques for face recognition. In their technique class-independent PCA is first reduce the original space and then LDA is applied to reduce the dimension. Zhao et al. [13,14] demonstrated a technique based on the combination of LDA and PCA. A complete Kernel Fisher discriminant (KFD) was introduced to implement kernel PCA plus LDA strategy by Yang et al. [15] after KFD implementation by Mika et al. [16]. Wu et al. [17] presented a direct LDA method that is applicable to small sample size problems. Jian et al. [18] suggested subspace algorithm for determining the optimal projection for LDA that addressed two LDA problems viz. "small sample size" and "illumination and pose variations". Xiao gang et al. [19] then presented a unified framework using PCA, LDA and Bayes techniques for face recognition. Ye et al. [20] showed generalized optimization criteria based on pseudo inverse for discriminant analysis to address under sample problems.

Organization of this paper is described as below: Section (2) provides a well-known technique of fisher face. Section (3) describes a proposed modified fisher face and fuzzy fisher face approach. Section (4) reports on comprehensive simulation results completed for several commonly used face

databases such as ORL, and Yale. Finally, concluding comments and references are included.

## 2. Conventional method of face recognition using fisher face approach

FLD is a popular discriminant criterion that measures the between-class scatter normalized by the within-class scatter. Let  $\omega_1, \omega_2, \dots, \omega_L$  and  $N_1, N_2, \dots, N_L$ , denote the number of classes and the number of images within each class, respectively. Let  $M_1, M_2, \dots, M_L$  and  $M$  be the means of the classes and the grand mean. The within- and between-class scatter matrices,  $S_\omega$ ,  $S_b$  are defined as follows:

$$S_\omega = \sum_{i=1}^L p(\omega_i) \mathbb{E}\{(Y^{(p)} - M_i)(Y^{(p)} - M_i)^T |_{\omega_i}\} \quad (1)$$

$$S_b = \sum_{i=1}^L p(\omega_i) \mathbb{E}(M_i - M)(M_i - M)^T$$

(2)

Where,  $p(\omega_i)$  is *a priori* probability,  $S_\omega, S_b \in mR$ , and L denotes the number of classes. FLD derives a projection matrix that maximizes the ratio  $\frac{|P^T S_b P|}{|P^T S_\omega P|}$ .

This ratio is maximized when  $P$  consists of the eigenvectors of the covariance matrix  $A$

$$S_\omega^{-1} S_b \psi = \psi \Delta \quad (3)$$

where  $\psi, \Delta \in R^{m \times m}$  are the eigenvector and Eigen value matrices of  $S_\omega^{-1} S_b$  respectively.

## 3. Proposed Algorithm

### a) Modified Fisher Linear Discriminant approach

The Modified Fisher linear discriminant Model (MFLD) improves the generalization capability of FLD by decomposing the FLD procedure into a simultaneous diagonalization of the two within- and between-class scatter matrices. The simultaneous diagonalization is step wisely equivalent to two operations whitening the within class scatter matrix and applying PCA on the between-class scatter matrix using the transformed data.

To achieve the enhanced performance, MFLD preserves a proper balance between the need that the selected eigen values (corresponding to the principal components for the original image space) account for most of the spectral energy of the raw data, i.e., representational adequacy, and the requirement that the eigenvalues of the within class scatter matrix (in the reduced PCA space) are not



too small, i.e., better generalization. The choice of the range of principal components ( $m$ ) for dimensionality reduction takes into account both the spectral energy and the magnitude requirements. The eigenvalue spectrum of the covariance matrix provides a good indicator for meeting the energy criterion; one needs then to derive the eigenvalue spectrum of the within-class scatter matrix in the reduced PCA space to facilitate the choice of the range of principal components so that the magnitude requirement is met.

The stepwise FLD procedure derives the eigenvalue and eigenvectors of  $S_{\omega}^{-1}S_b$  as the result of the simultaneous diagonalization of  $S_{\omega}$  and  $S_b$ .

$$S_{\omega}v\Xi = \Xi\Gamma \text{ and } \Xi^T\Xi = 1 \quad (4)$$

$$\Gamma^{-1/2}\Xi^T S_{\omega}\Xi\Gamma^{-1/2} = 1 \quad (5)$$

Where,

$\Xi, \Gamma \in R^{m \times m}$  are the eigenvector and the diagonal eigenvalue matrices of  $S_{\omega}$  respectively

Different spectra are obtained corresponding to different number of principal components utilized. Tread off is to be find to optimize the behavior of the trailing eigenvalues in the reduced PCA space with the energy criteria for the original image space. The eigen vectors derived are as shown in figure 1. After the feature vector is derived, MFLD first diagonalizes the within-class scatter matrix  $S_{\omega}$  using (4) and (5).  $\Xi$  and  $\Gamma$  are the eigenvector and the eigenvalue matrices corresponding to the feature vector  $Y^{(p)}$ . MFLD proceeds then to compute the between-class scatter matrix as follows:

$$\Gamma^{-1/2}\Xi^T S_b\Xi\Gamma^{-1/2} = K_{\phi} \quad (6)$$

Diagonize now the new between-class scatter matrix  $K_b$

$$K_b\Theta = \Theta\gamma \text{ and } \Theta^T\Theta = I \quad (7)$$

Where,

$\Theta, \gamma \in R^{m \times m}$  eigenvector and diagonal eigenvalue matrices of  $K_b$  respectively



Figure 1: Eigen vector images.

The overall transformation matrix of MFLD is now defined as follows

$$T = \Xi\Gamma^{-1/2}\Theta \quad (8)$$

#### b) Fuzzy Fisher Linear Discriminant (FFLD) approach

The fisher face presented in the previous section has exhibited a substantial advantage over the PCA



as far as classification aspects are concerned. But in order to improve the same technique, an alternative can be used which sophisticate the use of class assignment of patterns (faces). Further to refine classification results so that they could affect the within-class and between-class scatter matrices and enhance the performance of the classifier. Having this in mind, an obvious choice is to look at the fundamental results available in the setting of fuzzy nearest neighbor classifiers.

Given a set of feature vectors transformed by the PCA,  $X = \{x_1, x_2, \dots, x_N\}$ , a fuzzy  $c$ -class partition of these vectors specifies the degrees of membership of each vector to the classes. The partition matrix denoted by  $\mu_{ij}$  for  $i=1, 2, \dots, c$  and  $j=1, 2, \dots, N$  satisfies two obvious properties

$$\sum_{i=1}^c \mu_{ij} = 1 \quad (9)$$

$$0 < \sum_{j=1}^N \mu_{ij} < N \quad (10)$$

$$\mu_{ij} = \begin{cases} 0.51 + 0.49(n_{ij} / k) & \text{if } i = \text{the same as the label of the } j^{\text{th}} \text{ pattern} \\ 0.49(n_{ij} / k) & \text{if } i \neq \text{the same as the label of the } j^{\text{th}} \text{ pattern} \end{cases} \quad (11)$$

The first condition helps us assure sound mathematical tractability. The computations of the membership degrees are realized through a sequence of steps:

*Step 1:* Compute the Euclidean distance matrix between pairs of feature vectors in the training.

*Step 2:* Set diagonal elements of this matrix to infinity (practically place large numeric values there).

*Step 3:* Sort the distance matrix (treat each of its columns separately) in an ascending order. Collect the class labels of the patterns located in the closest neighborhood of the pattern under consideration (as we are concerned with " $k$ " neighbors, this returns a list of " $k$ " integers).

*Step 4:* Compute the membership grade to class  $i$  for  $j^{\text{th}}$  pattern using equation (11). In the expression (11),  $n_{ij}$  stands for the number of the neighbors of the  $j^{\text{th}}$  data (pattern) that belong to the  $i^{\text{th}}$  class. After the examination of the membership location formula we conclude that the method attempts to "fuzzify" or refine the membership grades of the labeled patterns.

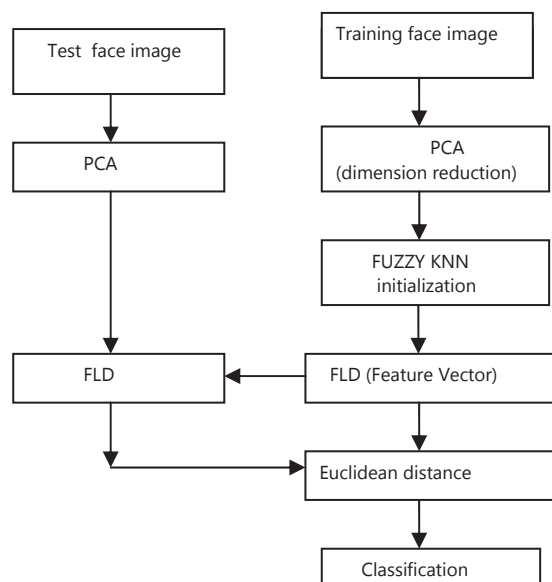


Figure 2: A general flow of computing for the fuzzy fisher face method.





Figure 3: Fuzzy fisher faces

#### 4. Results and Discussions

The algorithms are tested on Yale, and ORL database to compute recognition rate. The recognition rate for above proposed algorithms is carried out in two parts as in-database and out-database. In database means training images and testing images are the same whereas for out-database training images and testing images are different. The result obtained for in-database are listed in table I and result obtained for out-database are listed in table II

TABLE I. IN-DATABASE RECOGNITION RATE

Face database	Recognition rate		
	FLD	MFLD	FFLD
ORL	95%	100%	100%
Yale	94%	100%	100%

MFLD and FFLD have 100% identification rate. In contrast, FLD has only 94% for Yale database and 95% for ORL database. It means that FLD doesn't learn well when we train the input images. In fact, FLD only maximizes the distance of each subject. As a result, these projected coefficients of different subject could be distributed in the same area and FLD system cannot identify these faces.

TABLE II: OUT-DATABASE RECOGNITION RATE

Face database	Recognition rate		
	FLD	MFLD	FFLD
ORL	75.5	90.7	95.5
Yale	83.45	91.4	94.8

The MFLD and FFLD technique outperforms in identifying a person with face as a biometric feature as compared with traditional FLD. The experimental results show improved recognition rates and reduced sensitivity to variations between face images caused by changes in illumination and viewing directions.

#### 5. Conclusions

We have proposed a generalized version of the fisher face method for face recognition by including refined information about class membership of the binary labeled faces (patterns). By doing this we were able to reduce sensitivity of the method to substantial variations between face images caused by varying illumination, viewing conditions, and facial expression. Experimental results showed a consistently better classification rates in comparison to other "standard" methods such as Eigen face and fisher face when applied to ORL, Yale.



**Acknowledgements:** This work is carried out under the grant "Engg-48" given by BCUD, University of Pune. Authors are thankful to BCUD University of Pune for their financial support.

## References

- [1] R. Chellappa, C. L.Wilson, and S. Sirohey, "Human and machine recognition of faces: A survey," *Proc. IEEE*, vol. 83, pp. 705–740, May 1995.
- [2] J. Daugman, "Face and gesture recognition: Overview," *IEEE Transaction Pattern Analysis and Machine Intelligence*, vol. 19, no. 7, pp. 675–676, 1997.
- [3] A. Pentland, "Looking at people: Sensing for ubiquitous and wearable computing," *IEEE Transaction Pattern Analysis and Machine Intelligence*, vol. 22, pp. 107–119, Jan. 2000.
- [4] A. Samal and P. A. Iyengar, "Automatic recognition and analysis of human faces and facial expression: A survey," *Pattern Recognition*, vol. 25, no. 1, pp. 65–77, 1992.
- [5] C. Liu and H. Wechsler, "Evolutionary pursuit and its application to face recognition," *IEEE Transaction Pattern Analysis and Machine Intelligence*, vol. 22, pp. 570–582, June 2000.
- [6] M. Turk and A. Pentland, "Eigenfaces for recognition," *J. Cogn. Neurosci.*, vol. 13, no. 1, pp. 71–86, 1991.
- [7] P.N. Belhumeur, J.P. Hespanha, D.J. Kriegman, "Eigenfaces vs. fisherfaces: recognition using class specific linear projection," *IEEE Transaction Pattern Analysis and Machine Intelligence*, 19 (7) (1997) 711–720.
- [8] M. Kirby and L. Sirovich, "Application of the Karhunen-Loeve procedure for the characterization of human faces," *IEEE Transaction Pattern Analysis and Machine Intelligence*, vol. 12, pp. 103–108, Jan. 1990.
- [9] R. A. Fisher, "The use of multiple measures in taxonomic problems," *Ann. Eugenics*, vol. 7, pp. 179–188, 1936.
- [10] R.O. Duda, P.E. Hart, "Pattern Classification and Scene Analysis," Wiley, New York, 1973.
- [11] D.L. Swets, J. Weng, "Using discriminative eigenfeatures for image retrieval," *IEEE Transaction Pattern Analysis and Machine Intelligence*, 18 (8) (1996) 831–836.
- [12] P.N. Belhumeur, J.P. Hespanha, D.J. Kriegman, Eigenfaces vs. fisherfaces: recognition using class specific linear projection, *IEEE Transaction Pattern Analysis and Machine Intelligence*, 19 (7) (1997) 711–720.
- [13] W. Zhao, R. Chellappa, P.J. Phillips, "Subspace linear discriminant analysis for face recognition," Technical Report CAR-TR-914, Center for Automation Research, University of Maryland, College Park, 1999.
- [14] W. Zhao, R. Chellappa, N. Nandhakumar, "Empirical performance analysis of linear discriminant classifiers," *Proceedings of the IEEE Conference on Computer Vision and Pattern Recognition*, 1998, pp. 164–169.
- [15] J. Yang, A.F. Frangi, J.-y. Yang, D. Zhang, J. Zhong, "KPCA plus LDA: a complete kernel Fisher discriminant framework for feature extraction and recognition," *IEEE Transaction Pattern Analysis and Machine Intelligence*, 27 (2) (2005) 230–244.
- [16] S. Mika, G. Rätsch, J. Weston, B. Schölkopf, A. Smola, K.-R. Müller, "Constructing descriptive and discriminative nonlinear features: Rayleigh coefficients in kernel feature spaces," *IEEE Transaction Pattern Analysis and Machine Intelligence*, 25 (5) (2003) 623–628.
- [17] X.-J. Wu, J. Kittler, J.-Y. Yang, K. Messerm S. Wang, "A new direct LDA (D-LDA) algorithm for feature extraction in face recognition," *Proceedings of the International Conference on Pattern Recognition* vol. 4, 2004, pp. 545–548.
- [18] H. Jian, P.C. Yuen, C. Wen-Sheng, "A novel subspace LDA algorithms for recognition of face images with illumination and pose variations," *Proceedings of the International Conference on Machine Learning and Cybernetics*, vol. 6, 2004, pp. 3589–3594.
- [19] W. Xiaogang, T. Xiaoou, "A unified framework for subspace face recognition," *IEEE Transaction Pattern Analysis and Machine Intelligence*, 26 (9) (2004) 1222–1228.
- [20] J. Ye, R. Janardan, H.P. Cheong, P. Haesun, "An optimization criterion for generalized discriminant analysis on undersampled problems," *IEEE Transaction Pattern Analysis and Machine Intelligence*, 26 (8) (2004) 982–994.



## Biographies



**Aba M. Patil:** has completed BE in Industrial Electronics and ME in Electronics from Amaravati University. He is presently working Professor and Head of Dept at J T Mahajan College of Engineering, Faizpur, Maharashtra. Also

he is Dean, Faculty of Engineering and Technology at North Maharashtra University Jalgaon. His area of interest includes Image processing, Biometrics recognition and Pattern recognition.



**Milind E Rane :** received his BE degree in Electronics engineering from University of Pune and M Tech in Digital Electronics from Visvesvaraya Technological University, Belgaum, in 1999 and 2001 respectively..His research interest includes image processing, pattern recognition and Biometrics Recognition



**Satish R Kolhe :** received his BE degree in computer engineering from Amaravati University and M Tech in Engineering Systems from Dayalbagh Educational Institute, Agra in 1991 and 1994 respectively. He completed his Ph D studies in August 2007.His research interest includes neural networks, image processing and pattern recognition



**Pradeep Mitharam Patil,** was born in Bhusawal, District Jalgaon, Maharashtra, India on December 13, 1966. He received B. E. (Electronics) degree in 1988 from Amravati University, Amravati, India and M. E.

(Electronics) degree in 1992 from Marathwada University, Aurangabad, India. From 1988 to 2002 he worked as Lecturer and Assistant Professor in Electronics department at various engineering colleges in Pune University, India. He received the Ph.D. degree in Electronics and Computer Engineering in 2004 at Swami Ramanand Teerth Marathwada University. He is member of various professional bodies like IE, ISTE, IEEE and Fellow of IETE. Presently he is working as Professor of Electronics Department at Vishwakarma Institute of Technology, Pune, India. His research areas include pattern recognition, fuzzy neural networks and power.







## An automated System for Liver CT Enhancement and Segmentation

M. Usman Akram, Aasia Khanum and Khalid Iqbal

*Department of Computer Engineering*

*College of Electrical and Mechanical Engineering*

National University of Sciences and Technology, Pakistan

usmakram@gmail.com, [khalid, aasia]@ceme.nust.edu.pk

### Abstract

In this paper we propose a method for automated liver segmentation from CT images that is invariant in terms of size, shape and intensity values. The system consists of three stages. In the first stage of the computerized system, the CT liver image is acquired and preprocessing is done to remove the noise and to enhance the image. In the second stage, liver region is segmented from the liver CT image. In the third stage, post processing enhancement is done on the segmented liver region to enhance the contrast of liver region. Experimental results show that our proposed technique segments the liver region with accuracy.

**Keywords:** Liver CT, Automatic Segmentation, Postprocessing, enhancement.

### 1 Introduction

As a medical imaging technique, computed tomography (CT) is quite useful for doctors to analyze the pathological changes of the biological organs. In order to reduce deaths, the diseases must be detected accurately in the early stage. The main problem of liver segmentation from CT images is related to low contrast between liver and nearby organs intensities. Liver sometimes presents in different dimensions and makes the detection and segmentation even more difficult.

The liver is a vital organ with vascular, metabolic, secretory and excretory functions. It is extensively perfused, and during liver surgery, special care has to be taken in order to avoid bleedings. Imaging techniques such as computed tomography (CT), magnetic resonance imaging (MRI), or positron emission tomography (PET) are nowadays standard instruments for the diagnosis of liver pathologies such as cirrhosis, liver cancer, fulminant hepatic failure. Among these techniques, CT images are often preferred by diagnosticians since they provide a more accurate anatomical information about the visualized structures, thanks to their higher signal-to-noise ratio and better spatial resolution.

The liver cancer is one of the most common internal malignancies also one of the leading death causes. Currently, the confirmed diagnosis used widely for the liver cancer is needle biopsy. The needle biopsy, however, is an invasive technique and generally not recommended [2]. Therefore, computed tomography (CT) has been identified as accurate non-invasive imaging modalities in the diagnosis of the liver cancer.

Many clinical applications for computer aided diagnosis require medical images to be segmented. For example, planning of liver tumor embolization, ablation and surgical resection require precise segmentation of the liver from CT images. Due to the complex shape and the large size of this organ, the manual segmentation is time consuming. In order to increase the efficiency of the clinical work, automatic segmentation methods are needed. A computerized liver CT segmentation system should take less time and should segment the liver accurately. It should be consistent and should provide a system to radiologist which is self-explanatory and easy to operate.

There are many approaches for liver image segmentation. Most of the automated liver segmentation methods are based on region-growing [8], active contour or surface [1],[3], level-set [5], or voxel classification algorithms [7], which were adapted to liver segmentation and connected with some pre- and post-processing operations [10]. Since the intensity as well as the boundary gradient of the liver varies from one part to the other, the methods are usually constrained with statistical shape [4],[9],[11] or volume model [6], [12]. Zalthen et al. [13] used a voxel-based region-growing algorithm to extract the portal vein, but the algorithm requires a manually set initial seed point and is therefore not fully automatic. The portal vein skeleton was calculated utilizing methods of Malandain and Bertrand [14,15] and is corrected by pruning vessel segments that do not confirm with a set of predetermined properties. There are also many liver image enhancement methods. Histogram equalization (HE) is normally used to improve contrast, which generates an image whose pixels of gray levels are as equal as possible. But for the original CT image,



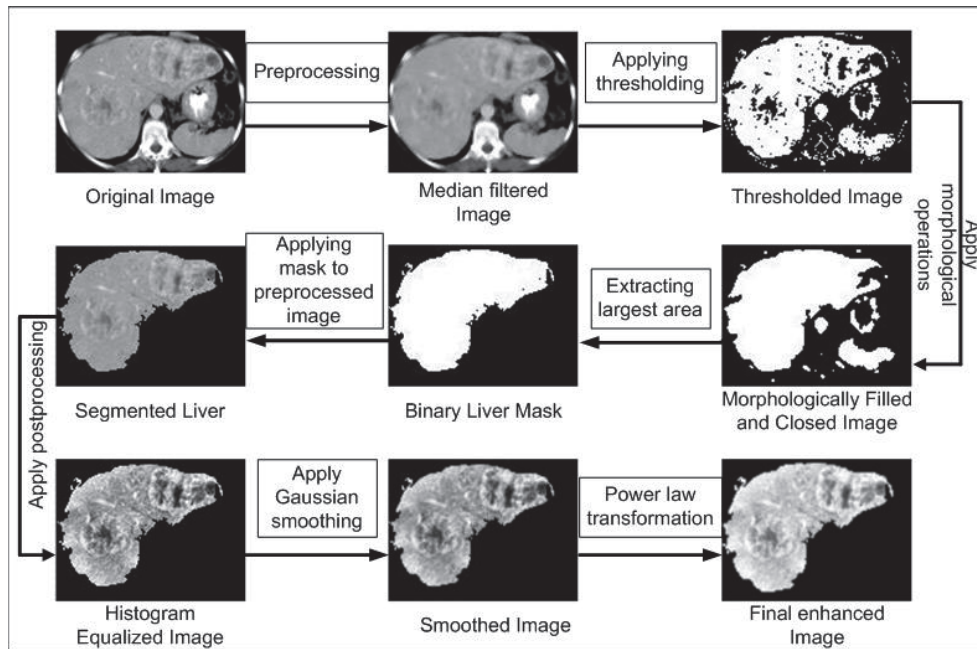


Figure 1: Flow diagram of Computerized System for Liver CT Segmentation and Enhancement

HE often makes the whole image too bright to see. In recent years, contrast limited adaptive histogram equalization(CLAHE) has been used in medical images processing. However, it is easy to introduce artificial boundaries at the region where gray levels have great differences.

A computerized liver CT segmentation system should consist of multiple phases including noise removal, liver region segmentation and liver region enhancement. In this paper, we propose a computerized system for liver image segmentation. Our system segments the liver region by using three phases, pre processing, global threshold and post processing.

The paper is organized in four sections. In section 2, proposed method is explained. Section 2 also presents the step by step techniques required for computerized liver CT segmentation system. Experimental results of tests on the images and their analysis are given in Section 3 followed by conclusion in Section 4.

## 2 Proposed System

A systematic overview of the proposed technique is shown in figure 1. In summary, given a liver CT image, the first step removes the noise from the image, the second step segments the liver portion from the CT image and in the third step post processing using adaptive histogram equalization, gaussian smoothing and gray level transformations takes place. As a result of these steps, we get a final segmented and enhanced liver CT image. Figure 2 shows flowchart of proposed technique.

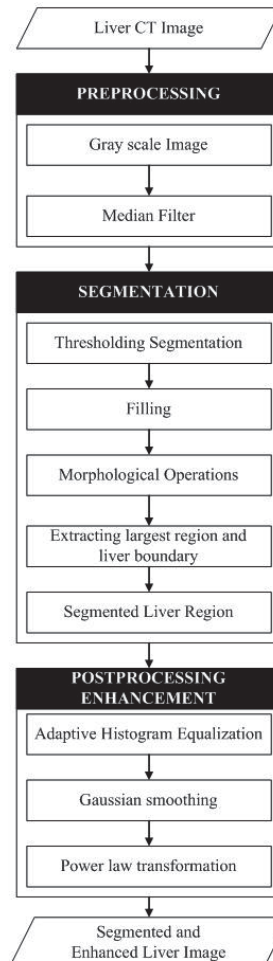


Figure 2: Flowchart of proposed technique



## 2.1 Preprocessing

Preprocessing of liver CT image is the first step in our proposed technique. Preprocessing of an image is done to reduce the noise and to enhance the image for further processing. The purpose of these steps is basically to improve the image and the image quality to get more surety and ease in segmenting the liver. Steps for preprocessing are as follows:

- Image is converted to gray scale.
- A 3x3 median filter is applied on liver CT image using equation 1 in order to remove the noise.

$$\bar{f}(x, y) = \text{median}_{(s,t) \in S_{xy}}\{g(s, t)\} \quad (1)$$

Figure 3 shows the original liver CT image and pre-processed image.

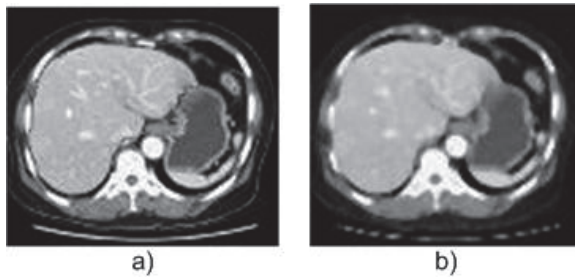


Figure 3: Preprocessing: a) Original Image b) Median Filtered Image

## 2.2 Liver Segmentation

After enhancing the liver CT image, the next step of our proposed technique is to segment the liver region from liver CT image. Segmentation is done to separate the image foreground from its background. Segmenting an image also saves the processing time for further operations which has to be applied to the image. We have used segmentation using a global threshold in order to segment the liver CT image. Afterwards some morphological operations are applied on the image to obtain the final segmented liver region. The basic steps for liver CT segmentation are as follows:

- Select a global threshold value for the whole CT image.
- Apply the threshold value to the preprocessed image to convert the image to binary and the thresholded image is obtained.
- Morphological close operation is applied on the thresholded image to fill in holes and small gaps in the image.
- Reserve the block whose area is the biggest and set the others to zero using 8-connected neighbors.

- The binary liver mask is obtained using the above step.
- Extract the liver boundary by setting a pixel to 0 if its 4-connected neighbors are all 1's, thus leaving only boundary pixels.
- Multiply the original liver CT image with the liver masked image to obtain the final segmented liver region with gray level values as those of original image.

Figure 4 shows the threshold image, filled image, image after applying morphological operations, liver mask image, boundary extracted image and final segmented image.

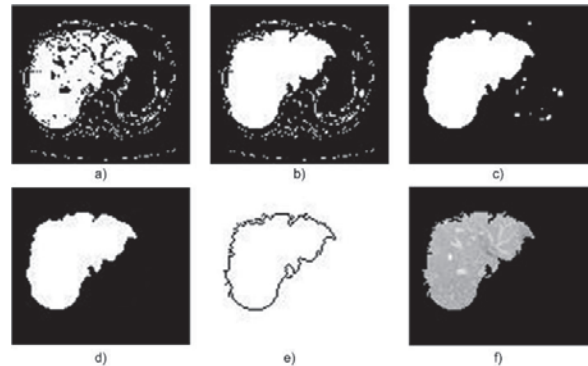


Figure 4: Segmentation: a) Thresholding, b) Morphological Filling, c) Morphological Closing, d) Binary Liver Mask, e) Liver Boundary, f) Segmented Liver Region

## 2.3 Postprocessing

After segmenting the liver region from liver CT image, several postprocessing operations are applied on the image to enhance the liver region so that area of focus can be clearly highlighted. These postprocessing operations include adaptive histogram equalization, gaussian smoothing and gray level transformations. The basic steps of postprocessing are as follows:

- Adaptive histogram equalization is applied on the segmented image. Adaptive histogram equalization is an image enhancement technique which is capable of improving the image contrast and brings out fine details of an image.
- A 7x7 gaussian low pass filter with  $\sigma=0.5$  is applied on the histogram equalized image using equation 2 in order to smooth the image.

$$h_g(x, y) = e^{-(x^2+y^2)/2\sigma^2} \quad (2)$$

- Power law transformation is applied on the smoothed image in order to adjust the gray levels of an image using equation 3.



$$s = cr^\gamma \quad (3)$$

where s is output gray level value, r is input gray level value, is gamma and it is a constant value but its value changes in different scenarios and c is the constant. The enhanced segmented liver region is obtained using the above enhancement techniques.

The enhanced segmented liver region is obtained using the above enhancement techniques. Figure 5 shows the adaptive histogram equalized image, smoothed image and power law transformation applied image.

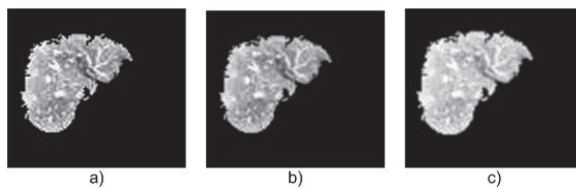


Figure 5: Postprocessing: a) Adaptive Histogram Equalization, b) Gaussian smoothing, c) Power law transformation

### 3 Experimental Results

The tests of proposed technique are performed with respect to the liver region segmentation accuracy using 100 CT images of different patients. The images are of size 512x512 pixels, eight bits per color channel. In order to check the accuracy of automated segmented liver region, liver region from all images is segmented manually by the hepatologist and oncologist. The manually segmented images are used as ground truth. The true positive fraction is the fraction of number of true positive (pixels that actually belong to liver region) and total number of liver region pixels in the CT image. False positive fraction is calculated by dividing false positives (pixels that don't belong to liver region) by total number of non liver region pixels in the CT image.

Figure 6 shows the experimental results for different liver CT images. It shows that proposed method have extracted the liver region accurately and enhanced the liver region to highlight the point of focus.

Table 1 summarizes the results of liver segmentation for CT images. It shows the results in terms of average accuracy and their standard deviation as compared with ground truth. Average accuracy is the fraction of pixels correctly classified.

### 4 Conclusion

Identification and segmentation of a liver from CT images is challenging due to the very low contrast be-

Table 1: Liver CT Segmentation Results

Parameter	Value
Average Accuracy	0.96
Standard Deviation	0.0017
Accurately Segmented	96%
Poorly Segmented	4%

tween the liver and other organs. In this paper liver segmentation and enhancement is done using CT images. The proposed method segments the liver using global threshold and then by identifying the largest area. Contrast of the liver region is improved by using adaptive histogram equalization and power law transformation. The proposed method is invariant in terms of size and shape of liver region. Experimental results show that our method performs well in enhancing, segmenting and extracting liver region from CT images.

### References

- [1] Bekes, Gy., Ny  l, L.G., M  t  , E., Kuba, A., Fidrich, M., 3D segmentation of liver, kidneys and spleen from CT images, Proceeding of the International Journal of Computer Assisted Radiology and Surgery, 2(1), pp.45-46, 2007.
- [2] E.L. Chen, P.C. Chung, C.L. Chen, H.M. Tsai, C.I. Chang, An automatic diagnosis system for CT liver image classification, IEEE Trans. Biomed. Eng., 45 (6), pp. 783-794, 1998.
- [3] Heimann, T., Wolf, I., Meinzer, H.P., Active shape models for a fully automated 3d segmentation of the liver - an evaluation on clinical data, In: Larsen, R., Nielsen, M., Sporring, J. (Eds.), MICCAI 4191 of LNCS. Springer-Verlag, pp.41-48, 2006.
- [4] Lamecker, H., Lange, T., Seebass, M., Segmentation of the liver using a 3D statistical shape model, ZIB-Report 04-09 Konrad-Zuse-Zentrum fur Informationstechnik, Berlin, 2004.
- [5] Pan, S., Dawant, B.M., Automatic 3D segmentation of the liver from abdominal CT images: a level-set approach, Proceedings of the SPIE 4322, pp. 128-138, 2006.
- [6] Park, H., Bland, P.H., Meyer, C.R., Construction of an abdominal probabilistic atlas and its application in segmentation, IEEE Transactions on Medical Imaging 22, 4, pp.483-492, 2003.
- [7] Pham, M., Susomboon, R., Disney, T., Raicu, D., Furst, J., A comparison of texture models for automatic liver segmentation, Proceedings of the SPIE 6512, 65124E., 2007.



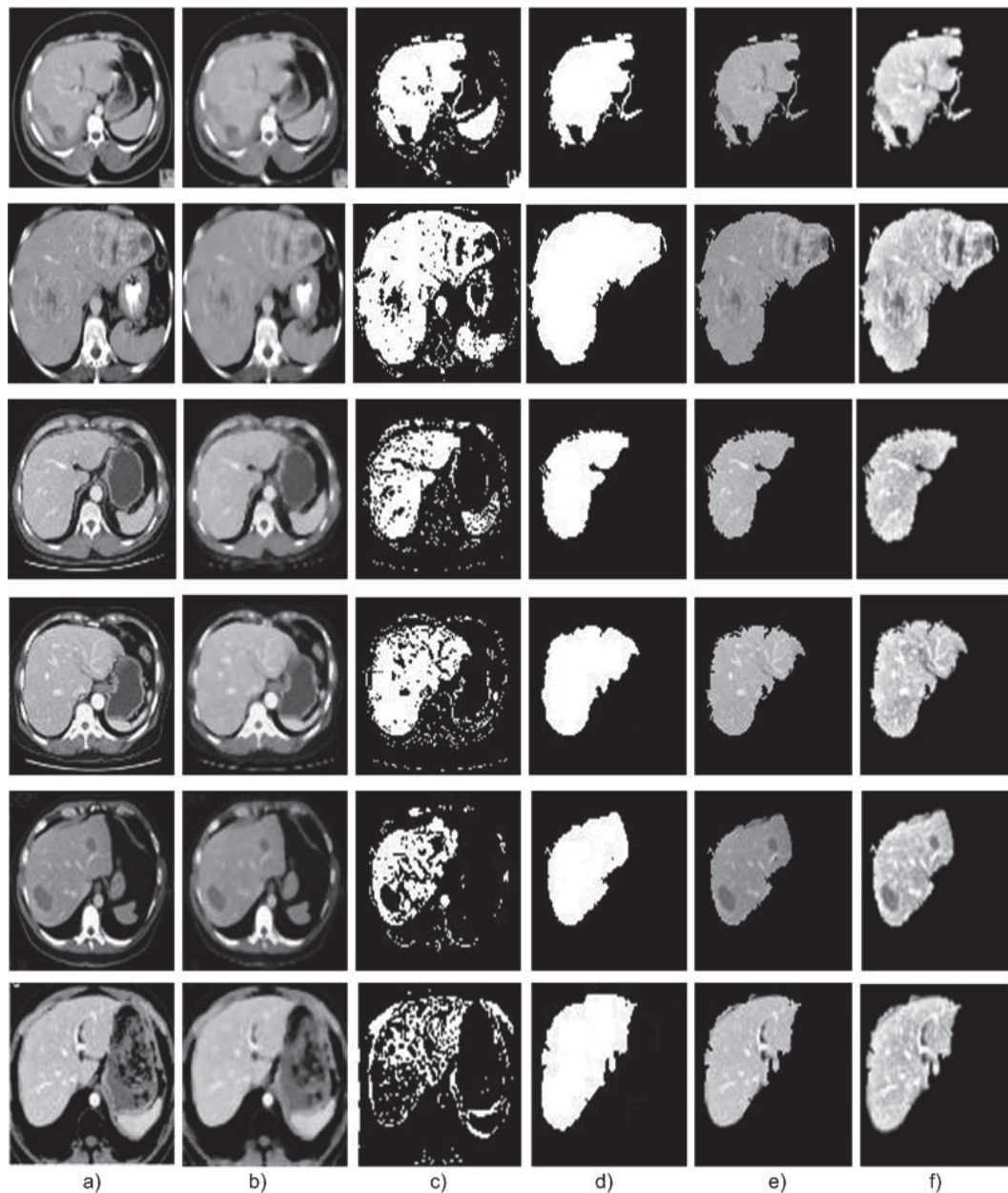


Figure 6: Experimental Results: a) Original Images, b) Preprocessing, c)Threshold Segmentation, d)Binary Liver Mask, e)Segmented Liver, f)Postprocessing



- [8] Pohle, R., Toennies, K.D., Segmentation of medical images using adaptive region growing, Proceedings of the SPIE Medical Imaging 4322, pp.1337-1346, 2001.
- [9] Slagmolen, P., Elen, A., Seghers, D., Loeckx, D., Maes, F., Haustermans, K., Atlas based liver segmentation using nonrigid registration with a B-spline transformation model, In: MICCAI 2007 Workshop Proceedings of the 3D Segmentation in the Clinic: a Grand Challenge, pp.196-206, 2007.
- [10] Soler, L., Delingette, H., Malandain, G., Mottagnat, J., Ayache, N., Koehl, C., Dourtheb, O., Malassagne, B., Smith, M., Mutter, D., Marescaux, J., Fully automatic anatomical, pathological, and functional segmentation from CT, Proceedings of the SPIE Medical Imaging 3979, pp.246-255, 2000.
- [11] Weese, J., Kaus, M., Lorenz, C., Lobregt, S., Tryuen, R., Pekar, V., Shape constrained deformable models for 3d medical image segmentation, In: Insana, M., Leahy, R. (Eds.), IPMI 2002 of LNCS, Springer-Verlag, pp.380-387, 2001.
- [12] Zhou, X., Kitagawa, T., Hara, T., Fujita, H., Zhang, X., Yokoyama, R., Kondo, H., Kanematsu, M., Hoshi, H., Constructing a probabilistic model for automated liver region segmentation using non-contrast X-ray torso CT images, In: MICCAI 4191 of LNCS, Springer-Verlag, pp.856-863, 2006.
- [13] C. Zahlten, et al., Portal vein reconstruction based on topology, European Journal of Radiology, 19 (2), pp.96-100, 1995.
- [14] G. Bertrand, G. Malandain, A new characterization of threedimensional simple points, Pattern Recognition Letters, 15 (3) , pp.175-196, 1994.
- [15] G. Malandain, G. Bertrand, N. Ayache, Topological segmentation of discrete surfaces, International Journal of Computer Vision, 10 (2), pp.183-197, 1993.

## Biographies



**M. Usman Akram** is a PhD student in department of computer engineering at College of Electrical and Mechanical Engineering, National University of Sciences and Technology, Pakistan. He has published more than 30 papers in journals and conferences of international repute. His research interests include biomedical engineering, image processing, machine learning and

pattern recognition.



**Asasia Khanum** holds a PhD degree in Software Engineering from the National University of Sciences and Technology (NUST), Pakistan. Currently she is working as an Assistant Professor at College of Electrical and Mechanical Engineering, NUST. She has published more than 20 papers in journals and conferences of international repute. Her research interests include application of intelligent techniques to multimedia processing, pattern recognition, data mining, software engineering, and cognitive computing.



**Khalid Iqbal** is Head of Computer Engineering Department in College of Electrical and Mechanical Engineering, National University of Sciences and Technology, Pakistan. He holds a PhD degree with majors in communication from Cranfield University UK. He has published a number of papers in journals and conferences of international repute. His research interests include digital signal processing, digital and wireless communication and MIMO systems.





## Content-Based Image Retrieval Using Templates of Medical Images

K.P. Ajitha Gladis<sup>1</sup>, K. Ramar<sup>2</sup> and Jestin Rajamony<sup>3</sup>

1, 3 CSI Institute of Technology, Thovalai, 2 Sri Vidhya College of Engg. and Tech., Virudhunagar.

ann\_aji@rediffmail.com, k\_ramar@yahoo.com, jestin\_br@yahoo.com

### Abstract

This paper proposes an efficient and novel content-based image retrieval framework, formalized using the higher level patterns present in the image. This novel approach combines the color and texture features of the image with its patterns to increase the retrieval rate. The low level wavelet sub band coefficients are clustered by an iterative approach to form the higher level semantically meaningful patterns. The optimum of horizontal or vertical forward and reverse histogram of the query that has best match with the database image histogram is treated as another reference feature to provide directionally invariant retrieval performance. The Sum of Squared Distance (SSD) similarity measure determines the close similarity between the database images and the query image. Experiments were performed on a diverse collection of reference images, and have shown that the proposed scheme can be efficiently and effectively applied for Content Based Image Retrieval (CBIR) from large databases. In view of the fact that medical images generally exhibit a standard pattern, the proposed framework could show better retrieval performance for medical images rather other natural images. The retrieval results demonstrated significant improvement in precision and recall with increased average retrieval rate, up to 97%.

**Keywords:** CBIR, Pattern, Modified fast Haar transform, Forward and reverse histogram, Iterative approach.

### 1. Introduction

With the rapid growth of digital technologies and the proliferation of World Wide Web, a huge amount of image databases are added into the digital image libraries every minute. To manage and search these large image collections effectively and efficiently, it poses significant technical challenges, and raises the necessity of constructing intelligent retrieval systems [1]. To date, the utilization of online images is limited due to the lack of effective search methods. Keyword-based searches [2] have been the dominating approach during the late 1970's. In keyword feature representation scheme [3], images should be accurately annotated manually before being stored. They can later be retrieved by searching for the corresponding keywords. This manual annotation process will be more tedious and expensive due to the regular increase in the size of image database. These facts limit the popularity of keyword based image retrieval technique.

Content-Based Image Retrieval (CBIR) scheme has been introduced in the early 1990's to overcome the difficulty of manual annotation and to automate the process of image retrieval [4], [5]. Most CBIR systems represent images by summarizing their low level visual image features such as color, texture, and shape. These features are automatically extracted from the images, and are used to find similar images [6] during the retrieval process. A key issue in CBIR system is feature extraction. Feature with respect to image is a piece of relevant information that indicates certain visual properties of an image either globally for the whole image, or locally for



objects or region of interest. Two major approaches [7] namely spatial, and transform domain-based methods can be identified in CBIR system to extract the image features: first approach usually uses the pixel features like color and shape. Among this color is the most used feature [8] for indexing. The second approach uses the transformed data [9] to extract some higher level features. Wavelet-based methods [10], [11] provide better local spatial information in transform domain.

This paper proposes an innovative approach that utilizes the similarity measures, defined over higher level patterns that are associated with clusters of low level image feature spaces. The focus on color images is made in HSV color space model [12], which is closely related to human visual perception than RGB color space model. The modified Haar wavelets [13] are used to extract the wavelet sub band coefficients because of their fast computation and regularity. The approximation (LL) band of the wavelet recognizes the patterns present in the image using an iterative approach. The optimum among the horizontal or vertical bins in the forward and reverse direction is determined. The combination of different wavelet decomposition planes and histograms increase the number of features, which in turn improves the retrieval accuracy. During the retrieval process, the feature vector of the query image is computed and matched with those features in the feature database. The SSD distance measure [14] is used in this paper for similarity matching.

The rest of this paper is structured as follows. A review of the related work done in the areas of computer vision and image processing are presented in section 2. The proposed methodology is dealt in detail under section 3. In section 4 the experimental results are depicted and discussed. Finally, the conclusions and issues for future research are given under section 5.

## 2. Survey – Related work

A typical CBIR system views the query image, and images in the database as a collection of features, and grades the relevance between the query image and any image in the database in

proportion to a similarity measure calculated from the features. In this context, the features or signatures of images characterize the content of images. According to the scope of representation, features may be categorized into two: global features, and local features. In global feature representation the image is considered as a whole [15], [16] for feature extraction, whereas the sub images [17], segmented regions [18], [19], or pixel points of interest [20] are considered in local feature representation.

Feature is the characteristic of an image that can capture the visual property of the image. CBIR systems use these features for searching, indexing, and browsing of images in a database. This is because representing images in feature space is more efficient in terms of storage and computation than that of pixel space representation. In feature space an image is represented as a vector of features and the dimension of feature vector is less than the original dimension. During the last decade, the advances in information technology made CBIR to have more focus among the researchers. A few examples of such system are QBIC [14], SIMPLICITY [19], and FIRE [21]. Around 50 CBIR systems are surveyed in [22]. The CLUE [23] approach improves user interaction, but the quality of clusters depend on the choice of the partitioning algorithm. The R-tree [26] and mesh-of-trees [27] approaches exploit multidimensional indexing. In [36] color texture features are extracted from images based on vector quantization. This technique for CBIR has far less complexity as compared to using full Discrete Cosine Transform (DCT). Low resolution and strong noise are the two common characteristics in most medical images. With these characteristics, medical images cannot be precisely segmented and extracted for the visual content of their features. In addition, medical images obtained from different scanning devices may display different features, though some approaches to image correction and normalization have been proposed. In [37] the authors disseminate the knowledge of the CBIR approach to the applications of medical image retrieval. There is a strong need to study the semantic gap thoroughly in order to help developing effective solutions. The existence and effects of this gap is investigated in [38].



The approach in [24] combines the Local Binary Pattern (LBP) texture histogram and Moving Picture Experts Group (MPEG-7) edge histogram for image description. But these features alone may not be sufficient for describing all medical images. The color and texture feature scheme [25] extracts the features globally. Medical image retrieval can be improved if more importance is given to local features too. The relevance feedback scheme [39] improves the retrieval accuracy due to the multiple features considered for similarity matching; however it is well suited for natural images rather scanned medical images. This is because medical images have predetermined structures. The structural details are not considered in [39]. These harms are well handled in the proposed scheme using templates of images.

### 3. Proposed Methodology

The technique and methodology behind the proposed CBIR scheme is dealt in detail under this section. Each sub section under this section describes the various modules used in implementing the proposed approach.

#### 3.1. System Overview

This paper proposes an unsupervised novel framework for an efficient content based image retrieval, formalized using the higher level patterns present in the image. The overall methodology is outlined in Figure1.

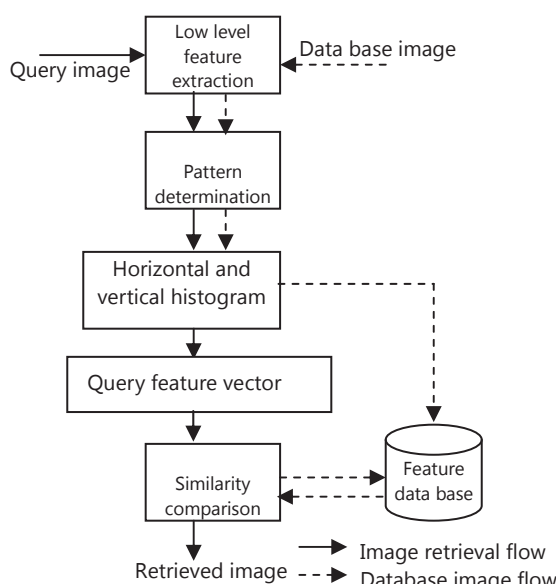


Figure 1. Outline of the proposed CBIR methodology

The performance of a CBIR system depends highly on the particular image representation in the form of a feature vector. The four major tasks involved in the proposed retrieval system are listed out below.

**Step 1:** Extraction of low level features such as color and texture from the database images and the query image.

**Step 2:** Extracting the higher level patterns using the LL band of the wavelet in the first level (64X64).

**Step 3:** Obtaining the horizontal and vertical histograms in both forward and reverse directions.

**Step 4:** Computation of feature similarity between the registered images in the database and the query image.

Steps 1 to 3 are performed for every image when it is registered in the database, whereas steps 1) – 3) including step 4 are performed during the retrieval phase.

#### 3.2. Color Descriptors

Color is one of the important descriptor for image representation in content-based image retrieval, due to the fact that color descriptor is invariant with respect to the common image transformations such as translation, scaling, and rotation. The key items in color feature extraction consist of color space, color quantization, and the kind of similarity measurements. Human vision can be described in various color model forms, e.g. RGB, YIQ, and HSV color models. In the RGB model, images are represented by three components, one for each primary color – red, green and blue. Although human eye is strongly perceptive to red, green, and blue, the RGB representation is not well suited for describing color image from human perception point of view.

Among the different color models, HSV (Hue, Saturation, and Value) is closely related to human visual perception of an image. Hue describes the dimension of color we readily experience when we look at color. Saturation refers to the dominance of hue in the color. How light or dark a color is, is referred to either as a colors' lightness or value. The first, second, and third central moments of each color channel are extracted in the proposed system to represent



the color feature vector of the image in the HSV [12], [28] color space. The color statistic measures namely mean, variance, and skewness for an image of size  $N \times M$  are defined respectively in the following equations.

$$\text{Mean}, \bar{x} = \frac{1}{NM} \sum_{i=1}^N \sum_{j=1}^M x_{ij} \quad (1)$$

$$\text{Variance}, \sigma^2 = \frac{1}{NM} \sum_{i=1}^N \sum_{j=1}^M (x_{ij} - \bar{x})^2 \quad (2)$$

$$\text{Skewness}, \sigma = \frac{\frac{1}{NM} \sum_{i=1}^N \sum_{j=1}^M (x_{ij} - \bar{x})^3}{\left( \frac{1}{NM} \sum_{i=1}^N \sum_{j=1}^M (x_{ij} - \bar{x})^2 \right)^{3/2}} \quad (3)$$

where  $x_{ij}$  is the value of a particular pixel in row  $i$  and column  $j$ .

Above Color moment descriptors are represented by a nine dimensional color feature vector using (1), (2), and (3) for each color channel in H, S, and V. This forms the first 9 features of the feature vector space in the proposed system.

### 3.3. Wavelet Sub band Coefficients

It is a well known fact that wavelet transforms provides a time-frequency representation of signals. It represents both the stationary and transient behavior of the image unlike the Fourier transform which is good only for stationary signals. However multi-resolution representations are very effective for analyzing the information content of images. The fast Haar discrete wavelet [13] transform can be well used for image decomposition. The Haar wavelets are real, orthogonal, and symmetric. Its boundary conditions are the simplest among all wavelet-based methods. Also the high pass and low pass coefficient is simple (either 1 or -1).

One dimensional discrete wavelet transform (1-D DWT) decomposes an input sequence into two components (average component and detail component) by calculations with a low pass filter and a high pass filter. Two dimensional discrete wavelet transform (2-D DWT) decomposes an image into four sub bands [30], one average/approximation component (LL), and three detail components (LH, HL, HH). The image information present in the detail

component sub bands look unobvious (very small coefficients). With Haar DWT, the image information becomes more obvious and the processing time decreases. A typical Fast Haar Transform (FHT) uses  $2^N$  data for calculation in the decomposition process.

Different categories of medical images can be distinguished via homogeneous or texture characteristics. In the proposed system, texture characteristics are extracted from wavelet sub-band coefficients. A higher order feature of entropy is measured for each level of decomposition to form an eight dimensional feature vector.

Phang Chang and Phang Piau have presented the Modified Fast Haar Transform (MFHT) algorithm to reduce the memory requirements of the transform and to limit the amount of inefficient movement of Haar coefficients. This will decrease the overall processing time required for Discrete Wavelet Transform operations. Hence the proposed CBIR scheme uses the MFHT algorithm [30] for image decomposition. The MFHT decomposition algorithm for  $2^N$  data is as follows:

For all the coefficients at level  $N-\theta$ , where  $\theta=1,...,\text{int}(N/2)$ ,

*Approximate coefficients,*

$$\frac{x_{4i} + x_{4i+1} + x_{4i+2} + x_{4i+3}}{4} \quad (4)$$

where  $i = 0,...,1/4(2^N)$

*Detail Coefficients at level  $n-1$ ,*

$$\frac{x_{4i} + x_{4i+1} - x_{4i+2} - x_{4i+3}}{4} \quad (5)$$

where  $i = 0,...,1/4(2^N)$

*Detail Coefficients at level  $n-1$ ,*

$$\frac{x_{2i} - x_{2i+1}}{2} \quad (6)$$

where  $i = 0,...,1/2(2^N)$

Figure 2 shows an example of MFHT decomposition for the set of data given below.

$$F=[4 6 9 7 2 8 9 12 0 8 3 4 5 14 15 6]$$

with  $N = 4$ .



It is clear from Figure 2 that the number of approximate coefficients as well as the number of division operations can be reduced in MFHT since more nodes are considered at one time (for example 4 nodes in Figure 2 instead of the usual 2 nodes in the common FHT).

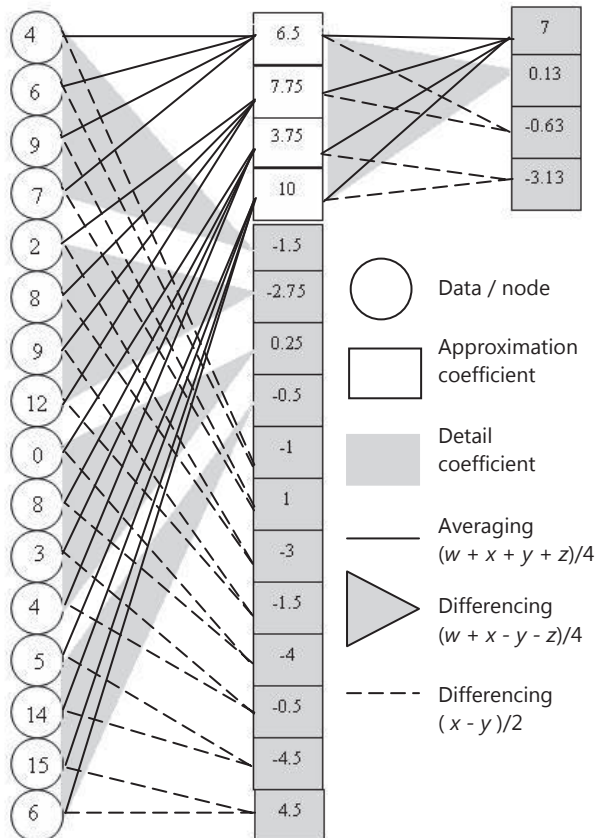


Figure 2: Modified Fast Haar Transform

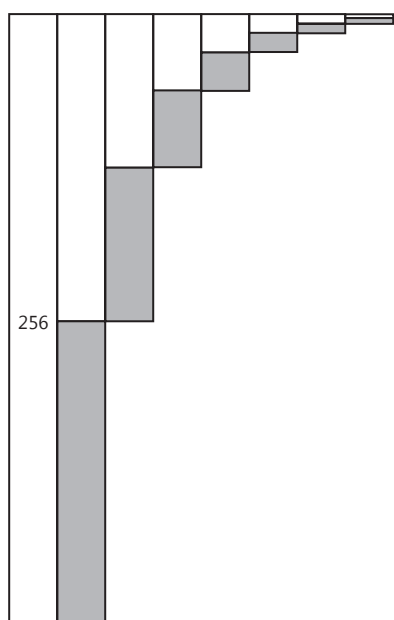


Figure 3: Block diagram of MFHT for 256 data

The coefficients can be ignored to reduce the memory requirements of the transform and the amount of inefficient movement of Haar coefficients. For Modified Fast Haar Transform, this can be done just by calculating  $(w + x + y + z)/4$  instead of  $(x + y)/2$  for approximation, and  $(w + x - y - z)/4$  instead of  $(x - y)/2$  for differencing process. Four nodes have been considered at one time in MFHT. Notice that the calculation for  $(w + x - y - z)/4$  will yield the detail coefficients in the level of  $n-2$  (Figure 2). For the purpose of getting detail coefficients, the differencing process,  $(x - y)/2$  still need to be done. The decomposition step can be done by using matrix formulation as well. Figure 3 roughly gives an idea of the decomposition process using MFHT for  $N = 256$ . If  $2^N$  is divisible by 4, the decomposition steps can be done by applying the MFHT algorithm. If  $2^N$  is divisible by 2 only, the last decomposition step should be done by using the similar way as for standard FHT.

### 3.4. Pattern Extraction

A single point is not indicative of identity, but many points allow for identification. A pattern is an entity, vaguely defined, and that could be given a name. A set of patterns that define a group of sequences having a certain common characteristic is the image signature. A pattern recognition system makes use of the following:

- a sensor that gathers the observations to be classified or described,
- a feature extraction mechanism that computes numeric or symbolic information from the observations, and
- a classification or description scheme that does the actual job of classifying or describing observations relying on the extracted features.

Also pattern recognition may be statistical or syntactic. The proposed scheme for CBIR is based on statistical characterization of patterns, assuming that the patterns are extracted by a probabilistic system. The structural scheme is based on the structural interrelationship of features.



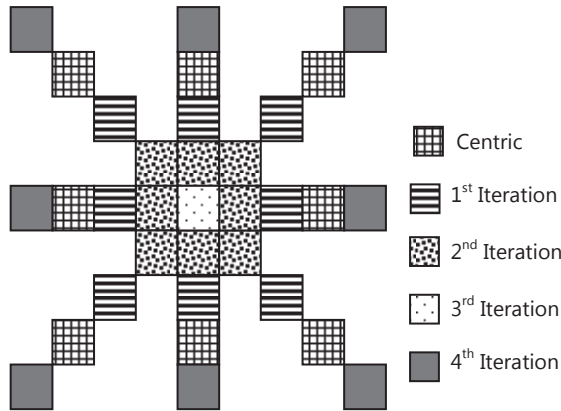


Figure 4: Neighborhood window for first four iterations

Pattern recognition is more complex when templates are used to generate variants. An iterative approach [31] is followed in this paper to identify the statistical characterization of patterns. It detects the dominant points in the digital image based on an initial set of pixel values. The iterative approach adds iteratively significant points by looking for the higher neighborhood pixel values. The modified image from the current iteration and the corresponding changing window are used in the next iteration. The varying window with 8 neighborhoods is illustrated in Figure 4.

A window of  $(2 \times e + 1) \times (2 \times e + 1)$  pixels is used to detect the pattern information, where  $e$  is the iteration number. The pseudo code of the iteration approach used in the implementation for pattern formulation is given below.

$$GM_{itt} = \frac{\sum_{i=0}^{M-1} \sum_{j=0}^{N-1} I_{itt}(i, j)}{M \times N} \quad (7)$$

$$I_{itt} = I_{itt}(i, j) - GM_{itt}, \quad (8)$$

$\forall i \in M$  and  $\forall j \in N$

$$\begin{aligned} LM_{itt} = & [I_{itt}(i - itt, j - itt) + \\ & I_{itt}(i, j - itt) + \\ & I_{itt}(i + itt, j - itt) + \\ & I_{itt}(i - itt, j) + I_{itt}(i + itt, j) + \\ & I_{itt}(i - itt, j + itt) + I_{itt}(i, j + itt) + \\ & I_{itt}(i + itt, j + itt)] / 8.0 \end{aligned} \quad (9)$$

where  $itt$  is the iteration number, and  $i$  and  $j$  values vary from 0 to  $M-1$  and 0 to  $N-1$  respectively.

$$I_{itt}(i, j) = LM_{itt} \quad (10)$$

The above mentioned iteration process proceeds as follows:

- Initially the original image is considered for iteration.
- The global mean of the image pixel values is determined using (7).
- The calculated global mean is subtracted from each pixel values using (8).
- The local mean of the image pixel values is computed using a changing window of  $(2 \times e + 1) \times (2 \times e + 1)$  pixels using (9).
- The local mean of the pixel values of the image is maintained as in (10) and  $I_{itt}(i, j)$  from (10) is used for the next iteration.

The iteration process is performed four times to get the higher level pattern image in the proposed system.

### 3.5. Histogram

In general the histogram of an image shows the frequency of occurrence of each grey scale value (pixel value). Histogram is invariant to translation and rotation of the image and change only slowly under change of angle view. The proposed scheme uses the optimum edge histogram of the query image to determine whether the image is oriented in forward or backward direction. The edge information contained in the images is generated and processed by using Canny edge detection algorithm [32]. The Binary Image (BI) is used here since they are the simplest to process. Histogram of an image in the horizontal and vertical direction is defined by a vector as given below.

$$H_{horz}(i) = \sum_{i=0}^{M-1} BI(i, j) \quad (11)$$

$; 0 \leq j \leq M - 1$

$$H_{vert}(i) = \sum_{j=0}^{N-1} BI(i, j) \quad (12)$$

$; 0 \leq i \leq N - 1$

The sample histogram obtained from (11) and (12) is depicted in Figure 5.



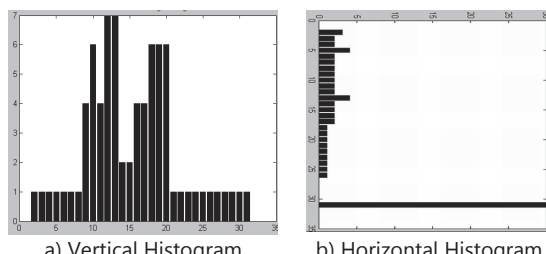


Figure 5: Sample Histogram

For database images the horizontal-forward and vertical-forward direction edge-histograms are calculated. For Query image the horizontal-forward, horizontal-reverse, vertical-forward and vertical-reverse direction edge histograms are generated. Then the optimum of horizontal or vertical forward and reverse histogram of the query that has best match with the database image histogram is treated as the histogram reference feature to provide directionally invariant retrieval performance.

### 3.6. Retrieval

The feature vector for every query image is formulated as described in subsection 3.2. to 3.5. under section 3. The optimum matching of database-horizontal-forward-histogram with that of the query-horizontal-forward and query-horizontal-reverse-histogram is found, and that optimum (query-horizontal-forward-histogram or query-horizontal-reverse-histogram) is selected for retrieval process for the case of horizontal histogram matching. The same is performed for vertical-edge-histogram also. The similarity matching between the query and database images is done by determining the distance between feature vectors in the feature database, and the query feature vector. The distance between a query image  $I_q$  and an image in the database  $I_i$  in the visual feature space is defined by the Sum of Squared Distance (SSD) as given below:

$$d^V(I_q, I_i) = \sum_{j=1}^{FC} |f_{q,j}^V - f_{i,j}^V|^2 \quad (13)$$

In (13), Feature Count ( $FC$ ) denotes the total number of features detected from each image,  $f^V$  is the feature vector, and  $i$  is the image index that varies from 1 to the size of image database. The retrieval precision may not be stable for all

classes of images, as a combined feature set involves in the retrieval process. To let each component of feature vector get equal importance in retrieval process the extracted feature values needs to be normalized. In the proposed system normalization is done over the distance values rather assigning weights to individual feature component. The similarity values for every feature representation are different, and hence that values can be of different orders of magnitude. To ensure that one similarity value does not overshadow the other in the overall similarity process, normalization is done on the distance value as given below:

$$d^V(I_q, I_i) = \frac{d^V(I_q, I_i)}{\max[d^V(I_q, I_i)]} \times 10^6 \quad (14)$$

Equation (14) formulates the final distance vector  $d^V$ , after normalization. This vector shows the distance between the reference query image  $I_q$  and each of the images in the database  $I_i$  with respect to the feature component. It is used in image retrieval process as a similarity measure. This distance vector is used as the similarity measure during image retrieval process.

## 4. Experimental Evaluation

The implementation details of the proposed CBIR scheme, results obtained, and the performance evaluation details are dealt under this section. The proposed CBIR scheme could retrieve both color images and gray scale images with equally high retrieval accuracy in reduced cost.

### 4.1. Implementation and Results

The proposed CBIR system has been implemented in MATLAB, under Windows XP and tested extensively with medical image database containing different classes of images. The core of the evaluation procedure is the image collection. This collection should be as open as possible so as to be distributed, modified and completed freely. Around 1000 scanned medical images - anatomy of human organs, brain, intestine, lungs, kidney, and uterus are included in the dataset for the image database in the proposed system. All the images



are of size 128x128 pixels. For every image in the database a total of 1105 features have been obtained by the proposed system which includes 9 HSV features, 8 entropy intensities, 1024 (32\*32) pattern features, and 64 edge histogram features. The same 1105 features are extracted from the query image also. The proposed system concentrates much on pattern feature since medical images generally have their own standard structure. Similarity matching and retrieval are done using (13) and (14). Extensive testing have been done over the image data set, and it could be proved that any normal user will be fully satisfied with the proposed system, due to its desirable and improved results. The proposed system exhibits higher retrieval performance with respect to medical images rather natural images as medical images have a predetermined structure. Figure 6 shows the snapshot of the image retrieval. It shows the query image with its final pattern obtained and the ranked ordered top 10 retrieved images for three sample queries. As expected, the first retrieved image in all cases is the query image. For each query image at most 99.8% and at least 80% relevant images are retrieved by inspecting the database.

#### 4.2. Performance Evaluation

Evaluation of retrieval performance is a crucial problem in CBIR. The current status of performance evaluation in CBIR is far from that of Information Retrieval (IR). The ultimate aim of evaluating CBIR systems is to measure how useful they are to their users. For achieving this aim, it is therefore important to have a precise specification of the requirements of a given CBIR system. However, such a specification is very much dependent of the type of application that is envisaged. The aspect of retrieval performance of the proposed system has been evaluated in terms retrieval time cost and retrieval accuracy. Table 1 shows the retrieval time cost comparison of the proposed system with the authors' another CBIR scheme [33], for two different data sets of two classes of images. From Table1, it is found that the average retrieval time cost is approximately the same irrespective of the image classes in the proposed scheme. It is also seen that the average retrieval time is very less, compared to the average time required in Back Propagation Network (BPN)

method [33] of author, for image retrieval. This is presented by the graph in Figure 7.

The retrieval accuracy of the proposed system is evaluated in terms of precision and recall parameters [34]. Precision and recall are the standard measures in information retrieval, which give a good indication of system performance. Either value alone contains insufficient information. The precision versus recall performance is compared with few other retrieval methods. Precision is the proportion of relevant images retrieved (similar to the query image) with respect to the total retrieved (15), whereas recall is the proportion of relevant images retrieved with respect to the relevant images that exist in the database (16).

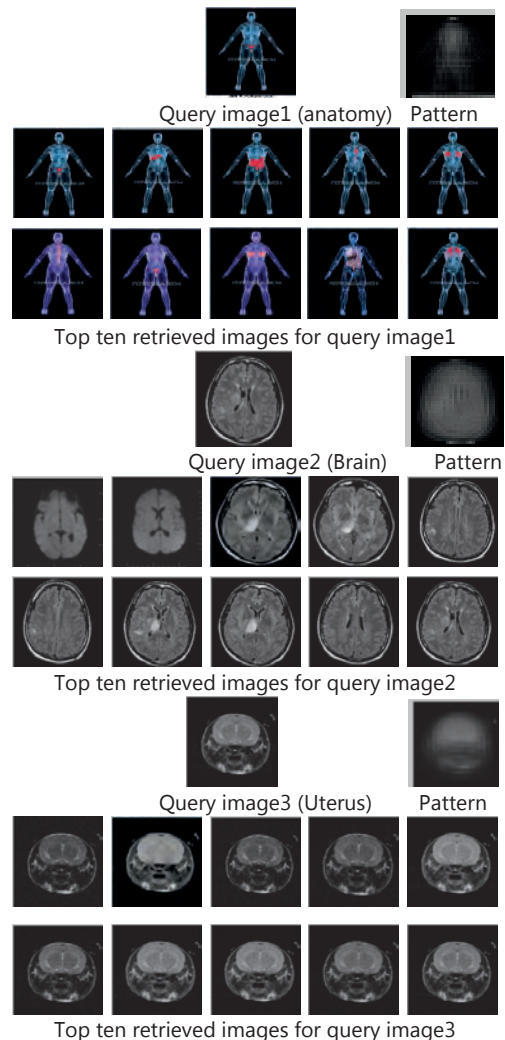


Figure 6: Snapshot of the image retrieval



TABLE 1: TIME COST (milliseconds)

Image	Datasets	Time (proposed)	Time (BPN)	Time Avg. (proposed)	Time Avg. (BPN)
Anatomy	30	6.92	10.52	8.43	11.64
Anatomy	60	9.94	12.75		
Lungs	30	6.94	11.12	8.11	12.05
Lungs	60	9.23	12.98		

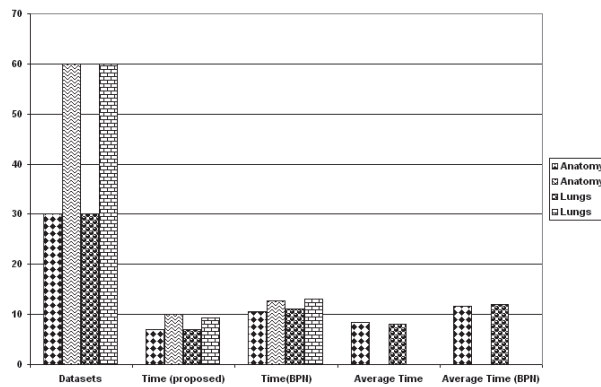


Figure 7: Time cost comparison

$$\text{Precision} = \frac{I_r}{I_r + I_n} \quad (15)$$

$$\text{Recall} = \frac{I_r}{I_r + N_r} \quad (16)$$

where  $I_r$  is the number of relevant images retrieved,  $I_n$  is the number of non-relevant images retrieved, and  $N_r$  is the number of relevant images not retrieved. For a given query  $I_r + I_n$  is the total number of images retrieved, and  $I_r + N_r$  is the total number of relevant images in the database. Hence a precision versus recall graph actually shows the precision percentage at each instance for every single retrieved image. Generally precision and recall should be either used together or the number of images retrieved should be specified in order to point out the change of precision with respect to recall. In most typical systems, the precision drops as recall increases, hence in order for an image retrieval system to be considered effective the precision values must be higher than the same recall ones, which is mostly the case in the current system. The precision and the corresponding recall percentage obtained for four different classes of images with two images from each class in the database used in the

proposed system is shown in Table 2. The precision versus recall performance for a few queries performed is depicted in Figure 8. The image thumbnails in Figure 6 reveal this precision vs. recall performance. The average precision and recall values obtained in the proposed system from Table 2 are 96.68% and 28.99% respectively.

In experimentation, the performance was evaluated on more than 50 randomly selected queries. The comparison between the proposed method and frequency layer [35] method in terms of precision is given in Table 3. The proposed system shows 10-20% of improvement in retrieval accuracy. This improvement is due to the importance given to the pattern present in the images rather the global features alone.

The performance comparison graph in Figure 9 shows that the proposed scheme substantially outperforms the traditional CBIR schemes for medical application

TABLE 2: PRECISION AND RECALL VALUES

Image	Precision	Recall
Anatomy 1	86.70%	13.54%
Anatomy 2	100%	15.63%
Brain 1	100%	44.12%
Brain 2	100%	44.12%
Lungs 1	100%	14.56%
Lungs 2	100%	14.56%
Uterus 1	100%	75%
Uterus 2	86.70%	65%

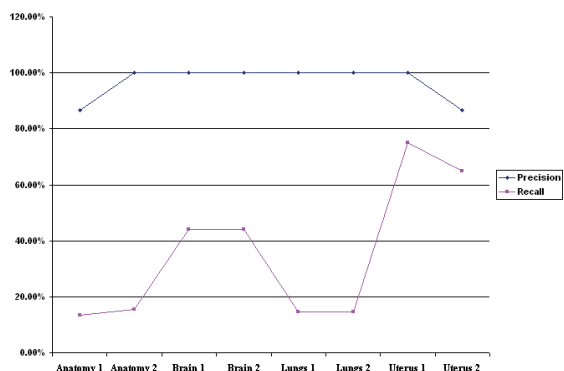


Figure 8: Precision of the proposed system



TABLE 3: COMPARISON OF PRECISION VALUES

Image	Frequency Layer	Proposed
Anatomy	65.4%	86.70%
Brain	77.8%	100%
Lungs	75.8%	100%
Uterus	69.5%	86.70%

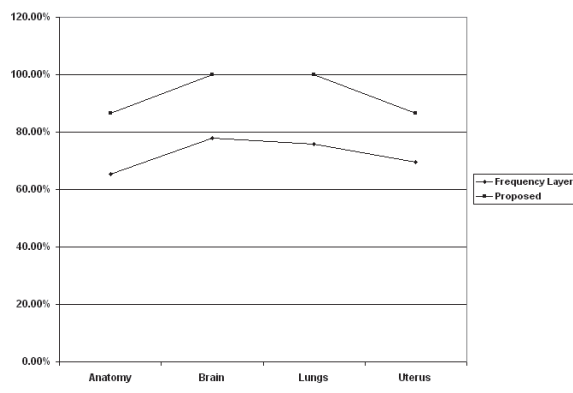


Figure 9: Performance comparison

## 5. Conclusion

In this paper, a new framework for CBIR is presented, which integrates the higher level patterns present in the image, together with the color and texture features. The optimum of horizontal or vertical forward and reverse histogram of the query that have a best match with database image histogram is treated as another reference feature to provide directionally invariant retrieval performance. Experimental results have shown that the proposed framework is cost effective, robust, and it improves the retrieval performance significantly in terms of precision and recall. Fuzzy-logic based or neural network based learning may improve the retrieval performance further, but probably with increased complexity with respect to time and cost. However, these factors will be considered in the future work.

## 6. References

- [1] A.W.M. Smeulders, M. worring, S. Santini, A. Gupta, and R. Jain, "Content-based image retrieval at the end of the early years", IEEE Trans. Pattern Analysis and Machine Intelligence, vol. 22, no. 12, pp. 1349-1380, Dec. 2000.
- [2] S. K. Chang and A. Hsu, "Image information systems: Where do we go from here?" IEEE Transactions on Knowledge Data Engineering. vol. 4, no. 5, pp. 431-442, Oct. 1992.
- [3] I. J. Cox, T. P. Minka, T. V. Papathomas, and P. N. Yianilos, "The Bayesian image retrieval system, PicHunter: Theory, implementation, and psychophysical experiments", IEEE Trans. Image Processing, vol. 9, no. 1, pp. 20-37, Jan. 2000.
- [4] P. Enser. "Visual Image Retrieval: Seeking the Alliance of Concept-based and Content-based Paradigms", Journal of Information Science, vol. 26, no. 4, pp. 199-210, August 2000.
- [5] V. N. Gudivada, and V. V. Raghavan. "Modeling and Retrieving Images by Content", International Journal of Information Processing and Management, vol. 33, no. 4, pp. 427-452, 1997.
- [6] Jing Huang, S. Ravi Kumar, Mandar Mitra, Wei-Jing Zhu, and Ramin Zabih, "Image indexing using color correlograms", Proceedings of IEEE Conference on Computer Vision and Pattern Recognition, San Juan, PR, pp. 762-768, June 1997.
- [7] H. Abrishami-Moghadam, T. Taghizadeh Khajoie, A. H. Rouhi, and M. Saadatmand-T, "Wavelet Correlogram: a new approach for image indexing and retrieval", Journal Elsevier, Pattern Recognition, vol. 38, pp. 2506-2518, 2005.
- [8] Th. Gevers, in: M. Lew (Ed.), "color based image retrieval", Multimedia search, Springer, Berlin 2001.
- [9] L. Balmelli, A. Mojsilovic, "Wavelet domain features for texture description, classification, and replicability analysis", Wavelets in Signal and Image Analysis: From Theory to Practice" (edited book), Kluwer Academic publishers, Neteherland, 2001.
- [10] E. J. Stollnitz, T. D. DeRose, and D. H. Salesin, "Wavelets for Computer Graphics: Theory and Applications", Morgan Kaufman Publishers, 1996.
- [11] J. Z. Wang, G. Wiederhold, O. Firschein, and S. X. Wei, "Content based Imgae Indexing and searching using Daubechies' wavelet",



- Int. journal on Digital Libraries, vol. 1, no. 4, pp 311-328, 1998.
- [12] Daniela Stan Raicu, "Tutorial 2: Image feature extraction", Visual Computing Workshop: Image Processing, DePaul University, pp. 01-12, May 21<sup>st</sup> 2004.
- [13] Piotr Porwik, and Agnieszka Lisowska "The Haar-Wavelet Transform in Digital Image Processing: Its Status and Achievements", Machine Graphics & Vision, vol. 13, no. ½, pp. 79-98, 2004.
- [14] Y. Rui, T. S. Huang, M. Ortega, and S. Mehrotra, "Relevance feedback: A power tool for interactive content-based image retrieval", IEEE Transactions on Circuits and Systems for Video Technology, vol. 8, no. 5, pp. 644 – 655, Sept. 1998.
- [15] C. Faloutsos, R. Barber, M. Flickner, J. Hafner, W. Niblack, D. Petkovic, and W. Equitz, "Efficient and effective querying by image content", J. Intell. Info. Syst., vol. 3, no. 3-4, pp. 231-262, 1994.
- [16] J. R. Smith, and S. F. Chang, "VisualSEEK: a fully automated content based query system", in proc. of 4<sup>th</sup> ACM Int. Conf. Multimedia, pp. 87-98, 1997.
- [17] R. W. Picard and T. P. Minka, "Vision texture for annotation", Journal on Multimedia Systems, vol. 3, no. 1, pp. 3-14, 1995.
- [18] Y. Chen, and J. Z. Wang, "A region –based fuzzy feature matching approach to content-based image retrieval", IEEE Trans. Pattern Anal. Mach. Intell. vol. 24, no. 9, pp. 1252-1267, Sep. 2002.
- [19] J. Z. Wang, J. Li, And G. Wiederhold, "SIMPLICITY: semantics-sensitive integrated matching for picture libraries", IEEE Trans. on Pattern Anal. Mach. Intell. vol. 23, no. 9, pp. 947-963, Sep. 2001.
- [20] C. Schmid and R. Mohr, "Local gray value invariants for image retrieval", IEEE Trans. Pattern Anal. Mach. Intell. vol. 19, no. 5, pp. 530-535, May 1997.
- [21] T. Deselaers, D. Keysers, and H. Ney, "FIRE – Flexible image retrieval engine: ImageCLEF 2004 evaluation", in Lecture notes in Computer Science, vol. 3491, pp. 688-698, 2004.
- [22] R. Veltcamp and M. Tanase, "Content-based image retrieval systems: a survey", Dept. Comp. Sci., Utrecht Univ. Tech. Rep. UU-CS-2000-34, 2000.
- [23] Yixin Chen, James Z. Wang, and Robert Krovetz, "CLUE: Cluster-based retrieval of images by unsupervised learning", IEEE Trans. On Image Processing, vol. 14, no. 8, pp. 1187-1201, Aug. 2005.
- [24] Guangjian Tian, Hong Fu, and David Dagan Feng, "Automatic medical image categorization and annotation using LBP and MPEG-7 edge histograms", Proc. of the 5<sup>th</sup> Int. Conf. on Info. Technology and application in Biomedicine, pp. 51-53, May 2008.
- [25] Subrahmanyam Murala, Anil Balaji Gonde, and R. P. Maheswari, "Color and Texture Features for Image Indexing and Retrieval", IEEE Int. Conf. on Adv. Computing – IACC'09, pp. 1411–1416, March 2009.
- [26] E. G. M. Petrakis, and C. Faloutsos, "Similarity searching in medical image databases", IEEE Trans. on Knowl. Data Engg., vol. 9, no. 3, pp. 435 – 447, May/June 1997.
- [27] W. M Jeng, and J. H. Hsiao, "An efficient content based image retrieval system using the mesh-of-trees architecture", Journal of Inf. Sci. Engg., vol. 21, pp. 797-808, 2005.
- [28] Asadollah Shahbahrami, Demid Borodin, and Ben Juurlink, "Comparison between color and texture features for image retrieval", Delft University of Technology, The Netherlands, pp. 361-371.
- [29] Mausumi Acharyya and Malay K. Kundu, "Document image Segmentation using wavelet scale-space features", IEEE Trans. on Ckts. and Syst. for Video Technology, vol. 12, no. 12, pp 1117-1127, Dec' 2002.
- [30] Phang Chang, and Phang Piau, "Modified Fast and Exact Algorithm for fast Haar transform", Int. J. of Comp. Sci. and Engg. vol. 2, no. 2, pp. 55–58, 2008.
- [31] Stefan Schulte et. al., "Fuzzy two-step filter for impulse noise reduction from color images", IEEE Trans. Image Processing, vol. 15, no. 11, Nov' 2006.
- [32] J. Canny, "A computational approach to edge detection", IEEE Trans. on Pattern Anal. and Mach. Intell., vol. 8, no. 6, pp. 679-698, Nov'1986.
- [33] K. P. Ajitha Gladis, and K. Ramar, "A novel method for content based image retrieval using the approximation of statistical features, morphological features, and BPN



- network", ICCIMA'07, vol. 3, pp. 179-184, Dec'2007.
- [34] Karen Sparck Jones, "Information retrieval experiment", Butterworth-Heinemann Newton Publisher, MA, USA, 1981.
- [35] Jianhua Wu, Xiaoman Wang, Donghui Yan, Chaorong Wei, Yixiang Zhang, "Method for medical image retrieval based on frequency layer feature", Int. conf. on Information Technology and Computer Science, IEEE Computer Society, pp. 622-624, 2009.
- [36] H.B.Kekre, Tanuja K. Sarode, Sudeep D. Thepade, " Image Retrieval using Color-Texture Features from DCT on VQ Codevectors obtained by Kekre's Fast Codebook Generation", ICGST- Int. Journal on Graphics, Vision and Image Processing, vol. 9, no. 5, Sept' 2009.
- [37] Preeti Aggarwal, H.K. Sardana, Gagandeep Jindal, "Content Based Medical Image Retrieval: Theory, Gaps and Future Directions", ICGST- Int. Journal on Graphics Vision and Image Processing, vol. 9, no. 11, Apr' 2009.
- [38] Omar Karam, Ahmad Hamad, Mahmoud Attia, "Exploring the Semantic Gap in Content-Based Image Retrieval: with application to Lung CT", ICGST- Graphics Vision and Image Processing Conference (GVIP 05 Conference), pp. 19-21, Dec' 2005.
- [39] K. P. Ajitha Gladis, K. Ramar, Jestin Rajamony, "Multiple feature set relevance feedback scheme for content-based image retrieval", Int. Journal of Image Processing & Networking Techniques", vol. 3, no. 1, pp. 33-43, June 2010.

## Biographies



K.P Ajitha Gladis is a Ph.D. research scholar, currently pursuing Ph.D. in Computer Science and Engineering. Now she is working as the Assistant Professor in CSI Institute of Technology, Thovalai. Her areas of interest are image processing and pattern recognition.



Dr. K.Ramar is a Ph.D. holder in Computer Science and Engineering. Now he is the Principal in Sri Vidhya College of Engineering and Technology, Virudhunagar. He has organized many workshops and faculty development programs for the technocrats. He has published many papers and has guided many research scholars. His areas of interest are image processing, pattern recognition, and Computer vision and machine intelligence.



Jestin Rajamony is a Ph.D. research scholar, currently pursuing Ph.D. in Computer Science and Engineering. Now he is working as the Assistant Professor in CSI Institute of Technology, Thovalai. His areas of interest are image processing, control systems, and real time systems.





## Creating and Manipulating Surfaces through Physics-based Curve Deformations

L. H. You<sup>1</sup>, B. P. Tang<sup>2</sup>, X. Y. You<sup>3</sup>, and J. J. Zhang<sup>1</sup>

<sup>1</sup>National Centre for Computer Animation, Bournemouth University, Poole, BH12 5BB, UK

<sup>2</sup>College of Mechanical Engineering, Chongqing University, Chongqing City, China

<sup>3</sup>Faculty of Engineering and Computing, Coventry University, Coventry, CV1 5FB, UK

### Abstract

In this paper, we present a new method to improve the efficiency of physics-based surface modeling which creates and manipulates surfaces through physics-based curve deformations. The proposed physics-based mathematical model of curve deformations consists of a vector-valued fourth order ordinary differential equation and boundary constraints. An efficient finite difference solution for curve modeling (FDSCM) is developed to solve the mathematical model. The computational efficiency and accuracy from FDSCM are compared to those from the finite difference solution for surface modeling (FDSSM). It is found that FDSCM is more efficient and accurate than FDSSM. The effects of the vector-valued shape control parameters and sculpting forces in the ordinary differential equation together with the boundary tangents in the boundary constraints on curve deformations are investigated. Their strong influences indicate that they are useful shape manipulation tools. With our proposed physics-based curve deformations, we create various geometric models by sweeping a deformed curve or using 2D cross-section curves or 3D feature curves, and manipulate surface shapes by deforming these curves.

**Keywords:** Surface creation, Surface manipulation, Physics-based curve deformations, Ordinary differential equations, Efficient finite difference solution.

### 1. Introduction

Modeling of curves and surfaces is very important in computer graphics and computer aided design

etc. Existing shape modeling techniques for curves and surfaces can be classified as purely and non-purely geometric methods.

Traditional curve and surface representation methods such as Bézier, B-spline and NURBS (Farin, 1997) are the most popular purely geometric techniques. They were investigated by a lot of researchers such as Hu and Wang (2007) and Yoshida and Saito (2007).

NURBS curves and surfaces are defined by control points, weights and knot sequences. The variation of these parameters results in the shape change of the curves and surfaces. Therefore, much work was concentrated on the modification of these parameters (Till, 1992; Au and Yuen, 1995).

In addition to purely geometric modeling, physics-based modeling methods have been receiving more and more attention in recent years since they can create more realistic appearances. Terzopoulos and Fleischer (1988) employed viscoelasticity, plasticity and fracture to model the shape of deformable bodies. Celniker and Gossard (1991) proposed deformable curve and surface finite-elements for free-form shape design. Applying Lagrangian mechanics of an elastic surface and the finite element method, Terzopoulos and Qin (1994) developed dynamic NURBS. Considering symmetries and topological variability of some objects, Qin, and Terzopoulos (1995) proposed dynamic NURBS swung surfaces. Léon and Veron (1997) used the mechanics of bar network to deform multi-patch tensor based free-form surfaces. Cotin et al. (2000) examined three physical models for real-time cutting,



deformations and force feedback in surgery simulation. Based on inter-atomic interaction, Jansson and Vergeest (2002) presented a discrete mechanics model of deformable bodies which incorporates motion, collision and deformation, etc. They (2003) also described an interface between a deformable-body mechanics model and a rigid-body mechanics model and applied it in design engineering, geometric modeling and computer animation. Using Lagrangian work-energy equation, Xie and Qin (2002) presented a framework of physics-based subdivision surface design. Based on a finite difference formulation and approximate classical continuum models, Etzmuss et al. (2003) established a link between mass-spring particle systems and classical mathematical elasticity for animation of deformable objects. Choi et al. (2004) presented a mass-spring-based model which treats deformation as a result of force propagation among the mass points in localized regions. Using modal derivatives and an interactive sketching technique to generate low-dimensional subspace bases, Barbić and James (2005) presented an approach for fast subspace integration of reduced-coordinate models for objects with complex geometry, large deformation and linear materials. Müller et al. (2005) introduced a meshless deformation to perform dynamic simulation which deals with point-based objects without any connectivity information. Extending traditional linear modal analysis to track the rotational component of an infinitesimal deformation, Choi and Ko (2005) proposed a real-time simulation technique for large deformations described with Green's nonlinear strains. By drawing an analogy between autowaves and elastic deformation, Zhong et al. (2006) investigated a new methodology for deformable object simulation which can deal with large-range deformations and accommodate isotropic, anisotropic and inhomogeneous material properties. Nealen et al. (2006) reviewed various physically based techniques of deformable models such as finite element/difference/volume methods, mass-spring systems, mesh-free methods, coupled particle systems and reduced deformable models based on modal analysis. Swanson et al. (2009) developed a physics-based modeling approach which is used to create high quality surfaces for application in computer aided geometric design.

Modeling techniques developed from partial differential equations (PDE) are becoming more

active. Rather than manipulating the control points, they modify the surface shape by adjusting the shape control parameters, sculpting forces, and positional and tangential boundary conditions.

PDE-based geometric modeling was firstly applied in surface blending (Bloor and Wilson, 1989) and free-form surface generation (Bloor and Wilson, 1990). Recently, Monterde and Ugail (2004) investigated harmonic and biharmonic Bézier surfaces. Since the resolution of the fourth order PDE is the key to successful applications of PDE surfaces, some numerical methods were developed (Brown et al., 1998).

As the shape control parameters have a strong influence on the generated surface shape, a new and more general fourth order PDE has been introduced for the generation of blending surfaces (You et al., 2004a). A sixth order PDE was also presented for surface modeling (Zhang and You, 2004) and blending (You et al., 2004b) with curvature continuity.

Unlike the above methods that are only applicable to static surface modeling, Du and Qin (2000) extended PDE based approaches to dynamic modeling by putting together a fourth order PDE and a motion equation. Du and Qin (2005) also proposed a method which uses geometric and physical constraints to design PDE based surfaces.

Physics-based and PDE-based modeling methods are usually solved by numerical methods. These numerical methods require an expensive computation procedure which hinders wide applications of these methods in computer graphics and computer-aided design etc.

Surfaces can be generated from many characteristic curves. This idea was proposed by Singh and Fiume (1998). They used wire curves to describe the shape of an object, and introduced the domain curves to define the domain of deformation on the object. Pyun et al. (2004) applied wire curves in facial animation. Qin and Wright (2006) investigated how to construct freeform surfaces from unorganized curves. Khan and Okuda (2006) investigated reconstruction of curves and 3D mesh models from points. Nealen et al. (2007) presented a method to design freeform surfaces from 3D curves. You et al. (2008) examined dynamic skin deformations by using characteristic curves. Liu et al. (2008) discussed how to use nonparallel curve networks to construct surfaces. Gal et al. (2009) used intelligent wires as basic primitives to edit surface



models.

Motivated by the existing work on physics and curve based surface modeling approaches, in this paper we will develop a new method to create and manipulate surfaces. Compared to the curve based surface modeling approaches, it extends purely geometric curve deformations to physics-based curve deformations. Compared with the physics-based and PDE-based surface modeling approaches, it is more efficient.

The existing work on curve based surface modeling has indicated that the shape of a surface can be well described by the curves on the surface. If physical properties and sculpting forces of a surface can be properly transformed into those of the curves describing the surface which we will investigate in our another paper, surface creation and manipulation by using physics-based curve deformations can improve the realism of purely geometric surface modeling and greatly raise the efficiency of physics-based surface modeling. This is due to the introduction of physics of curve deformations and the fact that surface creation and manipulation using physics-based curve deformations transforms a 2D surface modeling into a 1D curve modeling leading to high modeling efficiency. In addition to the above advantages, the proposed approach can use fewer data to define a surface.

In order to develop such an approach, we will propose an efficient finite difference solution for curve modeling (FDSCM) derived from our proposed vector-valued fourth order ordinary differential equation (ODE), compare it to the finite difference solution for surface modeling (FDSSM) which is derived from a vector-valued fourth order partial differential equation, investigate the effects of shape control parameters, sculpting forces and boundary tangents, examine local deformations and curve modeling, and demonstrate the applications of our proposed approach in surface modeling.

The remaining part of the paper is organized as follows. The mathematical model and corresponding finite difference solution are presented in Section 2. Computational efficiency and accuracy are examined in Section 3. Properties of curve deformations and curve modeling are discussed in Section 4. Curve based surface modeling is investigated in Section 5, and Section 6 concludes the paper.

## 2. Mathematical Model and Finite Difference Technique

In order to develop physics-based curve deformations, we first investigate the mathematical model which is used to physically deform curves. The deformation of a curve with physical properties is similar to that of a beam. Using the same methodology deriving the governing equation of the beam bending, the deformation of a curve can be described with the following vector-valued fourth order ordinary differential equation whose derivation is given in Appendix A.

$$\mathbf{S}_1 \frac{d^4 \mathbf{X}(u)}{du^4} + \mathbf{S}_2 \frac{d^2 \mathbf{X}(u)}{du^2} = \mathbf{F}(u) \quad (1)$$

where  $u$  is a parametric variable,  $\mathbf{X}(u)$  represents a vector-valued position function of a 3D curve which has three components  $x$ ,  $y$ , and  $z$ ,  $\mathbf{S}_1$  and  $\mathbf{S}_2$  are vector-valued shape control parameters, and  $\mathbf{F}(u)$  is a vector-valued function describing sculpting forces.

The solution to Eq. (1) presents a series of 3D curves. After specifying the positional and tangential constraints, we can obtain the curve which satisfies these boundary constraints formulated below

$$\begin{aligned} u=0 \quad \mathbf{X}=\mathbf{a} \quad \frac{\partial \mathbf{X}}{\partial u}=\mathbf{b} \\ u=1 \quad \mathbf{X}=\mathbf{c} \quad \frac{\partial \mathbf{X}}{\partial u}=\mathbf{d} \end{aligned} \quad (2)$$

where  $\mathbf{a}$  and  $\mathbf{c}$  indicate boundary points, and  $\mathbf{b}$  and  $\mathbf{d}$  stand for boundary tangents of a 3D curve at the boundary points.

In general, the vector-valued function of sculpting forces in Eq. (1) can be of any forms. For these situations, the analytical solution of Eq. (1) subjected to (2) may not exist or is very difficult to obtain. Therefore, numerical methods have to be used. The finite difference method is a numerical method which approximates derivatives with finite difference quotients and transforms a PDE or ODE into a set of linear algebraic equations. There are three finite difference schemes: central, forward and backward. Using the nodes shown in Fig. 1, the central finite difference formulae of the first, second and the fourth derivatives at the node  $j$  can be written as

$$\begin{aligned} (\frac{d\mathbf{X}}{du})_j &= (\mathbf{X}_{j+1} - \mathbf{X}_{j-1})/(2\Delta u) \\ (\frac{d^2\mathbf{X}}{du^2})_j &= (\mathbf{X}_{j+1} + \mathbf{X}_{j-1} - 2\mathbf{X}_j)/\Delta u^2 \\ (\frac{d^4\mathbf{X}}{du^4})_j &= [6\mathbf{X}_j - 4(\mathbf{X}_{j-1} + \mathbf{X}_{j+1}) + (\mathbf{X}_{j-2} + \mathbf{X}_{j+2})]/\Delta u^4 \end{aligned} \quad (3)$$

Substituting Eq. (3) into ordinary differential equation (1), Eq. (1) is transformed into a number of linear algebraic equations



$$(6\mathbf{S}_1 - 2\Delta u^2 \mathbf{S}_2) \mathbf{X}_j + (\Delta u^2 \mathbf{S}_2 - 4\mathbf{S}_1) (\mathbf{X}_{j-1} + \mathbf{X}_{j+1}) + \mathbf{S}_1 (\mathbf{X}_{j-2} + \mathbf{X}_{j+2}) = \Delta u^4 \mathbf{F}_j \quad (4)$$

(j = 2,3,4,...,N-1)

Since the coordinate values of boundary nodes 1 and N are known according to Eq. (2), we are only required to write the finite difference equation for nodes 2, 3, 4, ... and N-1. For the finite difference equation at node 2 and N-1, boundary nodes 1 and N together with nodes 0 and N+1 beyond the boundary nodes are involved. They can be determined by the finite difference equations of boundary constraints (2), i.e.,

$$\begin{aligned} \mathbf{X}_1 &= \mathbf{a} \\ \mathbf{X}_2 - \mathbf{X}_0 &= 2\Delta u \mathbf{b} \\ \mathbf{X}_N &= \mathbf{c} \\ \mathbf{X}_{N+1} - \mathbf{X}_{N-1} &= 2\Delta u \mathbf{d} \end{aligned} \quad (5)$$

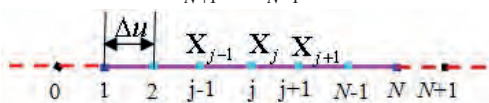


Figure 1. Nodes of finite difference algorithm

Equations (4) and 5 give N+2 linear algebraic equations which can be used to determine N+2 unknown constants  $\mathbf{X}_j$  ( $j = 0, 1, 2, \dots, N, N+1$ ).

Writing Eqs. (4) and (5) in a matrix form, we obtain

$$\mathbf{A}\mathbf{X} = \mathbf{D} \quad (6)$$

Equation (6) can be solved using the algorithms and corresponding programs provided by Press et al. (1992). The obtained result is called the finite difference solution for curve modeling (FDSCM).

The solution to a partial differential equation subject to boundary constraints represents a 3D surface. In order to make a comparison between surface modeling based on ODE and that based on PDE, we also introduce the finite difference solution of PDE.

For surface modeling tasks, fourth order partial differential equations are widely applied. Here we adopt the following vector-valued equation which was derived in Appendix B with the same methodology as that of an elastic thin plate under bending deformations

$$\mathbf{S}_1 \frac{\partial^4 \mathbf{X}(u,v)}{\partial u^4} + \mathbf{S}_2 \frac{\partial^4 \mathbf{X}(u,v)}{\partial u^2 \partial v^2} + \mathbf{S}_3 \frac{\partial^4 \mathbf{X}(u,v)}{\partial v^4} = \mathbf{F}(u,v) \quad (7)$$

where  $u$  and  $v$  are parametric variables,  $\mathbf{X}(u,v)$  represents a vector-valued position function of a 3D surface which has three components  $x$ ,  $y$ , and  $z$ ,  $\mathbf{S}_1$ ,  $\mathbf{S}_2$  and  $\mathbf{S}_3$  are vector-valued shape

control parameters, and  $\mathbf{F}(u,v)$  is a vector-valued function describing sculpting forces.

The boundary constraints of surface modeling tasks can be written as

$$\begin{aligned} u = 0 \quad \mathbf{X} = \mathbf{a}(v) \quad \frac{\partial \mathbf{X}}{\partial u} &= \mathbf{b}(v) \\ u = 1 \quad \mathbf{X} = \mathbf{c}(v) \quad \frac{\partial \mathbf{X}}{\partial u} &= \mathbf{d}(v) \end{aligned} \quad (8)$$

where  $\mathbf{a}(v)$  and  $\mathbf{c}(v)$  indicate boundary curves, and  $\mathbf{b}(v)$  and  $\mathbf{d}(v)$  stand for boundary tangents of a 3D surface at the boundary curves.

Using the same central finite difference algorithm, the finite difference solution for surface modeling (FDSSM) can be developed from PDE (7) and boundary constraints (8), and written in the same matrix form (6).

Although the matrix form of the finite difference equation (6) is the same for FDSCM and FDSSM, the implication is different. FDSSM deals with a two-dimensional problem with two parametric variables  $u$  and  $v$  whose resolution region is a surface area. In contrast, FDSCM copes with a one-dimensional problem with one parametric variable  $u$  whose resolution region is a line segment.

FDSCM can be directly applied to curve modeling. For surface modeling, the surface to be modeled should be transformed into a series of curves. Then FDSCM is applied to generate or deform these curves and the surface is created or manipulated from these deformed curves.

As demonstrated in next section, FDSCM is more efficient and accurate than FDSSM.

### 3. Computational Efficiency and Accuracy

Since the closed form solution of PDE (7) subject to boundary constraints (8) is accurate and most efficient, we will make a comparison among the closed form solution, FDSCM and FDSSM. The computational accuracy will be evaluated with the following error equation.

$$E = \frac{1}{I_u \times J_v} \sum_{i=1}^{I_u} \sum_{j=1}^{J_v} \left\{ \left[ [x(u_i, v_j) - \bar{x}(u_i, v_j)]^2 + [y(u_i, v_j) - \bar{y}(u_i, v_j)]^2 + [z(u_i, v_j) - \bar{z}(u_i, v_j)]^2 \right] \right\}^{1/2} / \left[ [x(u_i, v_j)]^2 + [y(u_i, v_j)]^2 + [z(u_i, v_j)]^2 \right]^{1/2} \quad (9)$$

where  $I_u$  and  $J_v$  are chosen points respectively in  $u$  and  $v$  directions within the resolution region of a surface,  $x$ ,  $y$ , and  $z$  components without a “-” stand for the closed form solution and those



with a “-” for FDSCM and FDSSM.

The surface to be generated satisfies the following boundary constraints

$$\begin{aligned} u=0 \quad & x = e_1 \sinh(e_2 v + e_3) + (1+u_0^3) \sin e_4 v \\ & y = e_5 \cosh e_6 v + (1+u_0^3) \cos e_4 v \\ & z = h_0 + e^{u_0} \quad \frac{\partial x}{\partial u} = 3u_0^2 \sin e_4 v \\ & \frac{\partial y}{\partial u} = 3u_0^2 \cos e_4 v \quad \frac{\partial z}{\partial u} = e^{u_0} \quad (10) \\ u=1 \quad & x = e_7 u_1 \sin e_4 v \quad y = e_7 u_1 \cos e_4 v \\ & z = h_1 \quad \frac{\partial x}{\partial u} = e_7 \sin e_4 v \\ & \frac{\partial y}{\partial u} = e_7 \cos e_4 v \quad \frac{\partial z}{\partial u} = 0 \end{aligned}$$

and the three components of a sculpting force take the form of

$$\begin{aligned} f_x &= [p_0 + p_1 u(1-u)] \sin e_4 v \\ f_y &= [p_0 + p_1 u(1-u)] \cos e_4 v \quad (11) \\ f_z &= 0 \end{aligned}$$

In the above equations,  $e_1$  to  $e_7$ ,  $h_0$ ,  $h_1$ ,  $u_0$ ,  $u_1$ ,  $p_0$  and  $p_1$  are known constants, and  $f_x$ ,  $f_y$  and  $f_z$  are the three components of a sculpting force. Using the boundary constraints (10) and the sculpting force (11), we can obtain the closed form solution of PDE (7). Without considering the sculpting force, i.e. setting  $p_0$  and  $p_1$  in the closed form solution to zero, we generated the surface shown in Fig. 2a. By applying a sculpting force ( $p_0 = 1,500$  and  $p_1 = 1,000$ ), the surface in Fig. 2a was deformed into that in Fig. 2b. The shape of the surface was noticeably changed after the application of the sculpting force. It indicates that the sculpting force can be used as a sculpting tool. We timed the process of determining the unknown constants in the closed form solution and found it took less than  $10^{-6}$  of a second on an ordinary PC.

For FDSSM, all the boundary constraints were taken from the closed form solution. The resolution region was divided into  $15 \times 15$  nodes and  $25 \times 25$  nodes, respectively. The generated surface for  $15 \times 15$  nodes was depicted in Fig. 2c and that for  $25 \times 25$  nodes was shown in Fig. 2e. The time used to obtain these node values and the errors compared to the closed form solution using equation (9) were given in Table 1.

For FDSCM, we must divide the surface into a number of curves. For each curve, it is divided into a series of nodes and solved with FDSCM. In order to facilitate the comparison with FDSSM, we took 15 curves for the first case and 25 curves for the second case. For each curve, 15 nodes for the

first case and 25 nodes for the second case were uniformly collocated.

Here, we adopted two algorithms of FDSCM: the accurate FDSCM which produces the same coordinate values as those of the closed form solution at the collocated nodes, and the approximate FDSCM which minimizes the error of node coordinate values between the finite difference and closed form solutions.

For the accurate FDSCM, the following constraint equation

$$\mathbf{X} = \mathbf{X}_i \quad (i=1, 2, \dots, K) \quad (12)$$

was used to determine the unknown sculpting forces at all the inner nodes of a curve.

In equation (12),  $K$  represents the total number of inner nodes on a curve and  $\mathbf{X}_i$  stands for the  $i^{th}$  node of the surface to be created.

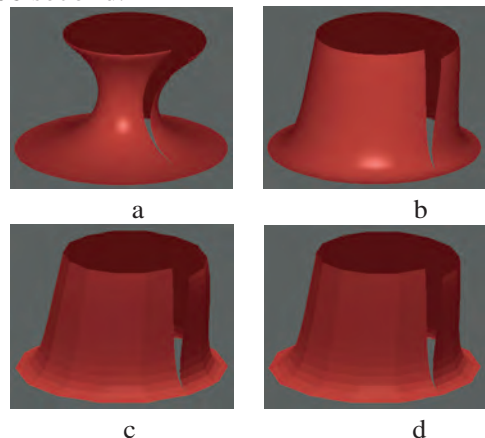
In the interest of space, the surface generated by the accurate FDSCM was not depicted in Fig. 2. However, the computing time and accuracy were given in Table 1 where NC stands for node collocation, and CM for the computational methods.

For the approximate FDSCM, the equation

$$\sum_{i=1}^K \|\mathbf{X} - \mathbf{X}_i\|^2 \rightarrow \min \quad (13)$$

is solved by the least squares technique (You et al. 2000).

For the  $15 \times 15$  node case, 4 unknown sculpting forces were applied at the inner nodes 4, 7, 10 and 12 of each curve. The created surface was given in Fig. 2d, and the time and error were listed in Table 1. Since the unknown constants are reduced from 13 of the accurate FDSCM to 4 of the approximate FDSCM, the corresponding computational time is reduced from 0.14 second to 0.06 second.



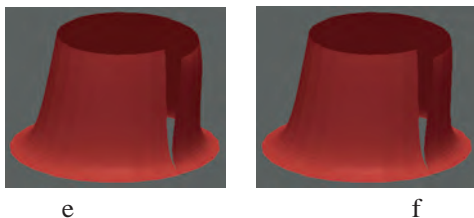


Figure 2. Surfaces generated with different methods and meshes

For the  $25 \times 25$  node case, 7 unknown sculpting forces were applied at the inner nodes 4, 7, 10, 12, 15, 18 and 21 of each curve. The obtained surface was shown in Fig. 2f, and the time and error were listed in Table 1. The computational time is reduced from 0.93 second to 0.35 second.

Table 1. Computational errors and time

NC	$15 \times 15$		$25 \times 25$	
CM	Error	T(s)	Error	T(s)
FDSSM	0.3593	10.78	0.3555	255
accurate FDSCM	0	0.14	0	0.93
approximate FDSCM	0.3552	0.06	0.3543	0.35

The comparison given by Table 1 suggests that FDSCM is more accurate and faster than FDSSM. The finite element method and other numerical methods require almost the same amount of computation as FDSSM. Computation cost is therefore not ideal for such numerical methods if they are to be used in interactive or real-time shape modeling applications.

#### 4. Properties of Curve Deformations and Curve Modeling

In this section, we discuss the properties of curve deformations and curve modeling with the above developed method. In particular, we investigate the effects of boundary tangents, shape control parameters and sculpting forces, how to achieve local deformation, and how to conduct curve modeling.

##### 4.1. Effect of Boundary Tangents

A straight line shown in Fig. 3 is deformed under different boundary tangents. The line was divided into 100 uniform intervals with 101 nodes (It should be pointed out that much fewer nodes can be used to obtain the same deformations. Here taking 101 nodes is for the illustrative purpose only). At nodes 25, 51 and 76, the sculpting forces with  $x$  component  $f_{x25} = 200$ ,  $f_{x51} = -200$ ,  $f_{x76} = 200$  and zeroed  $y$  and  $z$  components were applied. The values of the vector-valued shape control parameters at all the nodes were set to 1.

When we took  $\mathbf{b} = \mathbf{d} = 0$ , i.e. no rotation at its two end points, we obtained the shape of the second curve from the left. This shape was changed to the third when taking  $\mathbf{b} = \mathbf{d} = 0.8$ . The symmetric rotation can be obtained by taking  $\mathbf{b} = -0.5$  and  $\mathbf{d} = 0.5$  which resulted in the fourth curve. When these two parameters were taken to be  $\mathbf{b} = -0.5$  and  $\mathbf{d} = -0.5$ , the fifth curve was produced.

The images in Fig. 3 indicate that by changing both the direction and size of boundary tangents, different shapes of a curve can be easily obtained.

##### 4.2. Effect of Shape Control Parameters

In order to study the effect of the vector-valued shape control parameters in equation (1) on the deformation of the curve, we kept the boundary tangents  $b_y = b_z = d_y = d_z = 0$ ,  $b_x = -2$  and  $d_x = 2$  unchanged. When taking the shape control parameter values of all the nodes to be 1 and applying a sculpting force with  $x$  component  $f_{x51} = 120$  at node 51, a straight line in the leftmost of Fig. 4 is changed into the shape of the second curve from the left. Setting all the shape control parameter values to 0.6, we obtained the third curve. If the shape control parameter values are changed to 1.2, the shape of the curve is illustrated by the fourth curve. Keeping all the shape control parameters to be 1.2 and taking  $S_1$  between nodes 10 and 30 to be 0.0001, the shape on the rightmost is achieved.

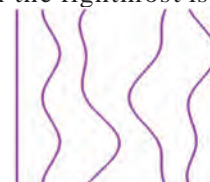


Figure 3. Influence of boundary tangents



Figure 4. Influence of shape control parameters

Examining these images, we can conclude that the shape control parameters function as the stiffness of the curve which are also an effective shape controller.

##### 4.3. Effect of Sculpting Forces

Applying different sculpting forces on the curve, we can obtain different shapes of a curve. This effect was illustrated in Fig. 5. For all the deformed curves in the figure, the constraints and shape control parameter were the same, that is, boundary tangents were set to  $b_x = -0.5$ ,  $d_x = 0.5$  and  $b_y = b_z = d_y = d_z = 0$ , and the shape control parameters at all the nodes were taken to be 1. When sculpting forces with  $x$  component



$f_{x25} = 120$ ,  $f_{x51} = -70$  and  $f_{x76} = 120$  were applied at nodes 25, 51 and 76, the curve was deformed from a straight line on the leftmost of Fig. 5 to the second from the left. Changing these sculpting forces to  $f_{x25} = 10$ ,  $f_{x51} = -50$  and  $f_{x76} = 100$ , the third curve was obtained. Further changing these sculpting forces to  $f_{x25} = 20$ ,  $f_{x51} = 50$  and  $f_{x76} = 20$  led to the generation of the fourth curve. Finally, setting these sculpting forces to  $f_{x25} = -60$ ,  $f_{x51} = 80$  and  $f_{x76} = -60$ , the shape on the rightmost was created.

The powerful influence of sculpting forces on the shape of curves is well demonstrated by these images. Since achieving deformations through sculpting forces is more intuitive than other factors affecting shape changes of curves, sculpting forces are a very useful tool for shape manipulation.

#### 4.4. Local Deformation

Since curve deformations are one-dimensional and its two boundaries are the two end points of the resolution region on the curve, the boundaries can be very easily treated when using the finite difference method. It is hence especially suitable for description of local deformation. In contrast, the resolution region of FDSSM is a surface area. Therefore, using FDSSM to deform a local area is more difficult than using FDSCM.



Figure 5. Influence of sculpting forces

Figure 6. Local deformation of curves

In Fig. 6, a curve on the leftmost has 101 nodes. Firstly, choosing the segment between node 21 and node 81 as a local deformation region, setting the boundary tangent at its two ends to zero and all the shape control parameters to 1, and applying a sculpting force  $f_{x51} = -1,000$ , we obtained the local deformation shape within this region as shown in the second from the left. Since the relative rotations at the two ends are constrained to zero, smooth transitions are achieved at the two ends. Reducing the deformation region to nodes 31 and 71, and changing the sculpting force to  $f_{x51} = 4,000$ , we obtained the third from the left. Finally, we further reduced the deformation region to that from node 41 to node 61, changed the sculpting force to  $f_{x51} = -10000$  and set boundary tangent at the

two ends of the new deformation region to  $-10$  and  $10$ , the local deformation within this new region was obtained as shown at the rightmost. For this case, since the relative rotations were permitted, acute angles at the two ends occur. This property is very useful. It indicates that by changing the boundary tangents at the two ends, not only different shapes of the curve can be created, but also various transitions and some special effects such as cuspidal points can be achieved.

#### 4.5. Curve Modeling

The basic process for curve modeling is: choosing a simple curve or a straight line or their assembly as the initial shape of a complicated curve, which roughly resembles the final shape; interactively applying forces to deform the initial shape globally; and finally determining the local deformation regions and deforming the surface to reach the final shape. Two examples are given below to demonstrate the proposed method.

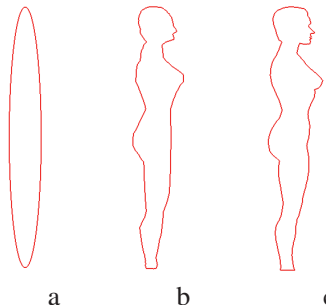


Figure 7. Curve modeling of a woman profile

The first example is to model a woman profile. We chose an ellipse as its initial shape as shown in Fig. 7a. We interactively applied sculpting forces to the ellipse and deformed it to the shape in Fig. 7b which has a rough shape of the woman profile. Finally, we chose the regions of eyes, nose, mouth and neck etc. as local deformation regions and applied different sculpting forces to obtain the final deformed shape of the ellipse as given in Fig. 7c.

The second example is to model a teapot. In this example, the assembly of some straight lines is used to represent the initial shape of the teapot. We used a big rectangle to approximate the main body of the teapot and two small concentric rectangles to represent its handle, as shown in Fig. 8a. With the bottom edge of the teapot being fixed, by applying forces on the main body and handle respectively, and making the joint points between the main body and handle share the same displacements, we obtained a global approximation of the teapot. Subsequently, some



local regions were determined, and local boundary constraints and sculpting forces were applied to obtain its final deformed shape, as shown in Fig. 8b.

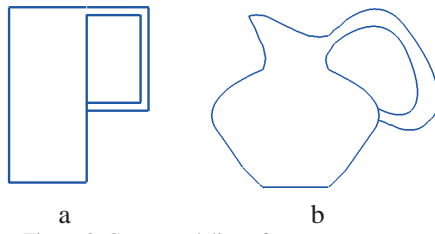


Figure 8. Curve modeling of a teapot

## 5. Curve based surface modeling

In this section, we investigate surface creation and manipulation through physics-based curve deformations developed above.

### 5.1. Surface Creation

With the developed FDSCM, we can perform surface creation. Two types of surfaces will be given to introduce different surface creation techniques. The first is a family of symmetric surfaces which are created by sweeping a profile curve. The second are arbitrary space surfaces which are generated by deforming 2D cross-section or 3D feature curves.

In the nature world and engineering, especially in manufacturing engineering, many objects exhibit symmetry. Examples include vases, wineglasses, bowls, dishes, and shafts used as mechanical components. This type of surfaces can be generated by sweeping a curve, most often a 2D cross-sectional contour along a 3D trajectory. Three types of sweeps, transitional, rotational and general sweeps, can be applied to obtain desired surfaces. In the following, we give a design example of a lamp which is generated by rotational sweeping about a straight line.

The contour curve of the lamp is two-dimensional. We chose an inclined straight line shown in Fig. 9a as its initial shape of the contour curve with its two end points being exactly at the final positions of the lamp.

Then, the initial curve was globally deformed under sculpting forces and a rough shape was obtained. Followed by local deformations, the final shape of the contour curve of the lamp was achieved which was given in Fig. 9b. By sweeping this contour curve about the symmetric axis of the lamp, we generated its final surface shape as shown in Figure 9c.

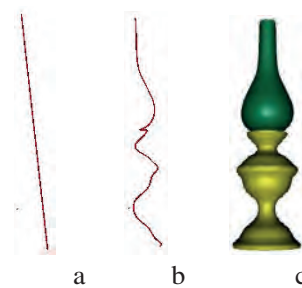


Figure 9. Surface creation of a lamp

Now let us study the shape modeling of an arbitrary 3D surface. There are two types of modeling techniques. One is to slice a 3D surface into a number of cross-section curves. By doing so, the 3D surface is transformed into a series of 2D curves. The other is to use some 3D feature curves to define the shape of the surface. Then, we interactively deform these 2D cross-section or 3D feature curves into their final shapes.

A human face is a very typical example of arbitrary surfaces. Here we use 2D cross-section curves to create the human face. In the following subsection, we will employ 3D feature curves to manipulate a horse torso.

Firstly, half of an ellipsoid was taken to be the rough shape of a human face. Then it was sliced into a number of 2D cross-section curves. For this example, 59 curves were used. By applying global and local deformation techniques, these curves were deformed to the final shapes of the human face as shown in Fig. 10a. The images in Figs. 10b and 10c were obtained from the final deformed curves in Fig. 10a.

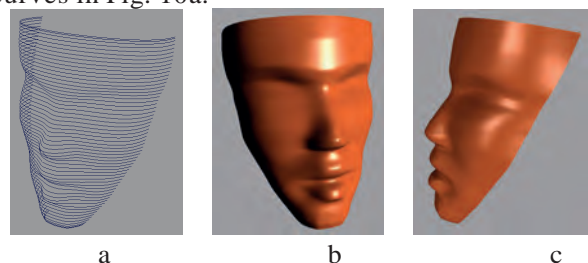


Figure 10. Surface creation of a human face

### 5.2. Surface Manipulation

Our proposed approach is effective and efficient in surface manipulation. For doing this, some feature curves within the region of the geometric model to be manipulated are specified. Then, the shapes of these curves are changed with our proposed approach. The surface shape is achieved through these curves.

Here we discuss how to manipulate the torso shape of a horse model in Fig. 11a. First, nine 3D feature curves are specified on the torso of the horse model as indicated in Fig. 11b. Then, we



apply sculpting forces to deform these curves into new shapes depicted in Fig. 11c. Finally, a new torso shape in Fig. 11d is generated from these deformed curves.

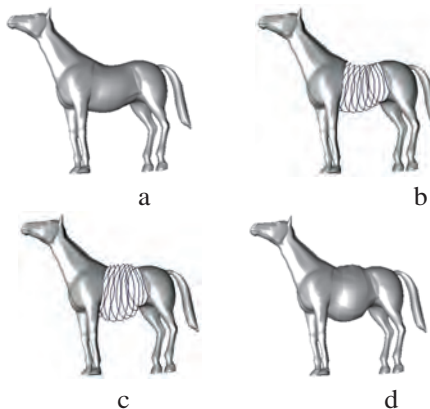


Figure 11. Manipulation of torso shape of a horse model

## 6. Conclusions

A simple and efficient method has been developed in this paper to create and manipulate surfaces through physics-based curve deformations.

The computational efficiency and accuracy between FDSCM and FDSSM have been compared. FDSCM is faster and more accurate than FDSSM. Its high efficiency suggests that FDSCM is very useful for the development of an interactive user interface of surface modeling. The properties of physics-based curve deformations have been investigated. The shape control parameters, sculpting forces and boundary tangents have very strong influences on curve shape, and can be used as effective user interface controls. We also demonstrated how to achieve local deformations and carry out curve modeling. Based on our proposed physics-based curve deformations, we presented a new approach to create and manipulate surfaces which builds a 3D surface model by sweeping a curve or using a set of 2D cross-section or 3D feature curves, and manipulates a surface by physically deforming these curves.

Compared to existing modeling techniques based on the manipulation of control points or surface points, the developed method is simple, easy to use and powerful because it can deform curves and surfaces by changing the shape control parameters, sculpting forces and boundary tangents instead of moving a large number of control or surface points. Due to the introduction of physics of curve deformations, it can improve the realism of purely geometric surface modeling approaches including those based on purely geometric curve deformations. Compared to the existing physics-

based and PDE-based surface modeling approaches using numerical methods such as the finite element method and finite difference method, the developed method transforms a two-dimensional modeling problem into a one-dimensional one and simplifies the resolution process. It is therefore more efficient. As its boundary constraints only involve two boundary points which are easier to process than those of a surface area. Hence it is more flexible than surface based methods and especially suitable for modeling of locally complex shapes.

## 7. Acknowledgements

This research is in part supported by EPSRC grant EP/F030355/1. Some mesh data used in this project was made available by ‘500 3D-Objects’ (<http://www.taschen.com>) and Robert Sumner and Jovan Popović from the Computer Graphics Group at MIT.

## 8. References

- [1] C. K. Au, and M. M. Yuen. Unified approach to NURBS curve shape modification. *Computer-Aided Design*, 27(2): 85-93, 1995.
- [2] J. Barbič, and D. L. James. Deformable models: Real-time subspace integration for St. Venant-Kirchhoff deformable models. *SIGGRAPH 05* and *ACM Transactions on Graphics*, 24(3): 982-990, 2005.
- [3] M. I. G. Bloor, and M. J. Wilson. Generating blend surfaces using partial differential equations. *Computer-Aided Design*, 21(3): 165-171, 1989.
- [4] M. I. G. Bloor, and M. J. Wilson. Using partial differential equations to generate free-form surfaces. *Computer-Aided Design*, 22(4): 202-212, 1990.
- [5] J. M. Brown, M. I. G. Bloor, M. S. Bloor, and M. J. Wilson. The accuracy of B-spline finite element approximations to PDE surfaces. *Computer Methods in Applied Mechanics and Engineering*, 158: 221-234, 1998.
- [6] G. Celniker, and D. Gossard. Deformable curve and surface finite-elements for free-form shape design. *Computer Graphics*, 25(4): 257-266, 1991.
- [7] K.-S. Choi, H. Sun, P.-A. Heng, and J. Zou. Deformable simulation using force propagation model with finite element optimization. *Computers and Graphics*, 28(4): 559-568, 2004.
- [8] M. G. Choi, and H.-S. Ko. Modal warping: Real-time simulation of large rotational deformation and manipulation. *IEEE Transactions on*



- Visualization and Computer Graphics, 11(1): 91-101, 2005.
- [9] S. Cotin, H. Delingette, and N. Ayache. A hybrid elastic model for real-time cutting, deformations, and force feedback for surgery training and simulation. *The Visual Computer*, 16: 437-452, 2000.
- [10] H. Du, and H. Qin. Direct manipulation and interactive sculpting of PDE surfaces. *Computer Graphics Forum (EUROGRAPHICS 2000)*, 19(3): 261-270, 2000.
- [11] H. Du, and H. Qin. Dynamic PDE-based surface design using geometric and physical constraints. *Graphical Models*, 67: 43-71, 2005.
- [12] O. Etzmuss, J. Gross, and W. Strasser. Deriving a particle system from continuum mechanics for the animation of deformable objects. *IEEE Transactions on Visualization and Computer Graphics*, 9(4): 538-550, 2003.
- [13] G. Farin. *Curves and Surfaces for Computer Aided Geometric Design: A Practical Guide* (4th Edition). Academic Press, 1997.
- [14] R. Gal, O. Sorkine, N. J. Mitra, D. Cohen-Or. iWIRES: An Analyze-and-Edit Approach to Shape Manipulation. *SIGGRAPH 09 and ACM Transactions on Graphics*, 28(3): #33, 1-10, 2009.
- [15] Q.-Q. Hu, and G.-J. Wang. Improved bounds on partial derivatives of rational triangular Bezier surfaces. *Computer-Aided Design*, 39(12): 1113-1119, 2007.
- [16] J. Jansson, and J. S. M. Vergeest. A discrete mechanics model for deformable bodies. *Computer-Aided Design*, 34(12): 913-928, 2002.
- [17] J. Jansson, and J. S. M. Vergeest. Combining deformable- and rigid-body mechanics simulation. *The Visual Computer*, 19(5): 280-290, 2003.
- [18] I. R. Khan, and M. Okuda. Construction of regular 3D mesh models for real objects. *GVIP Journal*, 6(3): 23-31, 2006.
- [19] J. C. Léon, and P. Veron. Semiglobal deformation and correction of free-form surfaces using a mechanical alternative. *The Visual Computer*, 13: 109-126, 1997.
- [20] L. Liu, C. Bajaj, J. O. Deasy, D. A. Low and T. Ju. Surface Reconstruction From Non-parallel Curve Networks. *Computer Graphics Forum (EUROGRAPHICS 2008)*, 27(2): 155-163, 2008.
- [21] J. Monterde, and H. Ugail. On harmonic and biharmonic Bézier surfaces. *Computer Aided Geometric Design*, 21: 697-715, 2004.
- [22] M. Müller, B. Heidelberger, M. Teschner, and M. Gross. Meshless deformations based on shape matching. *SIGGRAPH 05 and ACM Transactions on Computer Graphics*, 24(3): 471 - 478, 2005.
- [23] A. Nealen, M. Müller, R. Keiser, E. Boxerman, and M. Carlson. Physically based deformable models in computer graphics. *Computer Graphics Forum*, 25(4): 809-836, 2006.
- [24] A. Nealen, T. Igarashi, O. Sorkine, and M. Alexa. FiberMesh: Designing freeform surfaces with 3D curves. *SIGGRAPH 07 and ACM Transactions on Graphics*, 26(3): #41, 1-9, 2007.
- [25] W. H. Press, S. A. Teukolsky, W. T. Vetterling, and B. P. Flannery. *Numerical Recipes in C: The Art of Scientific Computing* (Second Edition). Cambridge University Press, 1992.
- [26] H. Pyun, H. J. Shin and S. Y. Shin. On extracting the wire curves from multiple face models for facial animation. *Computers & Graphics*, 28: 757-765, 2004.
- [27] H. Qin, and D. Terzopoulos. Dynamic NURBS swung surfaces for physics-based shape design. *Computer Aided Design*, 27: 111-127, 1995.
- [28] S. Qin and D. K. Wright. Progressive surface modelling scheme from unorganised curves. *Computer-Aided Design*, 38: 1113-1122, 2006.
- [29] K. W. Swanson, K. A. Brakke, D. E. Breen. Physics-based Surface Modeling using Quasi-Static Liquids. *Computer-Aided Design and Applications*, 6(1-4): 1-11, 2009.
- [30] K. Singh, and E. Fiume. Wires: a geometric deformation technique. *SIGGRAPH'98*, 405-414, 1998.
- [31] D. Terzopoulos, and K., Fleischer. Modeling inelastic deformation: viscoelasticity, plasticity, fracture. *SIGGRAPH 88 and Computer Graphics*, 22(4): 269-278, 1988.
- [32] D. Terzopoulos, and H. Qin. Dynamic NURBS with geometric constraints for interactive sculpting. *ACM Transactions on Graphics*, 13(2): 103-136, 1994.
- [33] W. Till. Knot-removal algorithms for NURBS curves and surfaces. *Computer-Aided Design*, 24(8): 445-453, 1992.
- [34] H. Xie, and H. Qin. A Physics-based Framework for Subdivision Surface Design with Automatic Rules Control. In Proceedings of the 10th Pacific Conference on Computer Graphics and Applications, pp. 304-315, 2004.
- [35] N. Yoshida, and T. Saito. Quasi-aesthetic curves in rational cubic Bézier forms. *Computer-Aided Design and Applications*, 4(1-6): 477-486, 2007.
- [36] L. H. You, J. J. Zhang, and P. Comninou. A solid volumetric model of muscle deformation for computer animation using the weighted



- residual method. Computer Methods in Applied Mechanics and Engineering, 190: 853-863, 2000.
- [37] L. H. You, J. J. Zhang, and P. Comninou. Blending surface generation using a fast and accurate analytical solution of a fourth order PDE with three shape control parameters. The Visual Computer, 20: 199-214, 2004a.
- [38] L. H. You, P. Comninou, and J. J. Zhang. PDE blending surfaces with  $C^2$  continuity. Computers & Graphics, 28: 895-906, 2004b.
- [39] L. H. You, X. S. Yang, and J. J. Zhang. Dynamic skin deformation with characteristic curves. Computer Animation and Virtual Worlds, 19(3-4): 433-444, 2008.
- [40] J. J. Zhang, and L. H. You. Fast surface modeling using a 6<sup>th</sup> order PDE. Computer Graphics Forum (EUROGRAPHICS 2004), 23(3): 311-320, 2004.
- [41] Y. Zhong, B. Shirinzadeh, G. Alici, and J. Smith. An autowave based methodology for deformable object simulation. Computer-Aided Design, 38(7): 740-754, 2006.

## Appendix A: Derivation of Ordinary Differential Equation for Physics-Based Curve Deformations

An arbitrary curve in a three-dimensional space has  $x$ ,  $y$  and  $z$  components. Each of them is a function of parametric variable  $u$ . If a vector-valued ordinary differential equation is used to represent a curve, all three components can be determined by the solution of the ODE. Here we take the  $x$  component as an example to derive the ordinary differential equation for physics-based curve deformations.

The parametric variables  $u$  and position function  $x$  form a two-dimensional space, and the set of their coordinate values produces a curve in this two-dimensional space. Considering an infinitesimal element  $du$  taken from the curve under deformation, the external and internal forces are shown in the following figure where  $F_x$  is an externally applied sculpting force,  $Q$  is a shear force,  $N$  is an axial force, and  $M$  is a bending moment.

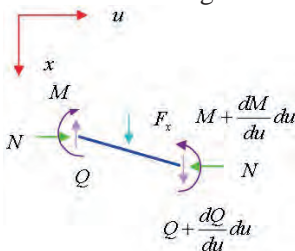


Figure A1. The forces and moments acting on an infinitesimal element of a curve

The equilibrium condition of forces in the  $x$  direction gives the following equation

$$\frac{dQ}{du} = -F_x \quad (A1)$$

Taking moment equilibrium about the right end point of the infinitesimal element, we obtain

$$N \frac{dx}{du} + Q - \frac{dM}{du} = 0 \quad (A2)$$

The above equation (A2) can be further changed into the following form

$$N \frac{d^2x}{du^2} + \frac{dQ}{du} - \frac{d^2M}{du^2} = 0 \quad (A3)$$

According to the beam theory in textbooks of mechanics of materials, the following relationship holds between the moment  $M$  and position function  $x$

$$M = -EI \frac{d^2x}{du^2} \quad (A4)$$

where  $E$  and  $I$  are Young's modulus and area moment of inertia of the curve, respectively.

Substituting (A1) and (A4) into (A3), and denoting

$$\begin{aligned} S_{1x} &= EI \\ S_{2x} &= N \end{aligned} \quad (A5)$$

we obtain the fourth order ordinary differential equation for  $x$  component

$$S_{1x} \frac{d^4x}{du^4} + S_{2x} \frac{d^2x}{du^2} = F_x \quad (A6)$$

Using the same method, we can derive the fourth order ordinary differential equations for  $y$  and  $z$  components. The vector-valued form of these three equations gives the vector-valued fourth order ordinary differential equation (1).

## Appendix B: Derivation of Partial Differential Equation for Physics-Based Surface Modeling

Similarly, any surfaces in a three-dimensional space are composed of  $x$ ,  $y$  and  $z$  components. Each such component is a function of parametric variables  $u$  and  $v$ , and can be described with the solution of a vector-valued fourth order partial differential equation.

Taking  $x$  component as an example and considering an infinitesimal element of  $du \times dv$  taken from a surface under bending deformation, the external and internal forces are indicated in the following figure where  $F_x$  is an externally applied sculpting force,  $Q_u$  and  $Q_v$  are the shear forces,  $M_u$  and  $M_v$  are the bending moments, and  $M_{uv} = M_{vu}$  is the twisting moment.

Taking the equilibrium of moments around  $u$  and  $v$  axes, we obtain

$$\begin{aligned} Q_u &= \frac{\partial M_u}{\partial u} + \frac{\partial M_{vu}}{\partial v} \\ Q_v &= \frac{\partial M_v}{\partial v} + \frac{\partial M_{uv}}{\partial u} \end{aligned} \quad (B1)$$



The condition of force equilibrium along x-axis gives the following equation

$$\frac{\partial Q_u}{\partial u} + \frac{\partial Q_v}{\partial v} + F_x = 0 \quad (\text{B2})$$

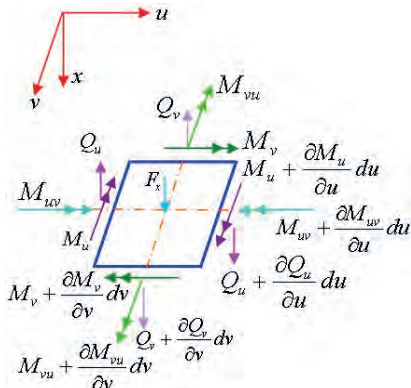


Figure B1. The forces and moments acting on an infinitesimal element of a surface

Substituting equation (B1) into (B2), one obtains the equilibrium equation below

$$\frac{\partial^2 M_u}{\partial u^2} + 2 \frac{\partial^2 M_{uv}}{\partial u \partial v} + \frac{\partial^2 M_v}{\partial v^2} + F_x = 0 \quad (\text{B3})$$

It can be found from the textbooks of elasticity that the bending moments, twisting moment and position function  $x$  hold the following relations for a surface with an isotropic elastic property

$$\begin{aligned} M_u &= -D \left( \frac{\partial^2 x}{\partial u^2} + \mu \frac{\partial^2 x}{\partial v^2} \right) \\ M_v &= -D \left( \frac{\partial^2 x}{\partial v^2} + \mu \frac{\partial^2 x}{\partial u^2} \right) \\ M_{uv} &= -(1-\mu) D \frac{\partial^2 x}{\partial u \partial v} \end{aligned} \quad (\text{B4})$$

where  $D = Eh^3/[12(1-\mu^2)]$ ,  $\mu$  is Poisson's ratio and  $h$  is the thickness of the surface.

Substituting (B4) into (B3) and introducing the following constants

$$\begin{aligned} S_{1x} &= S_{3x} = D \\ S_{2x} &= 2D \end{aligned} \quad (\text{B5})$$

we obtain the fourth order partial differential equation for  $x$  component as follows

$$S_{1x} \frac{\partial^4 x}{\partial u^4} + S_{2x} \frac{\partial^4 x}{\partial u^2 \partial v^2} + S_{3x} \frac{\partial^4 x}{\partial v^4} = F_x \quad (\text{B6})$$

For  $y$  and  $z$  components, similar equations to (B6) can be derived. Putting the fourth order partial differential equations for  $x$ ,  $y$  and  $z$  components in a vector-valued form, we obtain equation (7).



Dr. L. H. You is currently a senior research lecturer at the National Centre for Computer Animation, Bournemouth Media School, Bournemouth University, UK. His research interests are in computer graphics, computer animation and geometric modelling.



Dr. Baoping Tang received the B.Sc. degree from Chongqing Technology University, China, in 1993, and received the M.Sc. degree and Ph.D. degree from Chongqing University, China, in 1996 and 2003, respectively. He is a professor at Chongqing University, China. His research interests include software engineering, virtual instrument and wireless sensor network.



Mr. X. Y. You is currently a part-time MSc student with Coventry University, UK. He was awarded a BSc degree in computer science by the University of Warwick, UK. He is interested in the research into computer graphics etc.



Dr. Jian J. Zhang is Professor of Computer Graphics at the National Centre for Computer Animation and Director of Computer Animation Research Centre, Bournemouth Media School, Bournemouth University. His research interests include computer graphics, computer animation, physically-based simulation, geometric modeling, medical simulation and visualisation.





## An Adaptive Switching Filter for Removing Impulse Noise from Highly corrupted Images

R.Kulkarni<sup>1</sup>, S.Meher<sup>2</sup>, J.M.Nair<sup>3</sup>

Department of Electronics & Communication Engineering, NIT Rourkela<sup>1,2</sup>, VESIT<sup>3</sup> Mumbai  
rk1\_2002@yahoo.com<sup>1</sup>

### Abstract

This paper proposes a simple yet effective algorithm for effectively denoising the extremely corrupted image by impulse noise. The proposed method first classifies the pixels into two classes, which are “noise free pixel” and “noisy pixel” based on the intensity values. The corrupted pixels are replaced by “alpha trim-mean” value of uncorrupted pixels in the filtering window. The method adaptively changes the size of filtering window based on the number of “noise free pixels”. Because of this, the proposed method removes the noise much more effectively even at noise density as high as 90% and preserves the good image quality. The visual and quantitative results prove that the performance of proposed algorithm (PA) in the preservation of edges and details is far more superior to many of the median filtering techniques reported in terms of retaining the fidelity of the image highly corrupted by impulse noises. The proposed algorithm work very well for images with lower percentage of impulse noise also.

**Keywords:** Impulse noise, Nonlinear filter, Switching filter, Adaptive filter.

### 1. Introduction

Digital images, which are a subset to digital signals, are normally corrupted by many type of noise, including impulse noise. These impulses are salt and pepper like positive and negative in dances of larger strength corrupting the signal information. The malfunctioning pixels in camera sensors, faulty memory location in hardware, or transmission of the image in a noisy channel, are the some of the

common causes for impulse noise [1]. The intensity of impulse noise has the tendency of either being relatively high or low. Due to this when the signal is quantized to ‘L’ intensity levels, the corrupted pixels are generally digitized into either minimum or maximum values in the dynamic range, therefore these pixels appear as white or black dots in the image. Due to this it could severely degrade the image quality and cause some loss of image information. Keeping the image details and removing the noise from the digital image is a challenging part of image processing.

Various filters have been proposed for denoising in the past and it is well known that linear filters could produce serious image blurring. As a result, non-linear filters have been widely exploited due to their much improved filtering performance, in terms of noise removal and edges/details preservation. Median filter is one of the order-statistic filters, which falls in the group of non-linear filter; very much suitable for impulse noise filtering [2],[3], because of their simplicity and capability of preserving image edges/details. Nevertheless, because the typical median filters are implemented uniformly across the images, they tend to modify both ‘noise’ and ‘noise free’ pixels. To avoid the damage of good pixels, the switching scheme is introduced [4]-[6]. The switching impulse noise filters split the filtering process into two steps; 1) detection of noisy pixels, and 2) replacement of noisy pixels with estimated value. A lot of decision based median filters have been proposed, like, multi-state median (MSM) filter [7], Switching Median (SM) filter [8], and adaptive two-pass rank order filter (ATPMF) [9]. The MSM filter is adaptively



switched among those of a group of center weighted median filter (CWMF) [10] with varying center weights. The SM filter is based on the minimum absolute value of four convolutions obtained using one-dimensioned Laplacian operators for edge preservation to reduce impulse noise. ATPMF uses two-pass filtering, in which ; it detects irregularities in the spatial distribution of the estimated impulse noise by median filter, and then selectively replaces some pixels changed by the first pass of filtering with their original observed pixel values for keeping unchanged during the second pass. Additionally some methods such as homogeneity level information [11], and fuzzy filter [12] are proposed where they required previous training.

In this paper new noise detection and correction technique is proposed, which does not require optimizing parameters or previous training as required in some methods. The new method is a hybrid of adaptive and switching filter. The method can remove the impulse noise effectively from image, and at the same time can preserve the details inside the image, even when the input image is very highly corrupted by the noise. Because of this parameter it is much suitable for an automated system.

This paper is organized as follows:

Section 2 describes the proposed method in details. Section3 presents the results and discussions. Section 4 concludes the paper.

## 2 Proposed Method

The proposed method is the combination of adaptive and switching filter. The adaptive filter concept is used in order to enable the flexibility of filter to change its size accordingly based on the approximation of noise density. The switching filter frame work is used in order to speed up the process as well as preserve the image information, because only the noisy pixels are filtered.

In the first stage of proposed method, the pixels are classified into “noisy” and “noise free” pixels based on whether the processing pixel lies between minimum and maximum value of selected window. In the second stage of algorithm, an adaptive window, whose initial size is defined by noise density, is used for filtering, and the noisy pixels are replaced by “alpha trim-mean” value of uncorrupted pixels in the processing window.

**Noise classification:** Let ‘B’ denote the corrupted image. For each pixel  $B(x,y)$ , a 2-D sliding window ‘ $S_{xy}$ ’ of size  $3 \times 3$  is selected such that the current pixel  $B(x,y)$  lies at the center of the sliding window. If

$$P_{\min} < B(x,y) < P_{\max}, P_{\min}=0 \text{ and } P_{\max} < 255 \quad (1)$$

where  $P_{\min}$  is minimum value and  $P_{\max}$  is maximum value of pixels in the processing window. Then the pixel  $B(x,y)$  is classified as “noise free” otherwise classified as “noisy” pixel. Based on this classification a binary flag image  $f(x,y)$  is generated, where the noisy pixels are represented by binary ‘1’ and noise free pixels are represented by binary ‘0’. The flag image is defined as

$$f(x,y) \begin{cases} 0, & P_{\min} < B(x,y) < P_{\max}, \\ & (P_{\min} = 0, P_{\max} < 255) \\ 1, & \text{Otherwise} \end{cases} \quad (2)$$

**Noise correction:** In this stage, the noisy image  $B(x,y)$  is filtered and produces the output image  $g(x,y)$ . The output image  $g(x, y)$  is defined as,

$$g(x,y) = [1 - f(x,y)]B(x,y) + f(x,y)m(x,y) \quad (3)$$

where  $f(x, y)$  is binary flag image, defined by equation (2), and  $m(x,y)$  is the alpha trim-mean value obtained from adaptive filtering window.

As  $f(x,y)$  only can take value of either ‘0’ or ‘1’, the output value of  $g(x,y)$  is equal to  $B(x,y)$  or  $m(x,y)$ . Thus, the calculation of  $m(x,y)$  is only done when  $B(x,y)$  is a “noisy pixel” (i.e.  $f(x,y) = 1$ ). For the “noise free pixel” (i.e.  $f(x,y) = 0$ ), the value of  $B(x,y)$  is copied directly as the value of  $g(x,y)$ . This significantly speeds up the process.

In this method an adaptive technique is used to determine  $m(x,y)$ . This means that the size of the filter used at every pixel location is changing according to the local information. A square filters (i.e.  $W_M=W_N$ ) with odd dimensions are used for filtering process as given by,

$$W = W_M = W_N = 2R + 1 \quad (4)$$

where, ‘R’ takes any positive integer value.

This method, similar to other proposed method [4], uses only “noise free” pixels that are contained in the contextual region, defined by the area of  $W \times W$  (filter size), as the samples for the calculation of  $m(x,y)$ . This procedure ensures that the value of  $g(x,y)$  will not be affected by the noise.

However, in this algorithm an adaptive filtering window is used. To determine the value of  $m(x,y)$  a rule is set that the minimum number of “noise free” pixels ‘ $N_c$ ’ needed for this calculation must be greater than or equal to half of the total number of pixels ‘ $S_{in}$ ’ in the filtering window. Where  $S_{in}$  is given by,

$$S_{in} = \text{round}(W \times W) / 2 \quad (5)$$



If a small sample size is taken, where the total “noise free” pixels are less than ‘ $S_{in}$ ’, these samples are not good enough to present the local information of the image properly when the noise level is high. If the size is too big that is also not enough to present the local information of the image properly. So, if size of window is adaptive then these problems can be reduced up to maximum extent.

The  $R_{min}$  (minimum size of filtering window) is calculated as follows:

Let  $N_1$  be the number of “noisy” pixels that have been detected (i.e. number of ‘1’ present in flag image  $f(x,y)$ ) and ‘N’ be the total number of pixels in the image. Using the value of  $N_1$ , estimate the impulse noise level ‘ $\beta$ ’ that can corrupt the image. The value of ‘ $\beta$ ’ is the ratio of the number of “noisy” pixels ‘ $N_1$ ’ to the total number of pixels ‘N’ in the image, which is defined as,

$$\beta = \frac{N_1}{N} \quad (5)$$

The value of ‘ $\beta$ ’ is in between ‘0’ and ‘1’ (i.e.  $0 \leq \beta \leq 1$ ).

In order to minimize the number of trials needed to find the correct filter size, the value of ‘ $R_{min}$ ’ is calculated by using following equation,

$$R_{min} = \left\lfloor \frac{1}{2} \sqrt{\frac{7}{1-\beta}} \right\rfloor \quad (6)$$

The value  $\lfloor Z \rfloor$  represents the floor value. By using ‘ $R_{min}$ ’, this will allow the algorithm to converge faster, because less looping is needed to find the correct window size ‘W’ for filtering. As the consequence, this will speed up the process.

The novel adaptive method for finding  $m(x,y)$  is described as follows.

- 1) Initialize the size of filter  $W = 2 R_{min} + 1$ , where ‘ $R_{min}$ ’ is a small integer value, defined by equation (6).
- 2) Compute the number of “noise free” pixels in the filtering window size  $W \times W$ .
- 3) If the numbers of “noise free” pixels are less than  $S_{in}$ , increase the filtering window by two.  

$$W = W + 2 \quad (7)$$
  
and return to **step - 2**.
- 4) Calculate the value of  $m(x,y)$ , based on “noise free” pixels contained in the filtering window.
- 5) Update the value of  $g(x,y)$  by using equation (3).

### 3. Simulation Results

In order to demonstrate the performance of the method, the proposed algorithm is tested using different gray scale images. Fig. 1 & 2 shows the visual quality of the proposed method along with

the other similar methods with noise density 80% for ‘Lena’ and ‘Elaine’ images respectively. The results clearly shows that proposed method removes the noise much more clear than the other methods. Fig. 3 & 4 shows that the proposed method removes the noise effetely even at noise density as high as 95%.

The performance measure is done by using parameters like Peak-Signal-to-Noise-Ratio (PSNR), Mean Square Error (MSE), and Universal Quality Index (UQI); they are defined by the following equations.

$$PSNR = 10 \log_{10} \left( \frac{255^2}{MSE} \right) \quad (8)$$

where MSE is mean-square error given by

$$MSE = \sum_{x=1}^M \sum_{y=1}^N (f(x,y) - \hat{f}(x,y))^2 \quad (9)$$

$$UQI = \frac{4 \sigma f \bar{f} \hat{f} \bar{\hat{f}}}{(\sigma f^2 + \sigma \hat{f}^2)[(\bar{f})^2 + (\bar{\hat{f}})^2]} \quad (10)$$

where

$$\bar{f} = \frac{1}{MN} \sum_x^M \sum_y^N f(x,y), ; \quad \bar{\hat{f}} = \frac{1}{MN} \sum_x^M \sum_y^N \hat{f}(x,y)$$

$$\begin{aligned} \sigma_f^2 &= \frac{1}{MN-1} \sum_x^M \sum_y^N (f(x,y) - \bar{f})^2, \\ \sigma_{\hat{f}}^2 &= \frac{1}{MN-1} \sum_x^M \sum_y^N (\hat{f}(x,y) - \bar{\hat{f}})^2, \\ \sigma_{f\hat{f}}^2 &= \frac{1}{MN-1} \sum_x^M \sum_y^N (f(x,y) - \bar{f})(\hat{f}(x,y) - \bar{\hat{f}}), \end{aligned}$$

where MN is total number of pixels and  $f$  and  $\hat{f}$  is original and filtered image respectively.

Table 1, 2, and 3 shows the comparison of PSNR, MSE and UQI for Lena image corrupted by different noise densities applied to different filters. Fig. 5, 6, and 7 respectively shows graphical comparison of the PSNR, MSE and UQI parameter.

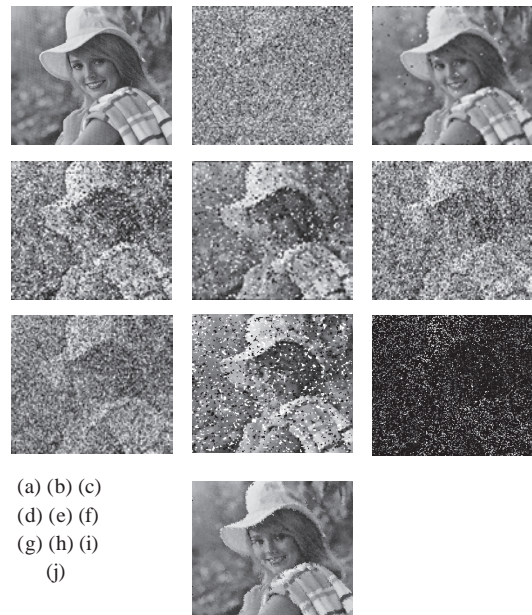
Extensive experimental results show that the proposed algorithm performs much better than some standard nonlinear medium and switching medium filters. From the parameter comparative table, it shows that the proposed method work better even for low and medium density noise and also preserve all fine details of image.





(a) (b) (c)  
(d) (e) (f)  
(g) (h) (i)  
(j)

Figure 1. (a) Original Lena Image (b) Noisy Image (noise density 80%). (c) AMF(3x3) (d) SWF (e) MF (7x7) (f) PSMF( g) CWMF (h) ATPMF (i) Rank Order MF (j) PA



(a) (b) (c)  
(d) (e) (f)  
(g) (h) (i)  
(j)

Figure 2. (a) Original Elaine Image (b) Noisy Image (noise density 80%). (c) AMF(3x3) (d) SWF (e) MF (7x7) (f) PSMF( g) CWMF (h) ATPMF (i) Rank Order MF (j) PA

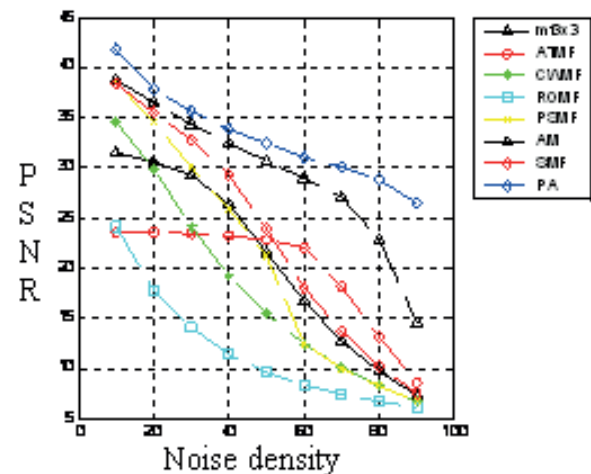


Figure 5. PSNR Plot

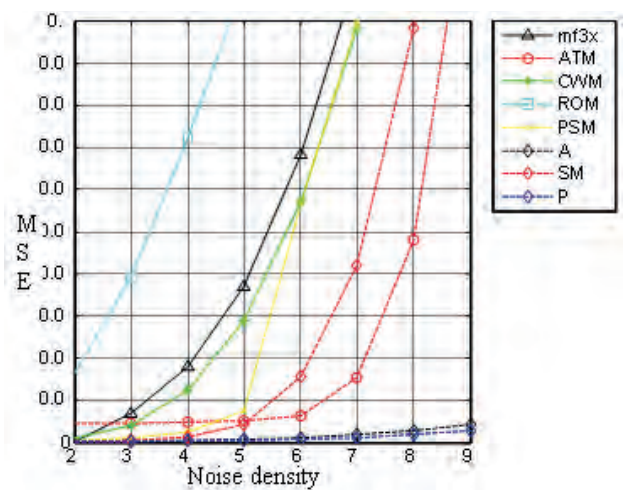


Figure 6. MSE Plot

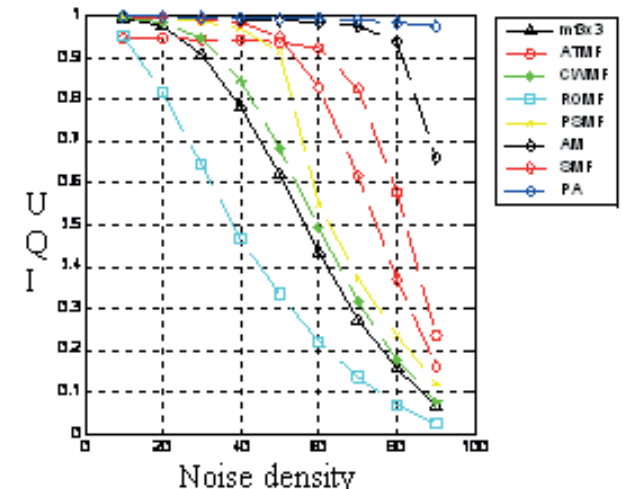
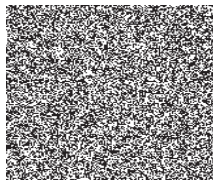


Figure 7. UQI Plot



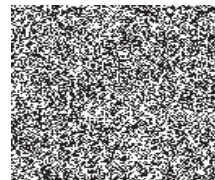


(a)



(b)

Figure 3: (a) 95% Noise density Lena Image



(a)



(b)

Figure 4: (a) 95% Noise density Lena Image

Table 1: Comparison table of PSNR of different filters for lena.jpg (512 x 512) image

Noise Density (%)	MF (3x3)	ATMF	CWMF	Rank - Order MF	PSMF	AM	SMF	PA
10	31.44	23.59	34.48	24.15	38.46	38.73	38.40	43.20
20	30.57	23.50	29.83	17.85	34.51	36.53	35.47	39.37
30	29.26	23.38	24.08	14.09	30.09	34.28	32.76	36.34
40	26.30	23.24	19.16	11.39	25.88	32.47	29.31	33.83
50	21.56	22.89	15.42	9.64	21.19	30.71	23.84	31.81
60	16.80	22.02	12.43	8.28	12.46	28.97	18.09	29.41
70	12.70	18.14	10.08	7.38	10.01	26.99	13.77	28.42
80	9.72	13.18	8.20	6.68	8.23	22.88	10.22	27.26
90	7.33	8.62	6.70	6.10	6.72	14.59	7.51	25.06

(MF = Median Filter, ATMF = Alpha-Trim Median Filter, CWMF = Center Weighted Median Filter, PSMF = Progressive Switching Median Filter, AM = Adaptive Median Filter, SMF = Switching Median Filter, PA = proposed algorithm)

Table 2: Comparison table of MSE of different filters for lena.jpg (512 x 512) image

Noise Density (%)	MF (3x3)	ATMF	CWMF	Rank - Order MF	PSMF	AM	SMF	PA
10	$3.84 \times 10^{-4}$	0.0044	$3.55 \times 10^{-4}$	0.0038	$1.42 \times 10^{-4}$	$1.33 \times 10^{-4}$	$1.44 \times 10^{-4}$	$4.7 \times 10^{-5}$
20	0.00017	0.0045	0.0010	0.0164	$3.53 \times 10^{-4}$	$2.22 \times 10^{-4}$	$2.83 \times 10^{-4}$	$1.1 \times 10^{-4}$
30	0.0069	0.0046	0.0039	0.0390	$9.78 \times 10^{-4}$	$3.72 \times 10^{-4}$	$5.29 \times 10^{-4}$	$2.3 \times 10^{-4}$
40	0.0180	0.0047	0.0123	0.0725	0.0026	$5.65 \times 10^{-4}$	0.0012	$4.1 \times 10^{-4}$
50	0.0370	0.0051	0.0287	0.1085	0.0076	$8.48 \times 10^{-4}$	0.0041	$6.6 \times 10^{-4}$
60	0.0683	0.0063	0.0571	0.1483	0.0567	0.0011	0.0155	0.0011
70	0.1114	0.0153	0.0981	0.1828	0.0996	0.0018	0.0420	.0014
80	0.1618	0.048	0.1511	0.2156	0.1502	0.0028	0.09848	.0018
90	0.2202	0.1371	0.2134	0.2452	0.2125	0.0043	0.1771	.0031

Table 3: Comparison table of UQI of different filters for lena.jpg (512 x 512) image

Noise Density (%)	MF (3x3)	ATMF	CWMF	Rank - Order MF	PSMF	AM	SMF	PA
10	0.9945	0.9461	0.9949	0.9528	0.9982	0.9983	0.9982	0.9992
20	0.9762	0.9450	0.9852	0.8178	0.9956	0.9972	0.9964	0.9985
30	0.9071	0.9435	0.9461	0.6435	0.9878	0.9953	0.9933	0.9974
40	0.7828	0.9416	0.8456	0.4662	0.9696	0.9923	0.9853	0.9954
50	0.6209	0.9368	0.6835	0.3360	0.9142	0.9893	0.9495	0.9931
60	0.4348	0.9234	0.4941	0.2196	0.5511	0.9841	0.8275	0.9890
70	0.2735	0.8252	0.3164	0.1369	0.3718	0.9749	0.6195	0.9865
80	0.1567	0.5767	0.1762	0.0698	0.2362	0.9367	0.3695	0.9822
90	0.0664	0.2346	0.0778	0.0263	0.1206	0.6599	0.1636	0.9701



#### 4. Conclusion

This paper presents a novel technique to remove impulse noise from low, medium & highly corrupted images. This is the hybrid method, which combines adaptive as well as switching filter. One of the advantages of this method is that this method doesn't need the threshold parameter. Thus no tuning or training is required; the filter size is adaptable to local noise density. Experimental results show that this method always produces good output, even when tested for high level of noise. The details inside the image are preserved. This method is simple and relatively a fast method and suitable for consumer electronic products such as digital camera.

#### 5. References

- [1] Raymond H. Chan, Chung-Wa Ho, and Mila Nikolova, "Salt-and-pepper noise removal by median-type noise detectors and detail preserving regularization", *IEEE Trans. Image Processing*, vol. 14, no. 10, pp. 1479-1485, October 2005.
- [2] Pitas, I., and Venetsanopoulou, A., 'Nonlinear digital filters: principles and application' (Kluwer, Nonvell, MA,), 1990.
- [3] H Lin and A.N Willson, "Median filter with adaptive length", *IEEE Trans. Circuits and Systems -II*, vol. 35, pp. 675-690, June-1988.
- [4] Zhou Wang, and David Zhang, "Progressive switching median filter for the removal of impulse noise from highly corrupted images", *IEEE Trans. Circuits and Systems -II: Analog and Digital Signal Processing*, vol. 46, no. 1, pp. 78-80, January 1999.
- [5] Yin, L., Yang, R., Gabbouj, M., and Neuvo, Y., 'Weighted median filters: a tutorial', *IEEE Trans. Circuits Syst.*, 43 (3), pp. 157-192, January 1996.
- [6] Shuqun Zhang and Mohammad A. Karim, "A new impulse detector for switching median filters", *IEEE Signal Processing Letters*, vol. 9, no. 11, pp. 360-363, November 2002.
- [7] Tao Chen and Hong Ren Wn, "Space variant median filters for the restoration of impulse noise corrupted images," *IEEE Trans. Circuits and Systems -II: Analog and Digital Signal Processing*, vol. 48, no. 1, pp. 784-789, Aug. 2001.
- [8] XXu, E. L. Miller, Dongbin Chen and M. Sarhadi, "Adaptive two-pass rank order filter to remove impulse noise in highly corrupted images," *IEEE Trans. Image Processing*, vol. 38, pp. 984-993, 1991.
- [9] KO, S.J., and LEE Y.H, 'Center weighted median filters and their application to image enhancement', *IEEE Trans. Circuits Syst.*, 38(3), pp190-195, 1991.
- [10] Eng.HL and Ma. K.K, 'Noise adaptive soft-switching median filter', *IEEE Trans. Image Processing*, vol.10, pp.245-252, 2001.
- [11] G. Pok, J.-C. Liu, and A. S. Nair, "Selective removal of impulse noise based on homogeneity level information," *IEEE Trans. Image Processing*, vol. 12, no.1, pp. 85-92, Jan. 2003.
- [12] F. Russo and G. Ramponi, "A fuzzy filter for images corrupted by impulse noise," *IEEE Signal Processing Lett.*, vol. 3, pp. 168-170, June 1996.
- [13] Besdok E. and Emin Yuksel M., Impulsive Noise suppression for images with Jarque-Bera test based median filter, *International Journal of Electronics and Communications*, Vol.59, pp. 105-110, 2005.
- [14] Chen T, Wu HR, Adaptive impulse detection using center weighted median Filters, *IEEE Signal Processing Letter*, Vol.8, pp. 1-3, 2001.



## Biographies



**R.K.Kulkarni** is a PhD scholar in the Department of Electronics & Communication Engineering, National Institute of Technology, Rourkela, Orissa, India. He received his bachelor degree in Electronics & Communication from Mysore University and master degree in Digital Electronics form Karnataka University, Karnataka. He has many publications in international journals and international conferences. His research area is Image processing, Non – Linear filters, and Digital signal processing.



**S.Meher** is currently working as associate professor in the Department of Electronics & Communication Engineering, National Institute of Technology, Rourkela, Orissa, India. He received is PhD from NIT, Rourkela, Orissa, India. He has many publications in international journals and international conferences. His research area is Image processing, Non – Linear filters, and Digital signal processing. He guided number of PhDs.



**J.M.Nair** is currently working as principal in VES institute of Technology, Mumbai, India. She received her bachelor degree in Electrical and master degree in Control Systems form Kerala. She received her PhD from IIT Mumbai, India. Her research area is Image processing, robust control, and passivity control . She guided number of PhDs. She has many publications in international journals and international conferences.







## Reducing Change of Illumination Effect for Hyperspectral Image Unmixing

Z. B. Rabah<sup>1,2</sup>, I. R. Farah<sup>1,2</sup>, B. Solaiman<sup>2</sup> and H. B. Ghzala<sup>1</sup>

<sup>1</sup> RIADI GDL laboratory

School of Engineering and Computer Science, Manouba, Tunisia

<sup>2</sup> ENST-Bretagne, ITI laboratory

Technopôle Brest Iroise CS 83818, 29238 Brest Cedex France

zouhairbr@yahoo.fr, riadh.farah@ensi.rnu.tn, henda.benghala@cck.rnu.tn, Basel.Solaiman@telecom-bretagne.eu

### Abstract

In the field of the processing of hyperspectral images, the pixel mixture is a serious problem to resolve. This difficulty comes from several outliers which affect seriously the reliability of spectral unmixing results. The illumination change effect, where the image do not reflect the true appearance of the scene in many cases due to primarily by slope or shadow facts, is considered one of the most important outliers and it is essential to deal with this problem which can otherwise have a serious effect on the estimation results.

Several attempts have been made to correct this problem which is not currently handled by atmospheric correction: these approaches allow the Endmembers of the mixture to be random variables (mostly Gaussians) and lack the ability to explain the statistical variability of the spectra within a class.

The present work propose a new approach called Independent Component Analysis and Spectral Angle Measure based Spectral Unmixing (ICA-SAM-SU) which use the spectral angle constraint for abundance quantification. The major benefit of this approach is its capability to estimate abundance quantification independently of the amplitude (magnitude) of the spectral signatures, using only spectral angle measures. As a consequence, a significant reduction in spectral unmixed error corresponding to the spectral similarity within-class confusion is obtained. A second benefit concerns physical constraints which are respected. The experiment was conducted using simulated and real image in order to validate our approach and to compare it with a well known statistic one.

**Keywords:** Abundance quantification, Endmember extraction, hyperspectral image, spectral angle measure, change illumination, shadow, slope.

### 1. Introduction

Theoretically, a pixel in an hyperspectral image represents a certain ground cover material, and each pixel can be uniquely assigned to only one ground cover class. Unfortunately, this assumption is not true, because many different materials are mistakenly classed together in the same pixel which leads to the mixed pixel that we denoted “pixel” [1]. This arises for one or two reasons. First, if the spatial resolution of an imaging sensor is low enough such that adjacent Endmembers (EMs) can jointly occupy a single pixel where an EM is an idealized pure signature for a class. Then the resulting spectral measurement will be a composite of the individual EMs. Second, this phenomenon appears when the spectral resolution of an imaging sensor is high enough, the resulting overlapping signatures [2]. Dealing with spectral signature compositions in pixel signal sources extraction and abundance quantification are then one of the most challenging problems in spectral unmixing.

Spectral unmixing techniques broadly fall into two categories: geometric algorithms and statistical models. The geometric methods such as pixel purity index (PPI) [3], N-finder (N-FINDR) algorithm [4], iterative error analysis (IEA) [5], automated morphological EM extraction (AMEE) algorithm [6], minimum volume transform (MVT) [7], convex geometry [8], convex cone analysis [9], use the distribution of hyperspectral data to fit a simplex to a set of hyperspectral data in order to extract EM spectra. Those methods share three significant drawbacks. First of all, they assume the presence in the data of at least one pure pixel of each EM. This is a strong requisite that may not hold in some data sets. Second, their difficulty to estimate the number of EM and to quantify their abundance. Third, which



can lead to ambiguous results in spectral unmixing and consist in considering some of the geometrically determined EMs having reflectance values that are greater than one and less than zero, which violates the physical model?

Those methods share a specific and significant drawback, however, is that aberrant pixels that arise due to sensor artifacts may also be identified as endmembers. As a consequence, geometric techniques are especially suited to identifying low-probability targets, but they perform best with data that are free of artifacts that can create spurious results.

Unlike, the statistical approaches such as Independent Component Analysis (ICA) which is the most used one [10] for its ability to classify objects with unknown spectral signatures in an unknown image scene. This method is based on minimizing the error of a statistical model of the hyperspectral data and take advantage from mathematical modeling to cope with the geometric approach drawbacks.

For this purpose, Chang proposes in [11] an abundance quantification algorithm such as fully constrained least squares linear mixture analysis (LSMA). In [10], Wang and Chang propose an ICA-based Abundance Quantification Algorithm (ICA-AQA) that enables EMs extraction and EMs abundance estimation simultaneously. Certainly, all these statistical methods shared the same objective but the same drawback too. The first is the need to solve the linear unmixing problem in the remote sensing field. The second is their sensitivity for illumination change caused primarily by shadow and slope facts.

In fact, several degradation mechanisms are normally found in hyperspectral applications namely signature variability, topography modulation, and noise. Thus observed data are not representing the real true values which negatively affect analysis processes particularly in abundance map quantification. This is why shadow and slope effects have drawn much attention by researchers [12] with increasing use of high-spectral remote sensing images of multi altitude areas.

To overcome this drawback for abundance map generation, we proposed a theoretical method called ICA and Spectral Angle Measure based Spectral Unmixing (ICA-SAM-SU) that use both Linear Mixture Model (LMM) and spectral angle measures (SAM) to derive a mathematical linear relationship between the fractional abundance of each source and spectral deviation of the observed mixel spectrum with each EM.

The paper is organized as follows. In Section 2, Linear Mixture Model (LMM) is presented as well as BSS method. The traditional Spectral Angle Mapper is presented in section 3. In Section 4, the ICA-SAM-SU is proposed and discussed. One experiment is carried out in Section 5 emphasizes the robustness of the proposed abundance estimator to ICA-AQA. Accuracies of the two estimators are compared through synthetic image and real image to quantify abundance. The last section concludes the paper.

## 2. Linear Mixture Model and ICA

Any approach for effectively unmixing hyperspectral data must begin with a model describing how constituent material substances in a pixel combine the composite spectrum measured at the sensor.

To this end, LMM have been used extensively for characterizing spectral data proving successful in geological applications [13]. One major reason why the LMM has been broadly accepted for the spectral unmixing analysis is that linear mixture assumption allows many mature mathematical skills and algorithms, to be easily applied to the spectral unmixing problem. The LMM assumes that each ground cover material only produces a single radiance, and the mixed spectrum is a linear combination of ground cover radiance spectra. So the spectrum for a given pixel is a linear combination of the EM spectra.

$$x_i = \sum_{k=1}^P \alpha_k m_k^i + \varepsilon \quad (1)$$

Where  $x_i$  is a given pixel in the  $i$ -th band,  $m_k^i$  is the  $k$ -th EM of the  $i$ -th band,  $\alpha_k$  is the mixing proportions of the  $k$ -th EM in the  $i$ -th pixel, and  $\varepsilon$  is additive Gaussian random error. It takes into account the sensor noise, the spectral variability, the atmosphere fluctuations and other model inadequacies. Indeed, the pixel compositions are assumed to be in percentages. To be physically realizable, the abundance coefficients should be non negative (eq.2) and should sum to one (eq.3) [14].

$$\forall k = 1, \dots, P, \quad \alpha_k \geq 0 \quad (2)$$

$$\sum_{k=1}^P \alpha_k = 1 \quad (3)$$

The unmixing technique solves a set of  $n$  linear equations for each pixel, where  $n$  is the number of bands in the image [15]. The unknown variables in these equations are the fractions of each EM in the pixel. To be able to solve the linear equations for the unknown pixel fractions it is necessary to have more equations than unknowns, which means that we need more bands than EM materials. With hyperspectral data this is almost always true.



ICA applied to hyperspectral images uses LMM [16], assuming the statistical independence of the sources and no more than one component can be gaussian. Performing a ICA to hyperspectral image consists in finding the linear transform  $W = A^{-1}$  which maximizes the statistical independence between the components of the random vector sources according to the linear mixture models (LMM) [17].

### 3. Spectral Angle Mapper

In  $N$  dimensional multi-(or hyper) spectral space a pixel vector  $x$  has both magnitude (length) and an angle measured with respect to the axes that defines the coordinate system of the space [18]. Only the angular information is used for identifying pixel spectra in the Spectral Angle Mapper (SAM) technique based on the assumption that an observed reflectance spectrum is a vector in a multidimensional space, where the number of dimensions equals the number of spectral bands. The spectral similarity between any two spectra pixel vectors is given by (eq.4).

$$\text{SAM}(s_i, s_j) = \cos^{-1} \frac{\langle s_i, s_j \rangle}{\|s_i\| \|s_j\|} \quad (4)$$

Where  $\langle s_i, s_j \rangle = \sum_{l=1}^L s_{il} s_{jl}$ ,

$$\|s_j\| = (\sum_{l=1}^L s_{jl}^2)^{1/2} \text{ and } \|s_i\| = (\sum_{l=1}^L s_{il}^2)^{1/2}$$

Where

$$s_i = (s_{i1}, s_{i2}, \dots, s_{iL})^T$$

and  $s_j = (s_{j1}, s_{j2}, \dots, s_{jL})^T$  are two pixel spectrums in  $L$ -dimensions. The superscript T stands for a vector or matrix transposition.

This method assumes that the data have been reduced to apparent reflectance and uses only the "direction" of the spectra, and not their "length". As a consequence, this method is insensitive to changes in pixel illumination caused by external factors because increasing or decreasing illumination does not change the direction of the vector, only its magnitude (i.e., a darker pixel will plot along the same vector, but closer to the origin).

### 4. ICA and Spectral Angle Measure-based Spectral Unmixing

Spectral unmixing is a quantitative analysis procedure used to recognize constituent ground cover materials or EM and to obtain their mixing proportions (or abundances) from a mixed pixel. In order to reliably estimate these two variables, with respect to physical conditions (eq.3) and (eq.4), we

present in this section the proposed unmixing method (ICA-SAM-SU) the proposed approach is presented in figure. 1.

#### A. Dimensionality reduction

In many classification problems, high-dimensional data are involved, because large feature vectors are generated to be able to describe complex objects and to distinguish between them.

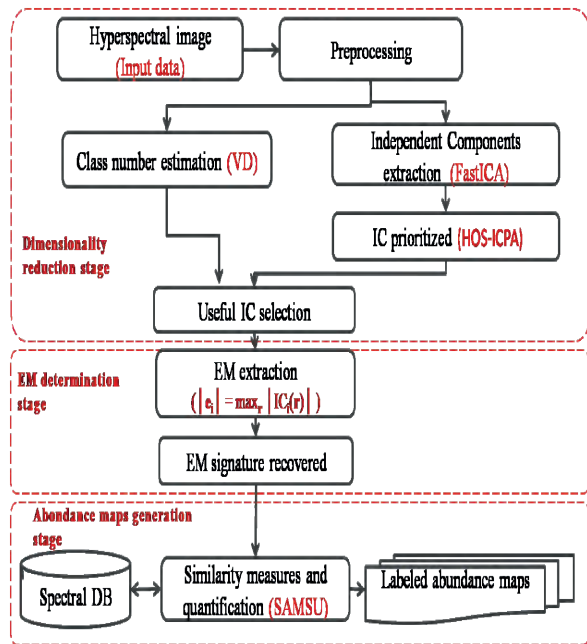


Figure1: Proposed approach for EM extraction and abundance quantification.

The reason for doing the dimension-reduction stage is then to reduce the computational load of subsequent processing dimension of the data in the scene and to improve classification performance through more removal of redundant or irrelevant information.

This can be done in several ways. The easiest way is to identify only the axes that contain the most energy in a scene [13]. The basic idea of dimensionality reduction is to first determine the number of ICs needed to be retained,  $p$  which can be estimated by the VD [14]. It then prioritizes the FastICA-generated ICs [19] using a high-order statistics criterion (HOS-ICPA) [11] to select the first  $p$  prioritized and useful ICs with  $p$  highest priority scores is to take advantages of the Fast-Independent Component Analysis (FastICA-2D) generated ICs that separate all extracted presumed EM pixels in individual components [18]. However, in a hyperspectral image analysis, commonly there are between one and three hundred of spectral bands, each one corresponding to a CI, therefore useful information is contained in only a dozen or fewer of



components image. Accordingly, appropriate ICs must be selected for an eventual efficient exploitation. Among the solutions for this problem addressed and investigated in the literature, this paper selects one among two algorithms developed in [19] that allows sorting the CIs in decreasing order in terms of utility degree. The selected one is named the high-order statistics-based IC prioritization algorithm (HOS-ICPA) which uses high-order statistics to affect a priority score to each generated IC. Following this, Virtual Dimensionality (VD) [13] algorithm was performed to estimate the number of sources within the scene. Then, the same number was used to determine the number of CIs needed to be selected, let  $p$  this number.

### B. EM determination

An accurate assessment of subpixel composition begins with a reliable EM estimation estimate of what pure substances comprise mixed pixels in the scene. To this end, Chang proposes in [10] an easy idea, to find for each of the  $p$  selected FastICA generated IC from previous stage images, a pixel with maximum absolute value  $|\mathbf{e}_i| = \max_{\mathbf{r}} |\mathbf{IC}_i(\mathbf{r})|$  which is the maximum of  $|\mathbf{IC}_i(\mathbf{r})|$  over all the image pixels in the  $\mathbf{IC}_i$ , which is supposed to be an EM and that is assumed to be pure. Then, each EM spectral signature is obtained from the observed image using spatial location corresponding to each EM extracted from previous step.

In order to label each EM, the SAM technique was performed by matching each EM signature with a calibrated spectral library produced by Spectroscopic measure campaign. Of course, the match will rarely be exact, because of modeling noise and error.

### C. Abundance quantification

This section, discusses the mathematical definition of the proposed abundance quantification method ICA-SAM-SU. The idea is to estimate the fractional abundances for each mixel using its spectrum and the EM spectra set. Mathematically, this consist to transform the equation system for the linear spectral unmixing problem, to a quadratic one (determined system) having unique solution independently of the magnitude of the observed and EM pixels. Our rationale is based on one primary observation, which is, a linear relationship exists between the fractional abundance of the substances comprising the area being imaged and the spectrum of the reflected radiation.

To this end, the aim of the ICA-SAM-SU method is to obtain an optimum and unique estimate value for

the abundances  $a_k$ .

Being given a mixel spectrum  $x_i$  and EM spectra  $m_k$  supposed statistically independents. Now, starting with (eq.1) as an expression of a linear mixture model where  $\varepsilon$  is defined as an additive white Gaussian noise considered as negligible [20] [15]. This equation can be rewritten to,

$$\mathbf{x}_i = \sum_{k=1}^p a_k m_k^i \quad (5)$$

Being given, the EMs  $(m_1, m_2, \dots, m_p)$  extracted previously, the aim is to resolve (5) under constraints (2) and (3).

$$\text{We assume } m_k = [m_k^1, \dots, m_k^L]^T$$

$$X = [x_1, \dots, x_L]^T$$

$$A = [a_1, \dots, a_p]^T$$

And  $M = [m_1, \dots, m_p]$  Equation (5) can be written :

$$X = MA \quad (6)$$

In the field of the hyperspectral imagery,  $L > p$  then  $M$  is not a square matrix and the problem can be resolved by .... method (5) can be rewritten as

$$X = [m_1, \dots, m_p][a_1, \dots, a_p]^T = \sum_{k=1}^p a_k m_k \quad (5)$$

So, basing on the (6) and (3), we can conclude that  $X$  represents the barycenter of the EMs

$(m_1, m_2, \dots, m_p)$  and the constraint (2) indicate that  $X$  belong to the convex formed by the EMs

The solution of the (6) without constraint

(eq.2) and (eq.3) can be written:

$$X = MA \Rightarrow M^T X = M^T M A$$

Let  $M^T M = \Gamma$  then (6) can be rewritten as

$$\Gamma A = M^T X$$

$$\Gamma_{ij} = \langle m_i, m_j \rangle \quad (8)$$

So,  $\Gamma$  is square matrix  $p \times p$ , symmetric and positive definite then Reversal

$$A = \Gamma^{-1} M^T \quad (9)$$

Where  $M^T X$  measure the degree of similarity between EMs and observed pixel.

Three cases can be distinguished:

- The observed pixel  $X$  belongs to the convex formed by the EMs, then the two constraints (eq.2) and (eq.3) are verified.
- The observed pixel  $X$  doesn't belong to the convex formed by the EMs but crossed it (example change illumination impact). Then it can be considered as the barycenter of EMs and the origin O as shown in figure 2. In that



case only the constraint (eq.2) is verified. The pixel value is corrected by the projection on the convex. What means normalizing the coefficients  $\alpha_i$

$$\beta_i = \frac{\alpha_i}{\sum \alpha_i} \quad (10)$$

- c) the last case where the pixel where the pixel is not contained in the cone formed by the EMs, then the constraints (eq.2) and (eq.3) can't be verified and the pixel was affected to an unknown class.

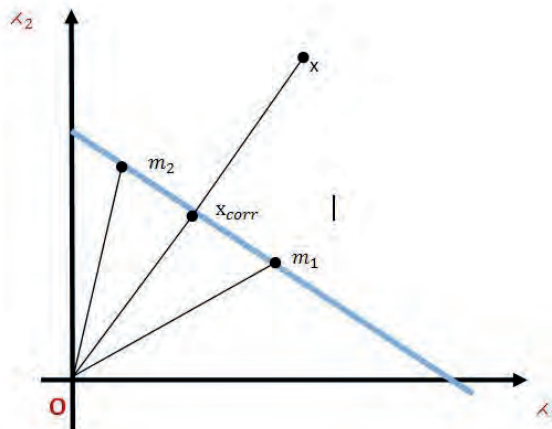


Figure 2: observed pixel cross the convex

## 5. Experiments, results and discussion

The objective of computer simulations is to use laboratory data at our disposal to design various scenarios to verify the utility of the proposed ICA-SAM-SU approach in solving a particular spectral unmixing problem. In the first experiment, mineral data available from the United States Geological Survey (USGS) website were used to produce synthetic image for this end. Five targets EM were chosen (Alunite (A), Buddingtonite (B), Calcite (C), Kaolinite (K), and muscovite (M)). And their spectral signatures were plotted in Figure 3.

Using these signatures, a synthetic image scene with size of  $64 \times 64$  pixels was simulated according to Figure 4 where the objects have been set into lines and columns.

The image background was made up of 50% Alunite and 50% Kaolinite and three other minerals Buddingtonite, Calcite, and Muscovite were used to simulate 24 panels of different abundance fractions with those panels in first, second, and third columns specified by Buddingtonite, Calcite and Muscovite, respectively. These 24 panels were then implanted into the image background in a way that the corresponding background pixels were replaced by the pixels in the 24 panels. Except three panels in the first row labeled by 100%, which contained four pure mineral pixels, all other panels were single-

pixel panels with various abundance fractions. It is worth noting that the panel pixels with abundance fractions less than 100 were mixtures of the panel signature with the background. For example, the panel pixel labeled by 80% in the first column is a mixture of 80% Buddingtonite with 20% background signature (BKG).

### A. Simulation image

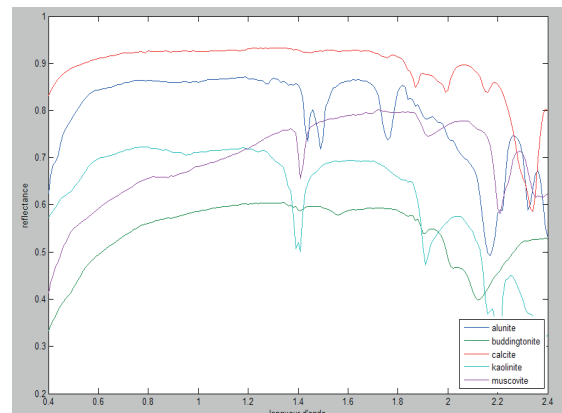


Figure 3: Five mineral spectra

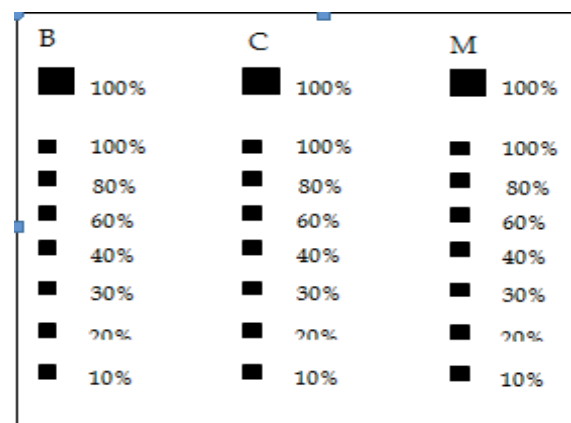


Figure 4: Synthetic image with specified abundance fractions

As explained in the previous section, obtained abundance maps are images, whose grey level values accuracy depends of the method robustness and the respect to the physical constraints (eq.2) and (eq.3). In Figure 5, abundance maps of the three objects (laboratory spectral signature) are estimated with ICA-AQA. On the other hand, those who are presented in Figure 6 are estimated with ICA-SAM-SU method.



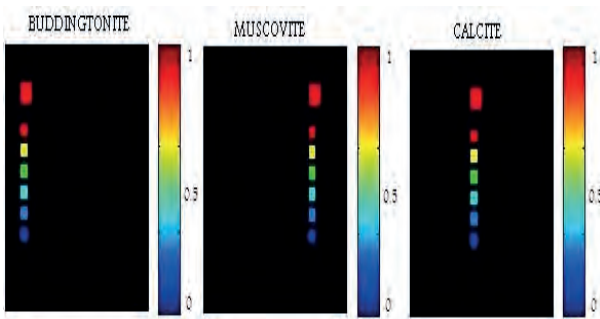


Figure 5: Abundance quantification for BKG and each EM using ICA-AQA

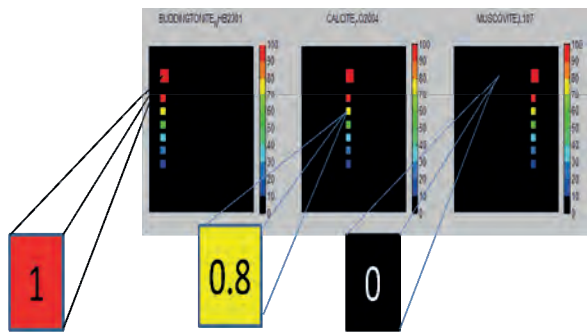


Figure 6 : Abundance quantification for BKG and each EM using ICA-SAM-SU

It is clearly shown that in any case, ICA-AQA or ICA-SAM-SU return abundances near to 1 if the EM is expected in the pixel and approximately null in the background (Figure 5, 6, line 1, 2). If we focus on the first EM (Buddingtonite) abundances, results would seem accurate for both estimators with a little improvement for the proposed method shown through table1.

Ground truth	ICA-AQA		ICA-SAM-SU	
	Estimation	Error	Estimation	Error
100	100	0	100	0
80	80.24	0.24	80.00	0
60	60.46	0.46	60.21	0.21
40	41.10	1.10	40.47	0.47
30	30.78	0.78	30.66	0.66
20	20.91	0.91	20.71	0.71
10	10.96	0.96	11.09	1.09

Table 1 : Abundance estimation of the Buddingtonite EM

This similar result given by both methods is explained by the nature of used data which are not affected by signal pixel amplitude variance problem. A second constation deduced from this experiment is that the lower the EM abundance, the higher the relative error of estimation. This is caused by the signal to noise ratio that decreases relatively with the EM abundance.

Up to now, computer simulations were used to demonstrate the effectiveness ICA-SAM-SU in spectral mixture analysis. In the follows, the

insensitivity of the proposed method to the number of spectral bands and to signal pixel amplitude (magnitude) variance will be tested. To this end, each spectra of each pixel presented in the simulated hyperspectral image was multiply by a random value between 0 and 1 keeping so reflectance constraint (radiometric value of a given pixel is under to 1). Then, both methods ICA-AQA and ICA-SAMSU were applied to the modified image. The results of each approach is shown respectively in figure 7 and figure 8

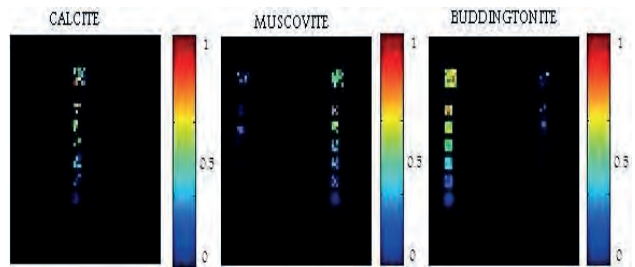


Figure. 7: Result of the ICA-AQA applied on the modified image

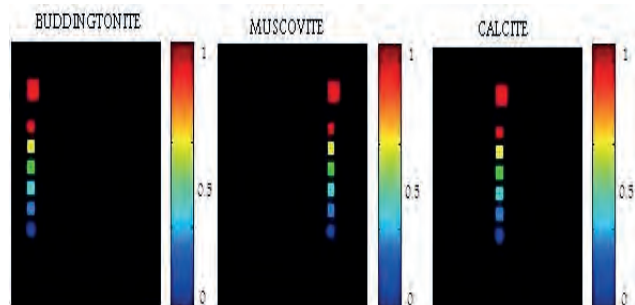


Figure 8. : Result of the ICA-SAM-SU applied on the modified image

Visual comparison, between abundance fraction estimates by ICA-AQA (Figure 7) and those estimated by our proposed method ICA-SAM-SU (Figure 8) applied on the modified simulated image, confirm the invariance of our approche, to signal pixel amplitude variance, compared to the obtained abundance maps using no modified simulated image. Unlike ICA-AQA shows otherwise, confirming so its sensibilty to signal pixel amplitude variance.

## B. Validation with Hyperion image

As our approach has demonstrated its robustness using a simulated image, it is meaningful to test it on real image. To this end, a case study was conducted using a subset of an Hyperion image dataset. The launch of NASA's EO-1 Hyperion sensor in November 2000 marked the establishment of spaceborne hyperspectral mineral mapping capabilities. Hyperion is a satellite hyperspectral sensor covering the 0.4 to 2.5  $\mu\text{m}$  spectral range with 242 spectral bands at approximately 10 nm spectral resolution and 30 m spatial resolution from



a 705-km orbit [22]. The study area is a mountainous region located in the south-eastern part of Tunisia, characterized by a geologic site investigated by National Remote Sensing Center in Tunisia. Extensive field work has been done in this area, and the HYPERION scene covering it has been previously acquired on the 13 February 2009.

First at all, data clean-up was applied to the data prior to atmospheric correction. Though radiometric corrections were applied prior to data delivery to analyze step, there was still a pronounced dark columns in the data. This drawback is corrected using adjacent column interpolation method under IDL/ ENVI 4.2 software. The result only 152 useful are retained (figure 8).Then atmospheric correction is performed on the Hyperion image using empirical line method in order to illuminate the absorption and scattering effects of the atmosphere. The methodology requires processing radiance-calibrated data to apparent reflectance.

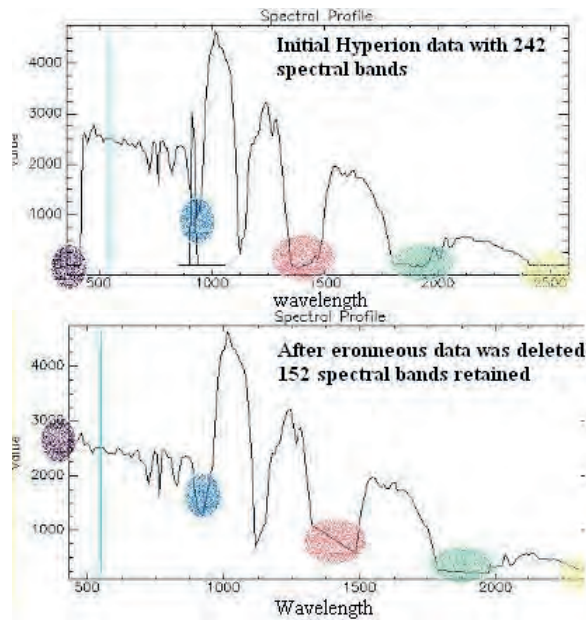


Figure 9 : Elimination of the undesired bands

In order to avoid infinite computing time, only a subset with 142 by 139 pixels size was used for this experiment as shown in Figure 10.

The idea of this experiment is to use real data to various scenarios to verify the utility of the ICA-SAM-SU in solving the sensitivity of spectral unmixing problems to the signal pixel amplitude variance. Furthermore, ICA-SAM-SU results will be compared with a classic approach ICA-AQA results to show that the performance of abundance quantification can be improved. This improvement performance stems from the possibility to ensure the separability measured by within-class variances and between-class variances.

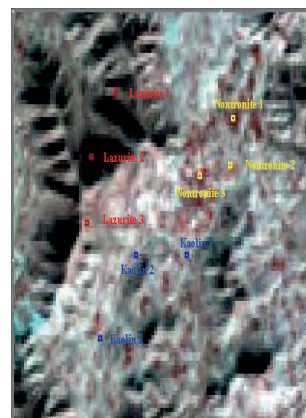


Figure 10 : A pseudo-color subset of Hyperion image 142x139 pixels

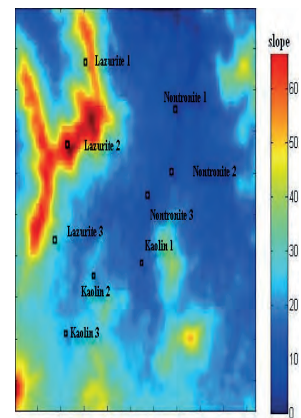


Figure 11 : Correspondent slope map

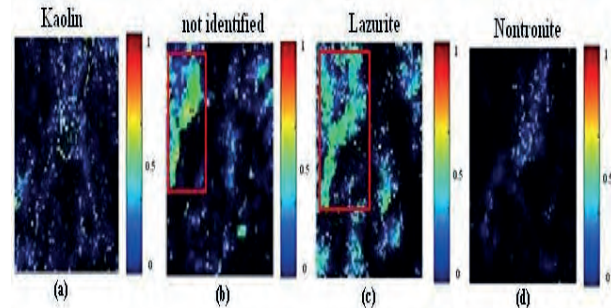


Figure 12 : Abundance quantification of the subset image using ICA-AQA

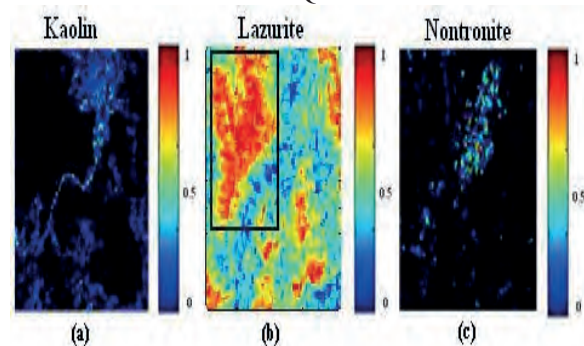


Figure 13: Abundance quantification of the subset image using ICA-SAM-SU method

To this end, we generate first, different ICs from Hyperion image subset using the FASTICA-2D [20] technique then we apply the VD algorithm [14] in order to estimate the number of assumed pure spectral signature (APSS) located in the scene. As a result this number is estimated to 4. A priority score is then calculated for each IC using HOS-ICPA algorithm [13] and the 4 APSS was extracted from the image and then labeled using SAM matching technique and laboratory spectral signature data base. The next steps consist in generating in the first place abundance quantification maps referring to the ICA-AQA method as shown in figure 12 and then in the second place the ICA-SAM-SU method as shown in figure 13.

According to a visual comparison of the abundance maps obtained by ICA-SAM-SU and these given by



the commonly used ICA-AQA method, the proposed method was shown significantly more efficient against change illumination problems caused by slope effect. This is illustrated in particular through image (b) and (c) of the figure 12 which present incorrectly two abundance maps for the same material (Lazurite). Unlike, the result given by ICA-SAM-SU method and illustrated in image (b) of the figure 13 presents significant reduced confusion caused by change illumination problems.

In order to quantitatively evaluate this first observation and to highlight the invariance of our proposed approach to amplitude variability, we examine this particular case through some samples pixels spectra as located in the Hyperion image subset (figure 10) with her correspondent slop map (figure 11). It was noted that these samples pixel are organized in three relatively homogenous (checked by ground truth) pixels set and marked by their material type and every set belongs to the same class but located in three different slopes as illustrated respectively in the figures 10 and 11.

Through figure 14, 15 and 16, we present the spectral signatures for these samples. Each image represents three spectra vector that have approximately the same direction but not the same profile (magnitude) due to some error outlier such as illumination variability phenomenon [13].

The ICA-SAMSU (3) was implemented and evaluated in comparison with the ICA-AQA for performance analysis. The experiment demonstrates that the proposed method ICA-SAMSU was able to reduce confusion between Lazurite 1, 2 and 3. In other words, it considers them as the same material (figure 12). On the contrary, ICA-AQA considers them as two different materials Lazurite and undefined one. Therefore we obtain one abundance false map moreover for undefined material (figure 13). Table 2 presents the quantification results of the samples pixels produced by the ICA-AQA and ICA-SAMSU. Also included in Table 2 are the abundance quantification results of all samples pixels produced by the two techniques and evaluated by their variability within class (VWC) with

$$VMC = \frac{1}{N} \sum_1^N (x_i - \bar{x})^2$$

N: number of sample; x: quantification fraction;  $\bar{x}$ : quantification mean value

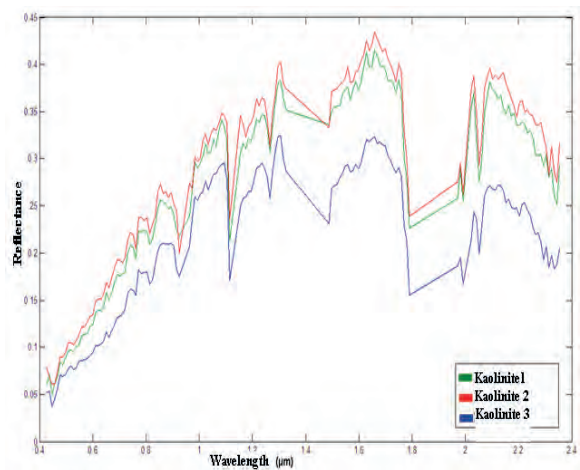


Figure 14 : Reflectance spectra for several pixels derived from the Kaolinite spectra samples . A multiplicative scaling effect is clearly evident in the spectra, but the shape of the spectra itself is nearly invariant

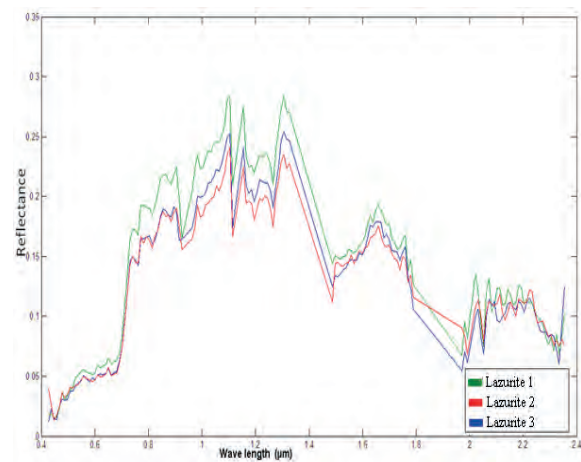


Figure 15 : Reflectance spectra for several pixels derived from the Lazurite spectra samples . A multiplicative scaling effect is clearly evident in the spectra, but the shape of the spectra itself is nearly invariant.

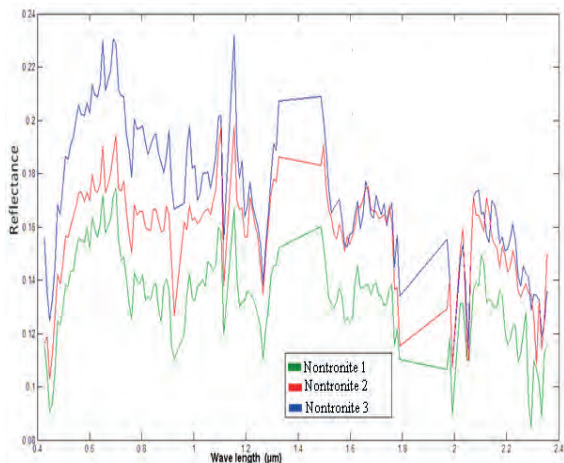


Figure 16 : Reflectance spectra for several pixels derived from the Nontronite spectra samples . A multiplicative scaling effect is clearly evident in the spectra, but the shape of the spectra itself is nearly invariant.



Sample	Pixel position	ICA-SAMSU	ICA-AQA
Kaolinite 1	(75,32)	0.906	0.819
Kaolinite 2	(75,66)	0.924	0.526
Kaolinite 3	(32,84)	0.917	0.619
VWC		0.062	1.494
Lazurite 1	(58,22)	0.986	0.906
Lazurite 2	(48,52)	0.991	0.689
Lazurite 3	(35,60)	0.963	0.591
VWC		0.014	2.090
Nontronite 1	(130,25)	0.895	0.663
Nontronite 2	(120,37)	0.943	0.802
Nontronite 3	(121,74)	0.909	0.559
VWC		0.041	0.980

Table 2. Abundance fraction of all the sample pixels by ICA-SAMSU AND ICA-AQA evaluated by variability within class (VWC).

From Table 2, the ICA-SAMSU performed significantly better than the ICA-AQA in both cases. The poor performance of the ICA-AQA was due to sensitivity to the signal pixel amplitude variance caused by the illumination variability for the same material.

## 6. Conclusion

In this paper, we presented an ICA-SAM-SU method for abundance quantification that positively contributes to hyperspectral image analysis. Linear unmixing method and spectral angle measure technique are combined by means of mathematic theories to generate abundance maps. We have demonstrated how our method based only on spectral angle measures can increase the separability among the EM spectra, making so the abundance estimation results physically meaningful. First, our method was performed using synthetic data and was compared in terms of abundance quantification rate, to one well known method (ICA-AQA). We have demonstrated that the result was approximately similar due to the purity of the data. Second, it was performed using the same data but affected with simulated multiplied errors. This experiment demonstrates the insensitivity of this approach to magnitude variation for the same materiel. Third, it was performed using real image and the results of abundance estimation for both evaluation methods are evaluated to show whether or not and to how much the ICA-SAMSU method is insensitive to the errors caused by particular illumination variability for the same material.

## REFERENCES

- [1] Sweet, J.N, "The spectral similarity scale and its application to the classification of hyperspectral remote sensing data", Advances in Techniques for Analysis of Remotely Sensed Data, IEEE Workshop, Vol. 27-28 pp. 92 – 99, Oct. 2003.
- [2] Nirmal Keshava, "A Survey of Spectral Unmixing Algorithms", Lincoln laboratory Journal, Vol. 14, NUMBER 1, 2003.
- [3] J.W. Boardman, F. A. Kruse, and R. O. Green, "Mapping target signatures via partial unmixing of AVIRIS data," in Proc. Summ. JPL Airborne Earth Sci. Workshop, Pasadena, CA, pp. 23–26, 1995.
- [4] M. E. Winter, "N-finder: An algorithm for fast autonomous spectral EM determination in hyperspectral data," in Proc. SPIE—Image Spectrometry V, vol. 3753, pp. 266–277, 1999.
- [5] R. A. Neville, K. Staenz, T. Szeregi, J. Lefebvre, and P. Hauff, "Automatic EM extraction from hyperspectral data for mineral exploration," in Proc. 4th Int.
- [6] Airborne Remote Sens. Conf. Exhib. /21st Can. Symp. Remote Sens., Ottawa, ON, Canada, pp. 21–24 Jun. 1999.
- [7] A. Plaza, P. Martinez, R. Perez, and J. Plaza, "Spatial/spectral EM extraction by multidimensional morphological operations," IEEE Trans. Geosci. Remote Sens., vol. 40, no. 9, pp. 2025–2041, Sep. 2002.
- [8] M. D. Craig, "Minimum-volume transforms for remotely sensed data," IEEE Trans. Geosci. Remote Sens., vol. 32, no. 3, pp. 542–552, May 1994.
- [9] J. W. Boardman, "Geometric mixture analysis of imaging spectrometry data," in Proc. Int. Geosci. Remote Sens. Symp., vol. 4, pp. 2369–2371, 1994.
- [10] IfarraGuerri and C.-I Chang, "Hyperspectral image segmentation with convex cones," IEEE Trans. Geosci. Remote Sens., vol. 37, no. 2, pp. 756–770, Mar. 1999.
- [11] Jing W. and Chein-I C., "Application of ICA for EM Extraction and Abundance quantification", IEEE Transactions on geosciences and remote sensing, VOL. 44, NO. 9, 2006.
- [12] D. Heinz and C.-I. Chang, "Fully constrained least squares linear mixture analysis for material quantification in hyperspectral imagery," IEEE Trans. Geosci. Remote Sensing, vol. 39, pp. 529–545, Mar. 2001.
- [13] J. D. Shepherd and J. R. Dymond, "Correcting satellite imagery for the variance of reflectance and illumination with topography ",



- International Journal of Remote Sensing, Volume 24, Issue 17 , pages 3503 - 3514, September 2003.
- [14] Jin Wang and C.-I Chang, "Independent component analysis-based dimentionality reduction with applications in hyperspectral image analysis," IEEE Trans. Geosci. Remote Sens., vol. 44, no. 6, pp. 1586–1600, Jun. 2006.
- [15] C.-I Chang and Q. Du, "Estimation of number of spectrally distinct signal sources in hyperspectral imagery," IEEE Trans. Geosci. Remote Sens., vol. 42, no. 3, pp. 608–619, March 2004.
- [16] Clark, R. N., Swayze, G. A., and Gallagher, A., "Mapping the mineralogy and lithology of Canyonlands, Utah with imaging spectrometer data and the multiple spectral feature mapping algorithm". In Summaries of the Third Annual JPL Airborne Geoscience Workshop, JPL Publication 92-14, v 1, pp. 11-13, 1992.
- [17] Hyvärinen, A., and Oja, E., "A Fast fixed-point algorithm for independent component analysis". Neural Computations 9, 7, pp. 1483-1492; 1997.
- [18] Chang, C., "Hyperspectral Imaging: techniques for spectral detection and classification". Kluwer academic/ Plenum publishers, New York 2003.
- [19] Farah I.R. and Ben Ahmed M., "Towards an intelligent multi-sensor satellite image analysis based on blind source separation using multi-source image fusion". International Journal of Remote Sensing, 31(01), pp. 13 - 38.
- [20] Cardoso, J. F., and Souloumiac, A., "Blind beamforming for non Gaussian signals. IEE Proceedings-F, 140, 6, pp. 362–370, 1993.
- [21] Leung, C. T., and Siu, W. C., "A general contrast function based blind source separation method for convolutively mixed independent sources", Signal Processing, Elsevier, 87, pp. 107–123, 2007.
- [22] Pearlman, J, Stephen Carman, Paul Lee, Lushalan Liao and Carol Segal, "Hyperion Imaging Spectrometer on the New Millennium Program Earth Orbiter-1 System" In Proceedings, International Symposium on Spectral Sensing Research (ISSR), Systems and Sensors for the New Millennium, 1999.



**Zouhaier B. Rabah** received the M.E. degree in engineering from the High School of Telecommunication (SupCom), Tunisia, in 2004. Since 2007, he has been a Permanent Researcher with the Laboratory RIADI, National School of Computer Sciences Engineering. His research interest includes images processing, image fusion, artificial intelligence, data mining, pattern recognition, and their application to remote sensing.



**Basel Solaiman** received the M.E. degree in telecommunication engineering from the Ecole Nationale Supérieure des Télécommunications de Bretagne (TELECOM-Bretagne), Brest, France, in 1983 and the Ph.D. degree from the University de Rennes I, Brest, in 1989. From 1984 to 1985, he was a Research Assistant with the, Communication Group, Centre d'Etudes et de Recherche Scientifique, Damascus, Syria. In 1992, he joined the Laboratoire ITI, TELECOM Bretagne Technopôle Brest Iroise, Brest. His current research interests include the fields of remote sensing, medical image processing, pattern recognition, neural network, and artificial intelligence.



**Imed Riadh Farah** received the M.D. degree from ISG Institute of Computer Sciences, Tunis, Tunisia, in 1995 and the Dr. Eng. degree from ENSI, Manouba, Tunisia, in 2003. He was with the Laboratory RIADI, National School of Computer Sciences Engineering, Manouba, Tunisia, where he became a Permanent Researcher in 1995 and a Research assistant in 1996. Since 2004, he has been an Assistant Professor with the University of Jendouba, Jendouba, Tunisia. His research interest includes image processing, pattern recognition, artificial intelligence, data mining, and their application to remote sensing. Prof. Farah is a member of Arts-Pi Tunisia



**Henda Ben Ghezala** is currently Professor of Computer Science in the department of Informatics at the National School of Computer Sciences of Tunis. She leads a Master degree in 'ICIS'. She is the president of University of Manouba. Her research interests lie in the areas of information modeling, databases, temporal data modeling, object-oriented analysis and design, requirements engineering and specially change engineering, method engineering. She is Director of the RIADI labs.

